Simulation of Li Dendrite Inhibition in Lithium Battery by Phase-Field Method

By

Yao Ren

DISSERTATION

Submitted in partial fulfillment of the requirements
for the Degree of Doctor of Philosophy
in Materials Science and Engineering at
The University of Texas at Arlington
May 2022

Arlington, Texas

Supervising Committee:

Dr. Efstathios "Stathis" I. Meletis, Committee Chair
Dr. Ye Cao, Supervising Professor
Dr. Yaowu Hao
Dr. Erika La Plante
Dr. Qiming Zhang

ACKNOWLEDGEMENT

First, I would like to express my sincere thanks to my advisor Dr. Ye Cao who gives me meticulous guidance to my research and at the same time gives me the freedom to involve my own ideas into the research. Second, I would also like to thank my parents. Their love and support are the cornerstone of my success. Furthermore, I would also like to thank Dr.Efstathios "Stathis" I. Meletis, Dr. Qiming Zhang, Dr.Yaowu Hao and Dr. La Plante for being my committee members and the suggestions on my research which improves my work. Next, I want to thank my current and former group members, Kena Zhang, Ryan Hart and Bharat Pant. It feels so happy to work with you and learn from each other. I would also like to thank Dr. Yue Zhou from South Dakota State University for his experimental support. Finally, I appreciate the support from my wife. Her love and companionship are the encouragement when I want to give up.

Table of Contents

List of Figures

List of Tables

Abstract

Lithium (Li) dendrite growth poses serious challenges for the development of Li metal batteries which also stops the footsteps of human utilizing the environment-friendly new power source. Replacing liquid electrolyte with solid electrolyte can not only inhibit the dendrite growth by mechanical suppression, but also introduce more possibilities to the electrochemistry of battery. However, the underlying mechanism is still not fully understood, and most theoretical works focus on pure liquid electrolyte, ignoring the mechanical strain effects. Here we developed a phase-field model which simulates the Li dendrite growth to study the competition between diffusion and deposition rates, the pure elastic and Elasto-plastic effects, and the inhibition from nanofillers embedded in the solid electrolytes. It is revealed that high diffusion rate can transport more Li ions to the electrode surface, which create a low concentration gradient at the interface, leading to a smooth electrode surface.

Li dendrite can also be effectively inhibited by the electrolytes of high elastic modulus and initial yield strength, which induce and withstand the large mechanical suppression, respectively. High-throughput phase-field simulations are performed to establish a database of relationships between the aforementioned mechanical properties and the Li dendrite morphology, based on which a compressed-sensing machine learning model is trained to derive interpretable analytical correlations between the key material parameters and the dendrite morphology, as described by the dendrite length and area ratio. It is revealed that the Li dendrite can be effectively inhibited by the electrolytes of high elastic

modulus and initial yield strength. Meanwhile, the role of the yield strength of Li metal is also critical when the yield strength of the electrolyte becomes low.

We also discovered that the introduction of the 1D nanofiber arrays could confine the Li ion transport along horizontal direction, reduce the concentration gradient across the electrode/electrolyte interface, and inhibit the Li dendrite growth. Our work provides deep understanding of the dendrite growth mechanism, the mechanical suppression and the inhibition by the 1D nanofiber array, as well as the designing strategy for the solid composite electrolyte for improved Li anode stability and Li ion conductivity.

Furthermore, we also explored the formation process of dead Li and study the formation mechanism. It is found that the initial Li amount affects the dead Li most while the high discharge voltage will also lead to the formation of dead Li.

Keywords: Lithium dendrite; Polymer composite electrolyte; Mechanical suppression; Elasto-plastic effects; Machine learning; Dead lithium; Phase-field simulation

Chapter 1. Introduction

1.1 Research motivation and objectives

The ever-growing demand of wearable and mobile electronic devices, electric vehicles, grid-scale electrical storage, and other energy storage systems requires the advancement of lithium-ion (Li-ion) batteries of high energy density and improved safety and stability[1,2]. One of the most promising approaches is to replace the existing graphite anodes with the lithium (Li) metal anodes, which has the highest theoretical capacity (3860 mAh/g), low density (0.53g/cm^3), and lowest negative electrochemical potential (-3.04V vs. standard hydrogen electrode) [3–5]. However, a critical issue that impedes the wide application of Li metal battery is the uncontrollable Li electrodeposition in the form of dendrites or filaments. These needle- or branch-like dendrites can eventually penetrate the separator of the cell, which creates serious problems such as lowered Coulombic efficiency, large mechanical deformation of the electrodes, reduced battery cycle life, and catastrophic internal short circuit[6–8].

The Li dendrite growth can be considered as the results of the competition between the Li ion transport and the electrodeposition. High electrodeposition rate together with a low Li ion transport rate leads to insufficient Li ions at the anode surface, which finally induces the uneven deposition of Li ions, which is also called dendrite. A fundamental understanding of this competition should be built, in which the Li ion transport rate is decided by the electrolyte materials, and the electrodeposition rate is related to the exchange current.

In addition, the mechanical suppression on dendrites using solid electrolyte of high mechanical strength and good ionic conductivity is one of the most promising methods. However, few phase-field models take the mechanical interaction between solid electrolyte and Li dendrite into consideration, which may be reasonable for liquid electrolyte, but should not be ignored in the solid electrolytes. Moreover, recent findings show that the Monroe-Newman theory, that electrolyte with two-times shear modulus of the electrode will stabilize the lithium surface, cannot explain all the phenomena in Li dendrite growth. For example, inorganic electrolytes such as $Li_7La_3Zr_2O_{12}$ (LLZO)[9,10], β-Li_3PS_4[11], and $Li_2(OH)_{0.9}F_{0.1}Cl$[12], which showed extremely high elastic (and shear) modulus (~10^2 GPa), still suffered from Li dendrite growth. On the other hand, recent studies also revealed that soft solid electrolytes (SE) with very low elastic modulus (such as rubber, E= 0.4 MPa) can still suppress Li dendrite growth over long cycling time[13,14]. One possible reason for these discrepancies between Monroe-Newman's theory and recent findings is the dynamic mechanical properties of Li metal anode during the electrodeposition as their theory is based on the linear elasticity, ignoring the plastic effect. It is reported that the yield strength of Li metal could increase from ~10^{-1}MPa to 10^2MPa as it is strongly dependent on the Li grain size[9,15], temperature[16], strain rate[17,18] and applied current density[18]. Therefore, the mechanical interaction including the elastic and plastic effects should be studied comprehensively for better understanding of inhibition of Li dendrite growth.

Finally, composite polymer electrolytes are commonly used in the battery to compensate the mechanical, electric or compatibility properties of pure polymers. The amount and size of the nanofillers in the composite are critical to control these properties and finally affect the inhibitory effects of dendrites. Therefore, it is imperative to develop

a new phase-field model to capture the Li dendrite dynamics in a composite polymer electrolyte system.

In this work, we aim at solving the three problems by developing a new phase-field model that couples the energy barrier effect (control the transport and deposition rates), mechanical effect and nanofiller effect together. An overall understanding of these effects will be studied by:

1) Varying the energy barriers of diffusion and reaction to control the rates and study the competition between the transport and electrodeposition.
2) Controlling the mechanical properties of the Li metal and electrolyte to study their effects on the dendrite growth.
3) Trying different amounts and sizes of nanofibers in the polymer to help understanding the inhibition by the nanofibers.

1.2 Development of lithium battery

With the growing crisis of non-renewable energy resources tensions, the rechargeable chemical power supply which is an energy storage device has been created and plays an important role in storing energy and providing power[19]. The chemical power supply is also named as electrochemical battery which converts the chemical energy to the electrical energy when in use. The representative batteries can be divided into the following categories, such as the lead-acid battery, nickel–cadmium (Ni-Cd) battery, nickel metal hydride (NiMH) battery, sodium-sulfur battery and lithium-ion (Li-ion) battery[20]. In terms of energy density[20], as shown in Figure 1-1, the gravimetric and volumetric energy density

of the lead-acid battery is about 30 $Wh \cdot Kg^{-1}$ and $100Wh \cdot L^{-1}$,respectively, while that of lithium-ion or lithium metal battery is about 3 to 5 times more than the lead-acid battery, together with 3 times battery life. Comparing with Ni-Cd or NiMH battery, Li-ion battery still have a double battery life with half volume and weight. Moreover, the Li-ion battery has the features like low density, no memory effect, environmentally friendly, safety and stability *etc.* which make it considered as the most potential candidates of rechargeable battery and raises the research passionate in industry and academia.

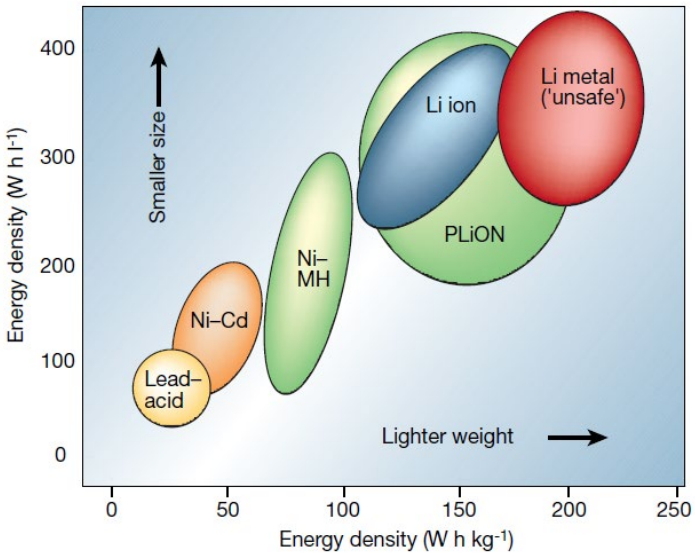

Figure 1-1 Comparison of the different battery technologies in terms of volumetric and gravimetric energy density[20].

The development of lithium batteries can be traced back to 1910s. G.N. Lewis began the experimentation with lithium battery in 1912, however, it was not commercialized until the 1970s[19,21]. The first-generation commercial rechargeable lithium battery came to the market, manufactured by Exxon Company with a TiS_2 cathode and by Moli Energy with a MoS_2 cathode, together with a Li-metal anode. However, during the

charging process, the Li ion tends to locally deposit at the Li metal anode and form the dendritic deposited lithium which will lead to the explosion of battery in extreme cases. For safety concerns, the development of lithium batteries was even stagnant for a while. Until 1991, Sony introduced the first commercial Li-ion battery[22] with the graphite as the "lithium sink" anode and the lithium cobalt oxide as the "lithium source" cathode, based on the concept of the rocking chair battery[23,24]. During the charging process, the reaction at the cathode is $LiCoO_2 \rightarrow Li_{1-x}CoO_2 + xLi^+$, at the anode is $xLi^+ + C \rightarrow Li_xC$, while reactions in the discharging process are the opposite, as shown in Figure 1-2(a). Since then, Li-ion batteries were widely used in all aspects of daily life[25,26].

In recent years, due to the emergence of new industries such as high-end communication terminals, electric vehicles, aerospace, and grid-scale energy storage stations, the demand for energy storage systems with high energy density has increased. Extensive efforts have been made to improve the energy density, safety and stability of lithium-ion batteries[1,2]. One promising approach is to replace the current graphite anodes with the lithium (Li) metal anodes, for the highest theoretical capacity (3860 mAh/g), low density (0.53 g/cm^3), and the lowest redox electrochemical potential (-3.04V vs. standard hydrogen electrode)[3–5]. In addition, the use of lithium metal anode can eliminate the need for current collectors in conventional graphite cathodes which makes the weight of the total cell dramatically reduced[27]. As the source of lithium ion in the battery, the lithium metal anode also enables the application of unembedded-lithium cathode materials that allows higher capacity than conventional cathode material in the cell such as sulfur[28,29] and air[29], as shown in Figure 1-2(b).

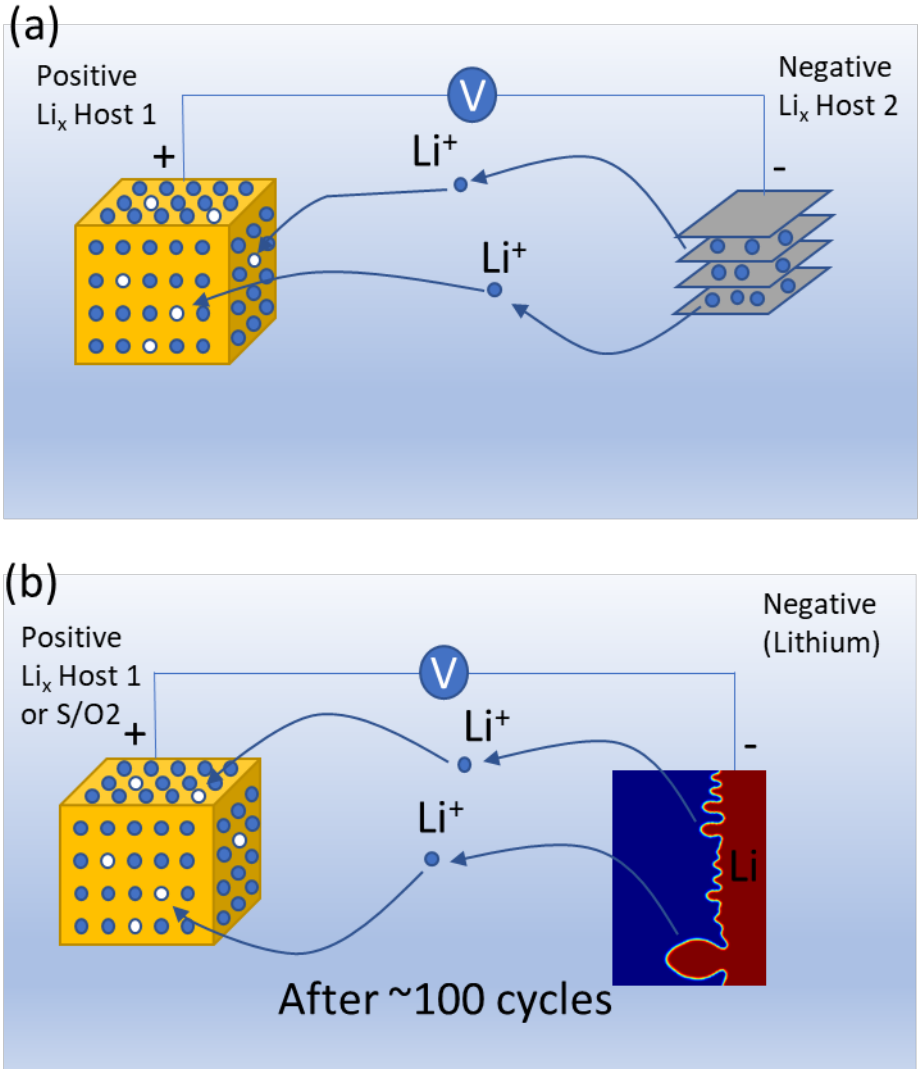

Figure 1-2 Schematic representative diagram and operating principles of (a) rechargeable lithium-ion battery and (b) rechargeable lithium metal battery (the schematic picture of dendrites at the Li surface was from the simulation results).

1.3 Existing problems in lithium metal battery

The lithium is considered as the ideal material for the battery due to its outstanding theoretical capacity and energy density. However, the lifetime and safety issues induced by using the lithium metal as anode during repeated charge and discharge cycles are common problems for lithium batteries which impedes the wide applications of lithium

metal battery. The dendrite growth brings many problems as shown in Figure 1-3 to the battery such as[30–35] (1) internal short circuit induced by lithium dendrite penetration into separator. During the charging and discharging process of lithium batteries with lithium metal as the negative electrode, the electrode surface will form SEI (solid electrolyte interface) layer. The lithium dendrites grow on the negative electrode, then extend through the separator to the positive electrode which leads to short circuit inside the battery and cause a fire or explosion. This is a major safety hazard. (2) formation of "dead lithium" which leads to low capacity and life. During the discharge process, if the point contact between lithium dendrites and electrode surface is broken, 'dead lithium' forms and falls into the electrolyte, which cannot participate in the subsequent electrochemical reactions, resulting in a significant reduction in the capacity of the lithium battery. (3) aggravated adverse reactions which reduces battery capacity. The formation of lithium dendrites can lead to the breakdown of the SEI layer and cause continuous reactions between the metallic lithium and electrolytes which consumes active lithium and finally reduces the capacity irreversibly as well. (4) increased polarization. The electrode with lithium dendrites always has a porous structure, together with the 'dead lithium' around the electrode, leading to an increased diffusion pathway and large resistance for the transport of Li ions and electrons. In this way, it renders an increased polarization and reduce the energy efficiency. (5) large volume change. Metallic lithium anodes have a higher volume change, which is far above these intercalated anodes, such as graphite (10%) and silicon (400%)[36]. The presence of lithium dendrites makes the embedded lithium metal porous, leading to harsher volume change issues. These porous lithium deposits prompt significant volume increase/decrease during the lithium plating/stripping, resulting in the lithium powderation at the electrode

surface and decreasing of the battery life and performance[5]. Therefore, the depression of dendrite growth is the most impending mission on the way to achieving the goal of battery safety and long life.

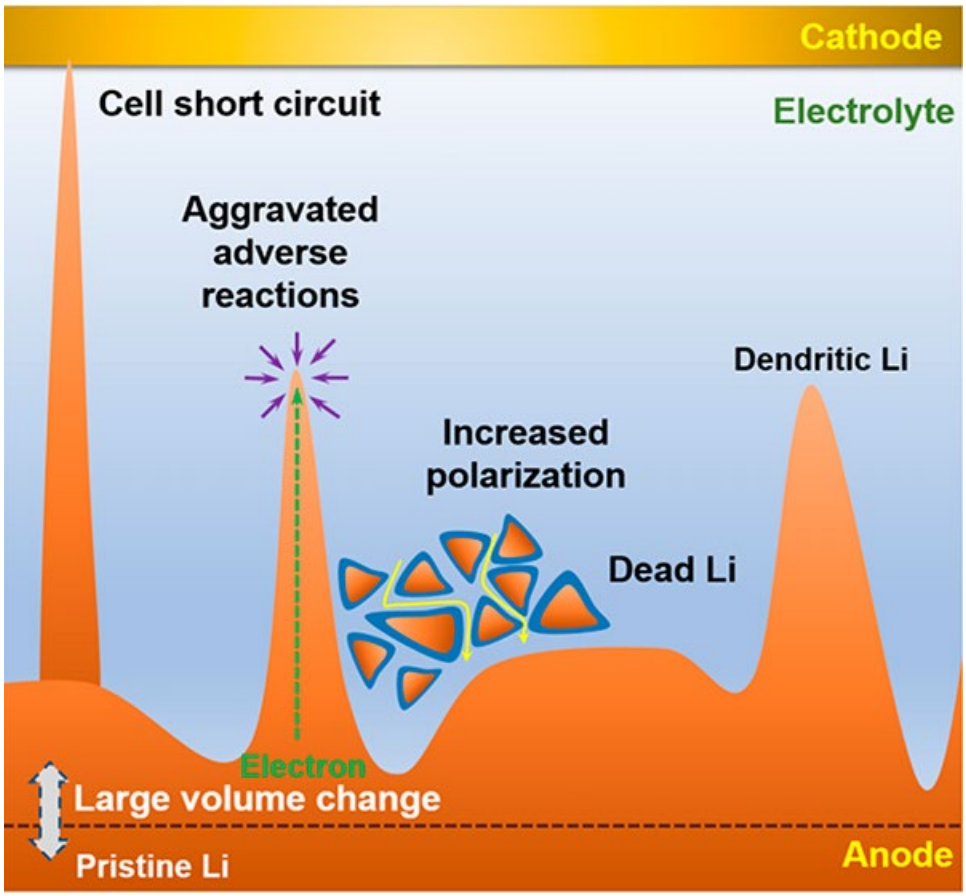

Figure 1-3 Existing problems caused by lithium dendrites[36]

In industry, when plating metals such as Cu, Ni and Zn at high current densities, the cathode is tilted toward plated metals with dendritic morphology[5]. During the electroplating process, the metal cations will diffuse from the anode to the cathode. At high current density, a gradient of cation concentration gradually appears between the two electrodes with the progress of plating. When the current density reaches to a critical value

J^*[37,38] (see Eq.(1)), the cations are depleted at the surface of cathode (Figure 1-4 (a)&(b)) after some time named as Sand's time[39], thus breaking the electrical neutrality of the electrode surface, forming a local space charge(Figure 1-4 (c)), inducing the generation of stable concentration gradients, and eventually leading to the formation of dendritic metallic precipitates(Figure 1-4 (d)).

$$J^* = \frac{2eDC_0(\mu_a + \mu_c)}{\mu_a L} \tag{1}$$

where D is the bipolar diffusivity ($D = (\mu_a D_a + \mu_c D_c)/(\mu_a + \mu_c)$, C_0 is the standard ion concentration, z is the charge number, L is the distance between two electrodes, e is the unit charge. The subscripts a and c mean anion and cation.

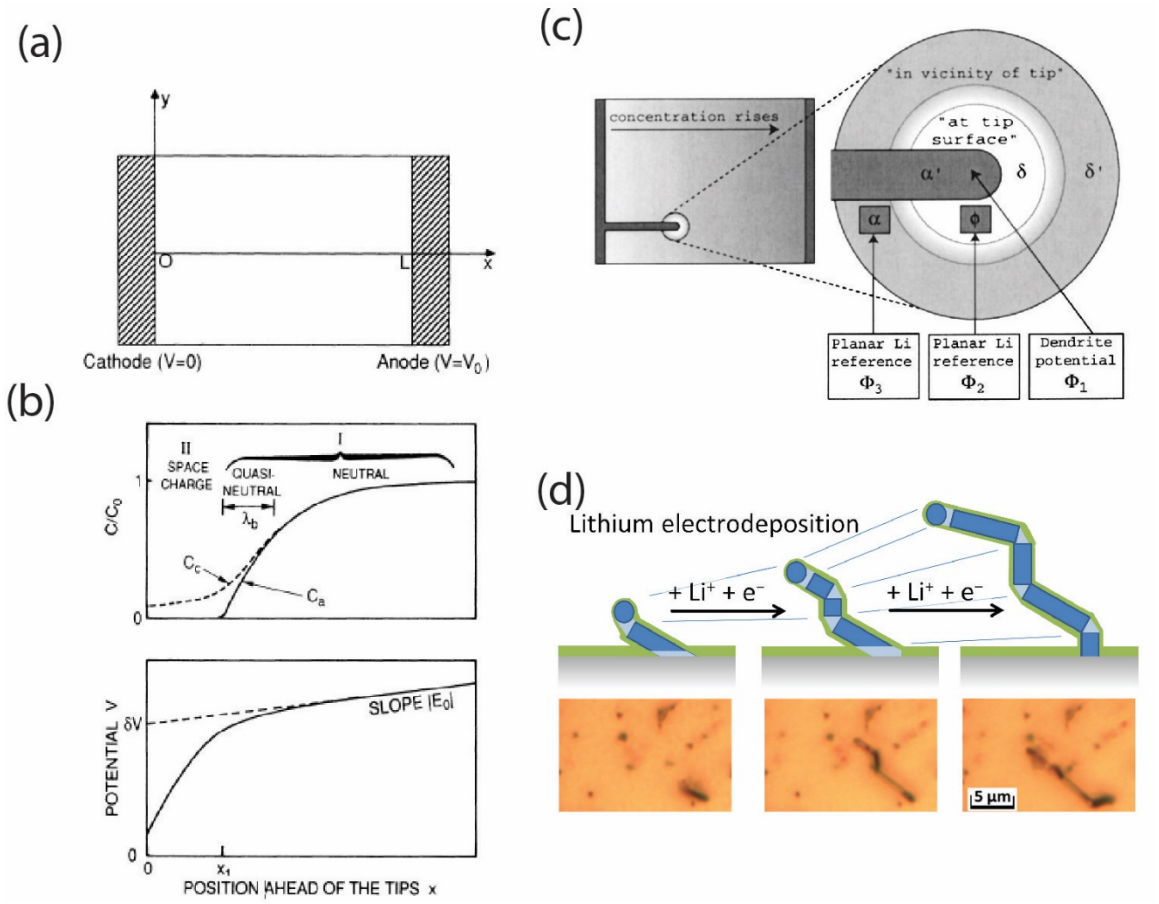

Figure 1-4 The factors of inducing dendrites (a) Scheme of a symmetrical cell. (b) Profile of the ion concentration and electrostatic potential obtained from the numerical calculation in the case of filamentary growth. (c) Diagram of a region near the tip of lithium dendrites. (d) Schematic and optical images describing the growth of lithium needle-like dendrite as observed in *in-situ* videos recorded under optical microscopy.

According to the numerical calculation of critical current density J^*, in the charge process, if current density $J > J^*$, it is obvious that dendrites form on the anode surface. However, as J^* is relatively large in common lithium metal batteries, the batteries are mostly operated at a current density far below J^*. However, the dendrites formation can still be observed[40], indicating that a different mechanism is dominating. Besides considering the transport of lithium ion, the impact of interfacial chemistry at the electrode surface should also be included. Usually, the uneven composition of the solid electrolyte

layer on the surface of the negative electrode leads to the uneven conductivity of lithium ions, which eventually leads to the uneven nucleation of lithium ions on the surface of anode. Afterwards, the uneven nucleation of lithium ions and the volume expansion due to the plating of lithium tend to promote the formation of cracks in the solid electrolyte layer, and the lithium-ion deposition rate at the cracks is higher than that at the other parts of the electrode surface, which aggravates the reactive dispersion of lithium dendrites[41].

1.4 Experimental efforts to inhibit lithium dendrite

Multiple experimental approaches have been proposed to inhibit the dendrite growth such as electrolyte modification[42–47], SEI protection layer[48–53], concentrated electrolyte[54–60], solid electrolyte[61], separators[62–67] *etc.* By using one or a combination of the above methods, the lithium dendrite gets effectively inhibited so that the battery capacity, energy density, cycle stability and safety are improved, which is meaningful to the lithium battery development. The following will explain the details.

1.4.1 Electrolyte modification & SEI protection layer

The electrolyte additives have been used to improve the performance of lithium anode. These additives will decompose, accumulate or adsorb on to the anode surface to enhance the properties of SEI layer to reach the goal of adjusting Li-ion distribution during plating. The traditional additives can be (1) fluorinated compounds. The addition of a small amount of HF and H_2O to the carbonate electrolyte can form a flexible and homogeneous LiF/Li_2O bilayer on the anode surface, resulting in smooth deposition of lithium. Lu *et al.*[68] introduced LiF and formed dense SEI layer which protects the anodes, inhibits the dendrite and extends the life of battery. (2) metal ions. When metal ion (M^+) is introduced to the electrolyte, it shows the same tendency to plate as Li ion. If M^+ has a lower reduction

potential than Li^+, it will adsorb to the lithium surface instead of being reduced. When uneven lithium deposition occurs, the charge accumulation at the protrude will attract more M^+ to form an electrostatic field which repels Li+ and stops the further growth of protrude[69,70]. (3) synergistic effects. For instance, Li *et al.*[50] found when the two additives Li_2S_8 and $LiNO_3$ are introduced to the electrolyte, $LiNO_3$ will first react with lithium to passivate the lithium surface, then Li reacts with Li_2S_8 at the upper SEI layer, forming Li_2S/Li_2S_2 to stop the decomposition of the electrolyte which stabilize the battery cycle at large charge/discharge rate.

1.4.2 Concentrated electrolyte

With the lithium metal battery is intensively studied, concentrated electrolyte shows good performance in lithium metal anode which overturns the conclusion that electrolyte of 1.0mol/L concentration has the best ionic conductivity and viscosity based on the research of Li-ion battery[71]. Concentrated lithium salt can increase the critical value of current density (J^*) (see Eq.(1)) so that the dendrites get inhibited. Suo *et al.*[58] use 7mol/L LiTFSI as the electrolyte of Li-S battery which inhibits the lithium dendrite, decreases the dissolution of Li_2S_x as well as increases the ionic conductivity.

1.4.3 Solid electrolyte

Despite the advantages of liquid electrolytes such as high conductivity and good wettability to electrode surfaces, they often suffer from insufficient electrochemical and thermal stabilities, low ion selectivity and safety issue[72]. Replacing liquid electrolytes with solid electrolyte separators not only overcomes the persistent problems of liquid electrolytes, but also offers the possibility of developing new battery chemistries. By using the solid electrolytes with excellent mechanical properties, the mechanical suppression is

applied onto the dendrites which is a direct physical way to stop the dendrite growth. Besides mechanical properties, the other main properties required for solid electrolytes can be summarized as: high ionic conductivity, low ionic area-specific resistance, high electronic area-specific resistance, high ionic selectivity, wide electrochemical stability, good chemical compatibility, easy manufacturing process and environmental friendliness[72–76]. Both inorganic and organic (polymeric) solid electrolyte materials have been made with a great progress in improving the above properties. Table 1 gives a summary of the common solid electrolytes with their properties are visualized in the radar plots in Figure 1-5[77].

Table 1 Summary of lithium-ion solid electrolyte materials[77]

Type	Materials	Conductivity (S cm^{-1})	Advantages	Disadvantages
Oxide	Perovskite, $Li_{3.3}La_{0.56}TiO_3$, NASICON $LiTi_2(PO_4)_3$, LISICON $Li_{14}Zn(GeO_4)_4$ and garnet $Li_7La_3Zr_2O_{12}$	10^{-5} – 10^{-3}	•High chemical and electrochemical stability •High mechanical strength •High electrochemical oxidation voltage	•Non-flexible •Expensive large-scale production
Sulfide	Li_2S-P_2S_5, Li_2S-P_2S_5-MS_x	10^{-7} – 10^{-3}	•High conductivity •Good mechanical strength and mechanical flexibility •Low grain-boundary resistance	•Low oxidation stability •Sensitive to moisture •Poor compatibility with cathode materials
Hydride	$LiBH_4$, $LiBH_4$-LiX (X=Cl,Br or I), $LiBH_4$-	10^{-7} – 10^{-4}	•Low grain-boundary resistance •Stable with lithium metal •Good mechanical strength and mechanical flexibility	•Sensitive to moisture •Poor compatibility with cathode materials

	$LiNH_2$,$LiNH_2$,$LiAlH_6$ and Li_2NH			
Halide	LiI, spinel Li_2ZnI_4 and anti-perovskite Li_3OCl	10^{-8} – 10^{-5}	•Stable with lithium metal •Good mechanical strength and mechanical flexibility	•Sensitive to moisture •Low oxidation voltage •Low conductivity
Borate or Phosphate	$Li_2B_4O_7$, Li_3PO_4 and Li_2O-B_2O_3-P_2O_5	10^{-7} – 10^{-6}	•Facile manufacturing process •Good manufacturing reproducibility •Good durability	•Relatively low conductivity
Thin film	LiPON	10^{-6}	•Stable with lithium metal •Stable with cathode materials	•Expensive large-scale production
Polymer	PEO	10^{-4} (65-78°C)	•Stable with lithium metal •Flexible •Easy to produce a large-area membrane •Low shear modulus	•Limited thermal stability •Low oxidation voltage (<4 V)

LiPON, lithium phosphorus oxynitride; LISICON, lithium superionic conductor; NASICON, sodium superionic conductor; PEO, poly(ethylene oxide).

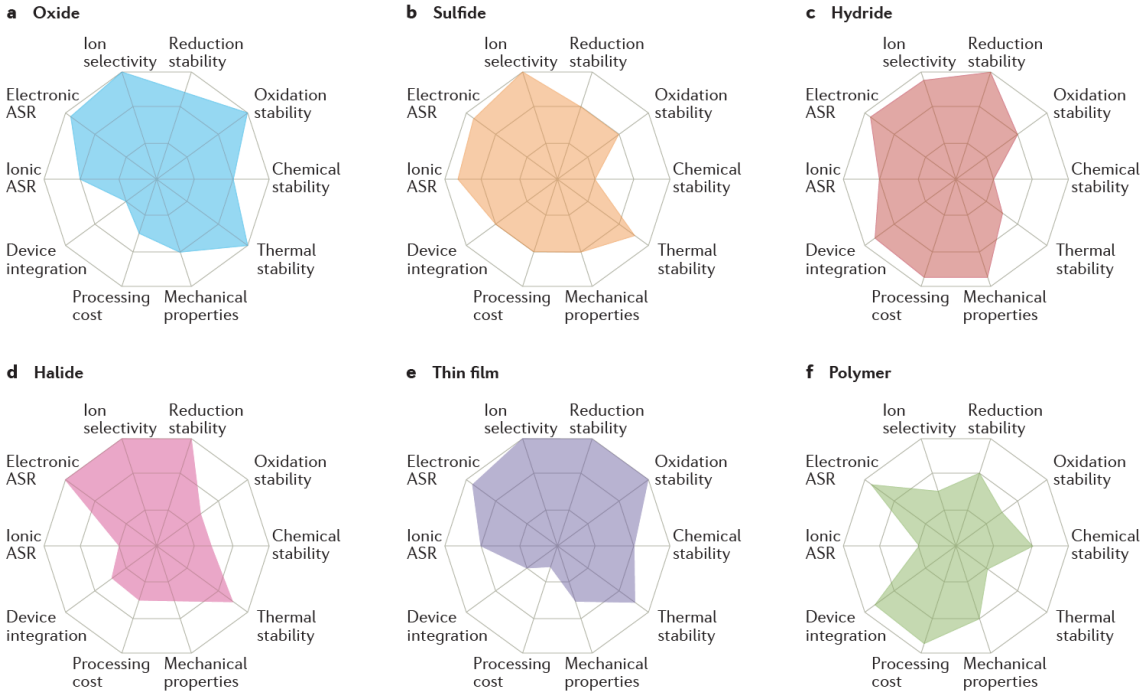

Figure 1-5 Performance of different solid electrolyte materials. Radar plots of the properties of a) oxide b) sulfide c) hydride d) halide e) thin film f) polymer.[77]

1.4.3.1 Inorganic solid electrolytes

The inorganic solid electrolytes can be mainly categorized into four types: perovskite type, NASICON type, garnet type and sulfide type. The representative perovskite-type electrolyte, $Li_{3x}La_{2/3-x}TiO_3$, exhibits a Li-ion conductivity over 10^{-3} S cm^{-1} at room temperature[78], but suffers from the reduction of Ti^{4+} contacting with Li metal.

NASICON-type compounds were named in 1976 due to the development of $Na_{1+x}Zr_2Si_xP_{3-x}O_{12}$[79], and generally have the general formula of $AM_2(PO_4)_3$, where A and M are usually occupied by Li, Na or K and Ge, Zr or Ti, respectively[80]. The properties like ionic conductivity and electrochemical can be enhanced with substitution to form $Li_{1+x}M_x(Ti/Ge)_{2-x}(PO_4)_3$ which M can be Al, Cr, Ga *etc.* The Al substitution is mostly used for its efficiency in improving ionic conductivity for $LiTi_2(PO_4)_3$ system[81–84] and electrochemical stability for $LiGe_2(PO_4)_3$ system[85–87]. NASICON-type electrolytes are suitable for high-voltage solid electrolyte batteries.

Garnet-type materials have been widely investigated since the first discovery in 1969[88]. The representative systems are $Li_5La_3M_2O_{12}$ (M=Nb or Ta), $Li_6ALa_2M_2O_{12}$ (A=Ca, Sr or Ba; M=Nb or Ta), $Li_{5.5}La_3M_{1.75}B_{0.25}O_{12}$ (M=Nb or Ta; B=In or Zr), $Li_7La_3Zr_2O_{12}$ and $Li_{7.06}M_3Y_{0.06}Zr_{1.94}O_{12}$ (M= La, Nb or Ta)[89–93]. The ionic conductivity of garnet-type materials at room temperature can reach to as high as 1.02×10^{-3} with $Li_{6.5}La_3Zr_{1.75}Te_{0.25}O_{12}$[94].

The investigation of sulfide-type electrolytes dates back to 1986 with the Li_2S-SiS_2 system[95]. With the system being studied, in 2001, LISICON (lithium superionic conductor) crystalline material was found in the Li_2S-SiS_2 system[96]. Since then, it has been widely reported to show a high Li-ion conductivity[96–100]. The disadvantage of sulfide-type

electrolytes is poor chemical stability and sensitivity to moisture. The stability can get improved by adding the metal oxides to the system[101–103].

1.4.3.2 Organic solid electrolytes

Organic solid electrolytes are mostly polymer or polymer composites. The polymer acts as the host of lithium salt to form a solid solvent[104–107]. The polymer hosts are commonly PEO (polyethylene oxides), PAN (polyacrylonitrile), PMMA (poly(methyl methacrylate)), PVC (poly(vinyl chloride)) or PVDF (polyvinylidene fluoride)[108–112], among which PEO is the most widely used. As the bare polymer host is poor at ionic conductivity at ambient temperatures, ceramic nanofillers are integrated into the host, help improving the conductivity[113–115]. The ceramic fillers can be divided into two types: active type (e.g. Li_2N and $LiAlO_2$[116–118]) and passive type (e.g. Al_2O_3 SiO_2 and MgO[119–121]) based on whether they involve in ion transport or not.

1.4.3.3 Thin-film solid electrolytes

Thin-film solid electrolytes are solid electrolytes that can be fabricated as ultrathin films via specific vapour deposition techniques like pulsed laser deposition, chemical vapour deposition *etc.* The standard thin-film solid electrolyte was reported by Oak Ridge National Laboratory based on LiPON (lithium phosphorus oxynitride)[122–124]. Another series of thin-film solid electrolytes based on lithium borate, lithium phosphate and lithium borophosphate, which have advantages at industry-level manufacture, have been reported as the candidate of LiPON[125–128]. Also, with the development of deposition techniques, newly emerged atomic layer deposition is being applied to other series of solid electrolytes like Li_3PO_4, $Li_xAl_2O_3$ and $Li_xSi_yAl_2O_3$[129–131].

1.4.4 Separators

Separators are the important component of lithium battery although they do not involve in electrochemical reactions. On the one hand, it provides a path for Li ion transport, on the other hand, it physically separates the anode from the cathode. Its mechanical property, thermal stability and ion transmission performance play a critical role in the performance and safety of battery. The modification of separators mainly focuses on enhancing these properties. Wu *et al.*[132] modified the commercial polypropylene separator through layer-by-layer self-assembly method, adsorbed with MoS_2 and polyacrylic acid on both sides in a uniform and orderly manner, in which polyacrylic acid layer prevents the transmission of polysulfides while the MoS_2 layer enhances the mechanical properties that physically suppress the dendrite growth.

1.5 Thermodynamics and previous theoretical models

Theoretical efforts have also been made to understand the growing mechanism of lithium dendrites. The dendrite growth process is an electrodeposition that happens at the electrode/electrolyte interface with the interface morphology changing under chemical, electrical and mechanical driving forces. To model this electrodeposition process, its thermodynamics should be first understood.

1.5.1 Thermodynamics

The Gibbs free energy of the electrodeposition system can be expressed by

$$G = \int_V f(\vec{c}, \varphi) dV \tag{2}$$

Here the $f(\vec{c},\varphi)$ is the Gibbs free energy density, V is the volume of the entire system, φ is the electrical potential. $\vec{c}$ indicates the concentrations of species in the system, consisting of c for M atom, c_+ for cation M^{z+} and c_- for the anion A^-. After normalizing the concentrations as $c^* = c / c_s; c^*_{+/-} = c_{+/-} / c_0$, where c_s is the site density of metal M and c_0 is the bulk concentration of electrolyte solution, the classic electrochemical potential can be identified as

$$\overline{\mu}_i = RT \ln a_i + \mu_{i0} + z_i F\varphi = RT \ln c_i^* + \overline{\mu}_i^{ex} \tag{3}$$

where R is the molar gas constant, T is the temperature, F is the Faraday's constant, a_i, μ_{i0} and z_i denote the activity, reference chemical potential and charge number of species i, respectively. $\overline{\mu}_i^{ex}$ is the excess electrochemical potential. If we assume the M metal and the electrolyte have no interaction when added into the system, the total electrochemical free energy can be introduced like

$$f_{el+ch} = \sum_i c_i \overline{\mu}_i = \sum_i c_i (RT \ln a_i + \mu_{i0} + z_i F\varphi) \tag{4}$$

As the electrolyte is commonly a dilute solution which means $a_i = c_i^*$, Eq.(4) can be written as

$$\begin{aligned} f_{el+ch} &= RT \sum_i c_i \ln c_i^* + \sum_i c_i \mu_{i0} + \sum_i F z_i c_i \varphi \\ &= c_s RT c^* \ln c^* + c_0 RT (c_+^* \ln c_+^* + c_-^* \ln c_-^*) + \sum_i c_i \mu_{i0} + \rho_e \varphi \end{aligned} \tag{5}$$

The term $c_s RT c^* \ln c^*$ in Eq.(5) indicates the contribution from M atom. For metal phase, the dimensionless concentration c^* equals 1 while for electrolyte phase, it equals 0. Based

on that, we have $c_s RTc^* \ln c^* = 0$ when assuming that there is sharp gradient at the metal-electrolyte interface.

To describe the diffusion interface in the model, a continuous phase-field variable ξ is introduced to the system whose physical meaning is the dimensionless concentration of M atom ($\xi = c^*$). A simple double-well function ($W\xi^2(1-\xi)^2$) is used to represent two equilibrium states for the metal electrode ($\xi = 1$) and the electrolyte ($\xi = 0$), where $W/16$ is the energy barrier height at $\xi = 0.5$. Thus, the total electrochemical free energy reads

$$f_{el+ch} = W\xi^2(1-\xi)^2 + c_0 RT(c_+^* \ln c_+^* + c_-^* \ln c_-^*) + \sum_i c_i \mu_{i0} + \rho_e \varphi \tag{6}$$

The free energy density related to the gradient is given by

$$f_{grad} = \frac{1}{2} \nabla \vec{c}^* \cdot \kappa \vec{c}^* \tag{7}$$

Combining Eqs.(6)(7) gives the Gibbs free energy

$$\begin{aligned} f(\vec{c}, \varphi) &= f_{el+ch} + f_{grad} \\ &= W\xi^2(1-\xi)^2 + c_0 RT(c_+^* \ln c_+^* + c_-^* \ln c_-^*) + \sum_i c_i \mu_{i0} + \rho_e \varphi \\ &\quad + \frac{1}{2} \nabla \vec{c}^* \cdot \kappa \vec{c}^* \end{aligned} \tag{8}$$

The energy term details in Eq.(8) are given as

$$\begin{aligned} f_{ch}(\vec{c}) &= W\xi^2(1-\xi)^2 + c_0 RT(c_+^* \ln c_+^* + c_-^* \ln c_-^*) + \sum_i c_i \mu_{i0} \\ f_{elec}(\vec{c}, \varphi) &= \rho_e \varphi = F \sum_i z_i c_i \varphi \\ f_{grad}(\vec{c}) &= \frac{1}{2} \nabla \vec{c}^* \cdot \kappa \vec{c}^* \end{aligned} \tag{9}$$

The reaction of an electrodeposition process is $M^{z+} + ze^- \rightarrow M$, indicating the metal ion M^{z+} combines with electron e^- and produces the metal atom M. According to the consistent formulation of electrochemical reaction kinetics[133,134], the reaction rate, R_e, is related to the excess electrochemical potential of all species, as

$$R_e = -k_0 c_1^* \exp[\frac{-(\overline{\mu}_t^{ex} - \overline{\mu}_1^{ex})}{RT}] + k_0 c_2^* \exp[\frac{-(\overline{\mu}_t^{ex} - \overline{\mu}_2^{ex})}{RT}] \tag{10}$$

where k_0 is the reaction constant, $\overline{\mu}_t^{ex}$, $\overline{\mu}_1^{ex}$ and $\overline{\mu}_2^{ex}$ are the activation barrier and local minimum excess electrochemical potentials for two states, respectively, as shown in Figure 1-6. By substituting $c_i^* = \exp(\frac{RT \ln c_i^*}{RT})$ and Eq.(3) into Eq.(10), the reaction rate can also be expressed as

$$R_e = -k_0 \{\exp[\frac{-(\overline{\mu}_t^{ex} - \overline{\mu}_1)}{RT}] - \exp[\frac{-(\overline{\mu}_t^{ex} - \overline{\mu}_2)}{RT}]\} \tag{11}$$

where $\overline{\mu}_1$ and $\overline{\mu}_2$. are the electrochemical potentials of two states. At equilibrium ($R_e = 0$), the two electrochemical potentials should equal, $\overline{\mu}_1 = \overline{\mu}_2$. From the definition of electrochemical potential, we can easily have that $\overline{\mu}_1 = \overline{\mu}_{M^{z+}} + z\overline{\mu}_{e^-}; \overline{\mu}_2 = \overline{\mu}_M$ for the reaction $M^{z+} + ze^- \rightarrow M$, where the expressions of $\overline{\mu}_{M^{z+}}$, $\overline{\mu}_{e^-}$ and $\overline{\mu}_M$ are listed below

$$\begin{aligned} \overline{\mu}_{M^{z+}} &= RT \ln a_{M^{z+}} + \mu_{M^{z+}}^0 + zF\varphi_s \\ \overline{\mu}_{e^-} &= RT \ln a_e + \mu_{e^-}^0 - F\varphi_e \\ \overline{\mu}_M &= RT \ln a_M + \mu_M^0 \end{aligned} \tag{12}$$

Here φ_s and φ_e are the electrostatic potential in the electrolyte solution and electrode, respectively. The difference of electrode-electrolyte interfacial potential is $\Delta\varphi = \varphi_e - \varphi_s$. By substituting Eq.(12) back to $\bar{\mu}_1$ and $\bar{\mu}_2$, we can get potential difference $\Delta\varphi^{eq}$ at equilibrium ($\bar{\mu}_1 = \bar{\mu}_2$), as

$$\Delta\varphi^{eq} = E^0 + \frac{RT}{zF}\ln\frac{a_{M^{z+}}a_{e^-}^z}{a_M} \tag{13}$$

where $E^0 = \frac{\mu_{M^{z+}}^0 + z\mu_{e^-}^0 - \mu_M^0}{zF}$ is the standard half-cell potential. Based on the aforementioned diluted electrolytes assumption and the activity of electron is unity, the $\Delta\varphi^{eq}$ can be further simplified as

$$\Delta\varphi^{eq} = E^0 + \frac{RT}{zF}\ln\frac{c_+^*}{a_M} \tag{14}$$

For the non-equilibrium state, the reaction R_e is controlled by the overpotential η, which is defined as[135]

$$\eta = \Delta\varphi - \Delta\varphi^{eq} = \Delta\varphi - E^0 - \frac{RT}{zF}\ln\frac{c_+^*}{a_M} = \frac{\Delta\mu}{zF} = \frac{1}{zF}\sum_i\frac{\delta G}{\delta c_i} \tag{15}$$

To model the Butler-Volmer kinetics, the transition barrier $\bar{\mu}_t^{ex}$ can be defined as[133,135]

$$\bar{\mu}_t^{ex} = RT\ln\gamma_t + (1-\alpha)(zF\varphi_s - zF\varphi_e + \mu_{M^{z+}}^0 + z\mu_{e^-}^0) + \alpha\mu_M^0 \tag{16}$$

So, we have

$$R_e = -R_0\{\exp[\frac{(1-\alpha)\Delta\mu}{RT} - \exp[\frac{-\alpha\Delta\mu}{RT}]\}$$
$$= -R_0\{\exp[\frac{(1-\alpha)zF\eta}{RT} - \exp[\frac{-\alpha zF\eta}{RT}]\} \quad (17)$$

which yields $R_0 = k_0 c_+^{*1-\alpha} a_M^{\alpha} / \gamma_t$, γ_t is the activity coefficient at the transition state which can be derived from the double well function describing the diffusion interface as

$$RT \ln \gamma_t = f_0'(\xi) - \kappa \nabla^2 \xi - RT \ln \xi \quad (18)$$

where $f_0(\xi) = W\xi^2(1-\xi)^2$.

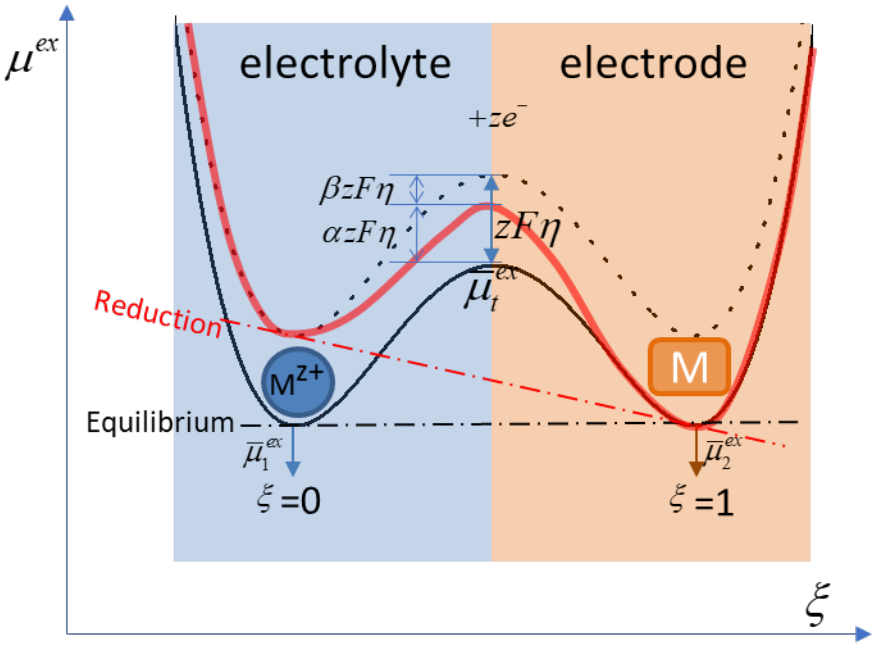

Figure 1-6 Schematic for the excess electrochemical potential at different phases in the electrodeposition reaction, $M^{z+} + ze^- \rightarrow M$ for equilibrium state (black) and reduction state under a negative overpotential (red).

The total overpotential η in Eq.(17) is contributed by two parts, the activation overpotential (η_a) and the concentration overpotential (η_c). They can be defined as

$$\eta_a = \Delta\varphi - E^0$$
$$\eta_c = -\frac{RT}{zF}\ln\frac{c_+^*}{a_M} \tag{19}$$

Based on the definition of activity[133] which is $a_i = \exp(\frac{1}{RT}\frac{\partial f_{mix}}{\partial c_i})$ by $f_{mix} = f_{ch} + f_{grad} - \sum_i c_i\mu_{i0}$, the activity of M metal (a_M) is written as

$$\ln a_M = \frac{f_0'(\xi) - \kappa\nabla^2\xi}{c_s RT} \tag{20}$$

Then the reaction rate R_e can be rewritten as

$$R_e = -R_0\{\exp[(1-\alpha)(\frac{zF\eta_a}{RT} - \ln c_+^* + \ln a_M) - \exp[-\alpha(\frac{zF\eta_a}{RT} - \ln c_+^* + \ln a_M)]\} \tag{21}$$

Physically, the total reaction rate (R_e) can be divided into two parts: interfacial free energy (R_ξ) and the electrode reaction affinity (R_η). According to Eq.(20), a_M is related to the gradient energy term, by which we can rewrite Eq.(21) as

$$R_e = -R_0\{\exp[(1-\alpha)(x+y)] - \exp[-\alpha(x+y)]\} \tag{22}$$

to realize the separation, where $x = \frac{zF\eta_a}{RT} - \ln c_+^*$ for R_η and $y = \ln a_M$ for R_ξ. When a negative electrical potential is applied to the system, making it far from equilibrium, the main driving force should come from R_η which means $R_\eta \gg R_\xi$, yields $x \gg y$. Performing Taylor expansion on Eq.(22), we finally have

$$R_e = -R_0\{\exp[(1-\alpha)x] - \exp(-\alpha x)\} - R_0 y\{(1-\alpha)\exp[(1-\alpha)x] + \alpha\exp(-\alpha x)\} \tag{23}$$

Thus, we can separate R_e into two parts with

$$R_\xi = -R_0 y\{(1-\alpha)\exp[(1-\alpha)x] + \alpha\exp(-\alpha x)\} \tag{24}$$

and

$$R_\eta = -R_0\{\exp[(1-\alpha)x] - \exp(-\alpha x)\} \tag{25}$$

If we ignore the dependence of R_σ on x, by defining an interfacial mobility L_ξ as $L_\xi = R_0 y\{(1-\alpha)\exp[(1-\alpha)x] + \alpha\exp(-\alpha x)\}/c_s RT$ and combining Eq.(20), we then have

$$R_\xi = -L_\xi(f_0'(\xi) - \kappa\nabla^2\xi) \tag{26}$$

Also, by substituting back $x = \frac{zF\eta_a}{RT} - \ln c_+^*$ and $R_0 = k_0 c_+^{*1-\alpha} a_M^\alpha / \gamma_t$, R_η is rewritten as

$$\begin{aligned} R_\eta &= -k_0 c_+^{*1-\alpha} a_M^\alpha / \gamma_t \{\exp[(1-\alpha)(\frac{zF\eta_a}{RT} - \ln c_+^*)] - \exp[-\alpha(\frac{zF\eta_a}{RT} - \ln c_+^*)]\} \\ &= -k_0 a_M^\alpha / \gamma_t \{\exp[(1-\alpha)(\frac{zF\eta_a}{RT})] - c_+^* \exp[-\alpha(\frac{zF\eta_a}{RT})]\} \end{aligned} \tag{27}$$

As the Butler-Volmer kinetics in R_η describe the reaction rate at the sharp interface, which is also the assumption of deriving the total free energy, we add an interpolating function $h'(\xi) = 30\xi^2(1-\xi)^2$ to limit the reaction position. Finally, we have the phase-field variable ξ evolving as

$$\frac{\partial\xi}{\partial t} = -L_\xi(f_0'(\xi) - \kappa\nabla^2\xi) - L_\eta h'(\xi)\{\exp[(1-\alpha)(\frac{zF\eta_a}{RT})] - c_+^* \exp[-\alpha(\frac{zF\eta_a}{RT})]\} \tag{28}$$

where for simplicity, $L_\eta = k_0 a_M^\alpha / \gamma_t$ is set as a constant in this work.

1.5.2 Previous models

Several theoretical models have also been developed to understand the Li dendrite growth mechanism in solid state electrolyte. The pioneer work was done by Monroe and Newman[136,137] for a Li anode/polymer electrolyte half-cell system, they found that the Li dendrite can be stabilized when the shear modulus of the electrolyte is at least twice as that of Li metal. Following their work, Barai *et al.* employed a similar morphological domain for dendrite initiation[138], and studied the external pressure, ionic conductivity, elastic properties, and solid electrolyte grain structure on the Li anode stability[139–142]. Ahmad *et al.* postulated a general criteria for the stability of electrodeposition at electrode-electrolyte interface (EEI) by considering the density change of Li metal[143]. All the models mentioned above are based on the solutions to Nernst-Planck equation in the electrode or electrolyte coupled with the electrochemical reactions. Atomic scale molecular dynamics (MD) simulation and first-principles calculations have also been employed to investigate the grain boundary softening effect[144] and the electronic density of states at the SE surface[145]. However, the electrodeposition process will lead to electrode/electrolyte interface change such as morphology change. These simulations were not able to capture the real morphology of the Li metal dendrite, which could play an important role in determining the mechanical properties of Li metal.

Phase-field simulation has emerged as a versatile mesoscale computation approach to model the temporal and spatial microstructure evolution in various material systems. Unlike conventional mesoscale method, phase-filed method treats the interface between different phases as a diffuse interface, which is characterized by an order parameter that

varies continuously from one phase to another. Thus, the interfacial motion can be explicitly tracked by the evolution of the order parameter. Several phase-field models have been developed to simulate the Li dendrite growth and its morphology evolution. Early work related to the electrochemistry was done by Guyer *et al.*[146,147], who studied the equilibrium and kinetics of the electrodeposition process in a 1D phase-filed model with a linearly kinetics. The first phase-field model coupled with a nonlinear kinetics was developed by Liang *et al.* [148], who introduced the Butler-Volmer kinetics to study the electrolyte/electrode interface motion and later extended to 2D model to simulate the needle-like Li dendrite growth in the battery[149]. Then Chen *et al.* formulated a thermodynamically consistent phase-field model to investigate the effects of the initial anode surface morphology, the applied voltages and the thermal effects on the dendrite patterns[150,151]. Yurkiv *et al.* also built a phase-field model that introduces mechanical properties of solid electrolyte to the existing electrodeposition system to find the correlation between Li dendrite growth and stress field by calculating the elastic[152] and plastic strain[153]. Recently, Hong *et al.* developed a full thermally coupled electrodeposition model to study the self-heating effect that could either accelerate or decelerate the Li dendrite formation[154,155].Tian *et al.*[156] reported a multiscale model coupling Density Functional Theory (DFT) calculations with the phase-field method, which successfully explains the experimentally observed dendrite intergranular growth and revealed that the trapped electrons may produce isolated Li-metal nucleation. Liu *et al.*[157] found that the difference in cation desolvation-induced exchange current is mainly responsible for the dramatically different dendritic Li plating and smooth magnesium (Mg) plating.

The phase-field models above consider the pure liquid/solid electrolytes only, while for composite electrolyte system or anode modification system, it also has the capability to describe the unique properties of a third phase (nanofillers in composite electrolytes or materials for anode modification) by adding an extra order parameter. Li *et al.*[158,159] developed a phase-field model that describe the PPS (polyethyleneimine sponge) modified metal anode limits the dendrite growth by changing the concentration and current density profiles. Wan *et al.*[160] established a composite electrolyte/electrode half-cell system which is based on PI (nanoporous polyimide) film together with PEO/LiTFSI (lithium bis(trifluoromethanesulfonyl)imide) interlayer, indicating the vertical channel enhance the ionic conductivity of the infused polymer electrolyte.

Chapter 2. Methods

2.1 Electrochemical model

2.1.1 Dendrite formation

The simulation system is a standard half-cell system which contains three phases: the Li metal electrode and Li dendrite, the solid polymer electrolyte, and the nanofiller embedded in the solid electrolyte which is as illustrated in Figure 2-1. The solid electrolyte consists of the positively charged Li-ion (Li^+) and the negatively charged anion (A^-). Several assumptions are made to simplify the system, 1) the A^- is set to be immobile so that the Li^+ is the only mobile ion in the system, the A^- is only to ensure the entire system neutrality. 2) a SEI layer is not explicitly incorporated in our model, although it is known to play a significant role during the electrodeposition[161,162].

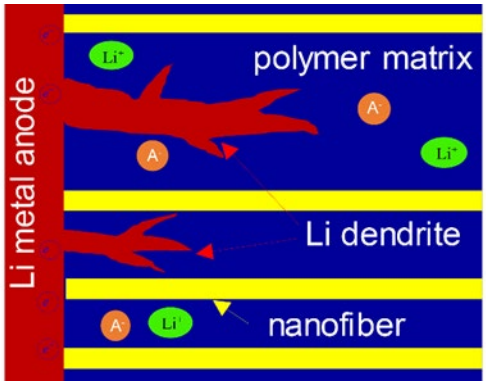

Figure 2-1 Schematic illustration of the half-cell simulation system consisting of the Li metal anode and dendrite, the solid polymer electrolyte and the nanofiber additives, along with the Li^+ cations, anions and electrons that are present in the electrolyte and on the surface of the Li metal anode

To indicate these three phases, we introduce two phase-field variables (ξ, φ), and each with its value ranging from 0 to 1 to describe the aforementioned phases. The phases are differentiate as the Li metal electrode (ξ=1, φ=0), the solid polymer electrolyte (ξ=0,

φ=0) and nanofillers (ξ=0, φ=1), respectively. The order parameters ξ and φ vary continuously from 0 to 1 across the diffuse interfaces at the phase boundaries. Based on that, the total free energy (F) of this half-cell system can be expressed as,

$$F = \int_V [f_{ch}(\xi, \phi, c_i) + f_{grad}(\nabla\xi, \nabla\phi) + f_{elec}(c_i, \varphi) + f_{elas}(\mathbf{F}, \xi)]dV \quad (29)$$

where V is the total volume of the system, f_{ch}, f_{grad}, f_{elec} and f_{elas} represent Helmholtz free energy density, the gradient energy density, the electrostatic energy density, and the elastic energy density, respectively. The first term f_{ch}, chemical free energy density is the summation of a local free energy density (f_0) and the energy of ion mixing (f_{ion}). The energy of ion mixing can be represented as $f_{\text{ion}} = c_0 RT \sum_i c_i^* \ln c_i^*$ in a diluted electrolyte where c_i (i = Li, Li^+ and A^-) denote the concentrations of the Li metal, cation and anion, c_i^* are the dimensionless concentrations ($c_i^* = c_i / c_0$) and c_0 is the standard bulk concentration (c_0=1mol/L). The local free energy density includes two arbitrary double-well function and a cross term, $f_0(\xi, \phi) = W_\xi \xi^2 (1-\xi)^2 + W_\phi \phi^2 (1-\phi)^2 + \frac{A}{2}\xi^2\phi^2$ which yields three minimum values corresponding to the three phases mentioned above. The energy coefficients (W_ξ, W_ϕ) are set to be 0.25 which represent the barrier heightes of the double wells, the cross term is introduced to avoid Li dendrite growth inside the nanofillers by setting the coefficient A/2 as 1.5. The second term f_{grad} which takes the form of $f_{grad}(\nabla\xi, \nabla\phi) = \frac{\kappa_\xi}{2}(\nabla\xi)^2 + \frac{\kappa_\phi}{2}(\nabla\phi)^2$, is the gradient energy density which accounts for the interfacial energy induced at the Li dendrite, solid electrolyte and nanofiller interfaces. The

anisotropy of interfacial energy at the dendrite/solid electrolyte interface which depends on the orientation of the interface will eventually leads to the Li dendritic morphology and can be modeled by expanding the gradient energy coefficient as $\kappa_\xi = \kappa_0[1+\delta\cos(\omega\theta)]$, where δ and ω are the strength and mode of the anisotropy, θ is the angle between the normal vector of the dendrite/electrolyte interface and the reference axis. κ_ϕ is the assumed gradient energy coefficient for the nanofillers which depends on their sizes and shapes. The third term in Eq.(29) is the electrostatic energy density that can be written as $f_{elec}(c_i,\varphi) = \rho\varphi = \sum z_i F c_i \varphi$, where ρ, z_i and F denote the local charge density, charge number of the species c_i and the Faraday's constant, respectively. The last term f_{elas} is the elastic energy density induced by the solid phase deformation, i.e., the induced strain by the Li dendrite growth. The details of elastic energy density will be discussed in the Section 2.3.

The evolution of the system is simulated by solving the non-linear Landau-Ginzburg-Devonshire(LGD) equations for the two phase-field variables ξ and ϕ.

$$\begin{aligned}\frac{\partial\xi}{\partial t} &= -L_\xi\left[\frac{\partial f_{ch}}{\partial\xi} - \kappa_\xi\nabla^2\xi + \frac{\partial f_{mech}}{\partial\xi}\right] \\ &\quad -L_\eta h'(\xi)\left\{c^*_{Li}\exp\left[\frac{\alpha\Delta G(r,t)}{RT}\right] - c^*_{Li^+}\exp\left[-\frac{\beta\Delta G(r,t)}{RT}\right]\right\}\end{aligned} \tag{30}$$

$$\frac{\partial\phi}{\partial t} = -L_\phi\left[\frac{\partial f_{ch}}{\partial\phi} - \kappa_\phi\nabla^2\phi\right] \tag{31}$$

where L_ξ and L_ϕ are the mobility coefficients for ξ and ϕ, L_η is the reaction rate coefficient. The term after L_η is the electrochemical driving force expressed by the Butler-

Volmer equation in which $h(\xi)=\xi^3(6\xi^2-15\xi+10)$ is an interpolating function to limit the driving force at the interface of electrode and electrolyte. $\Delta G(r,t)$ is the thermodynamic driving force of the electrodeposition reaction, and defined as $\Delta G(r,t)=zF\eta_a(r,t)$, where $\eta_a(r,t)$ is the overpotential of the reaction, i.e., the difference between the local electrical potential $\Delta\varphi$ and the standard equilibrium potential E^0 ($\eta_a(r,t)=\Delta\varphi-E^0$). α and β in the second term in Eq. (30) are the charge transfer coefficients ($\alpha+\beta=1$).

For the charged species in the system, we consider A^- to be immobile while electrons are always sufficiently provided at the anode surface. Therefore, the only mobile species of interest is Li^+. Furthermore, the electrochemical reaction ($Li^+ + e^- \leftrightarrow Li$) provides a source term for the generation/annihilation of Li^+ ions. Therefore, the spatial and temporal evolution of c_{Li^+} is described using the Nernst-Planck equation,

$$\frac{\partial c_{Li^+}}{\partial t}=\nabla\cdot\left[D^{eff}_{Li^+}\nabla c_{Li^+}+\mu_{Li}c_{Li^+}zF\nabla\varphi\right]-K\frac{\partial\xi}{\partial t} \tag{32}$$

where the effective diffusivity is interpolated as $D^{eff}_{Li^+}=D^m_{Li^+}(h(\xi)+h(\phi))+D^e_{Li^+}(1-h(\xi)-h(\phi))$. Here $D^m_{Li^+}$ and $D^e_{Li^+}$ are the diffusion coefficients of Li^+ in the Li metal and the electrolyte, respectively. The first two terms on the right side of Eq. (32) are the classic mass diffusion and drift terms. The last term describes the accumulation/annihilation rate of Li^+ due to the electrochemical reaction on the surface of the anode. It is proportional to the phase change rate ($\frac{\partial\xi}{\partial t}$, solved in Eq. (30)) through the accumulation constant (K).

For the electric potential distribution, we assume that the total system always remains charge neutral, and solve the current continuity equation including a source term to describe the current flows. The source term is related to the electrochemical reaction and phase change rate,

$$\nabla \cdot (\sigma^{eff} \nabla \varphi) = R \frac{\partial \xi}{\partial t} \tag{33}$$

where the effective conductivity is interpolated as $\sigma^{eff} = \sigma^m h(\xi) + \sigma^e (1 - h(\xi))$, σ^m and σ^e represent the electronic conductivities in Li metal and the electrolyte. The source term on the right side of Eq. (33) is related to the electrochemical rate and the phase change rate ($R \frac{\partial \xi}{\partial t}$), where R is the current constant.

2.1.2 Dead Li formation model

For the electrochemical model of dead Li formation, it is based on the Li dendrite formation model, plus the introduction of a step function f_d and a positive overpotential $\eta_a(r,t)$ to mimic electro-stripping process. The evolution of the system is described by the following Landau-Ginzburg-Devonshire(LGD) equations,

$$\begin{aligned} \frac{\partial \xi}{\partial t} = & -f_d L_\xi [\frac{\partial f_{ch}}{\partial \xi} - \kappa_\xi \nabla^2 \xi + \frac{\partial f_{mech}}{\partial \xi}] \\ & - f_d L_\eta h'(\xi) \left\{ c_{Li}^* \exp\left[\frac{\alpha \Delta G(r,t)}{RT} \right] - c_{Li^+}^* \exp\left[-\frac{\beta \Delta G(r,t)}{RT} \right] \right\} \end{aligned} \tag{34}$$

where f_d is a step function is written as $f_d = f_{step}(\frac{\varphi}{\varphi_{disch} - 0.01})$ and its value changes from 1 to 0 when $\frac{\varphi}{\varphi_{disch} - 0.01}$ is less than 1. Here φ_{disch} is the discharge voltage which is

a positive value in the dead Li formation process. f_d = 1 denotes the active Li part which is still evolving while f_d = 0 indicates the dead Li part which stops evolving.

2.2 Heat transfer model

The local temperature evolution can be obtained by solving the energy balance equation[151]:

$$C_p^{eff}\rho\frac{\partial T}{\partial t} = \nabla\kappa_{eff}\nabla T + Q \tag{35}$$

where C_p^{eff}, ρ, κ_{eff} indicate the effective specific heat capacity, mass density and effective thermal conductivity, which are decided by the corresponding properties of electrode and electrolyte via the interpolating function $h(\xi)$ in the same way as the diffusivity and conductivity above. The heat generation rate Q is mainly contributed by two parts: the Ohmic heating and overpotential heating when we assume the entropy change during the reaction is ignored, written as,

$$Q = Q_{Ohmic} + Q_{op} \tag{36}$$

where the Ohmic heating can be given by $Q_{Ohmic} = \sigma^{eff}(\nabla\varphi)^2$ and the overpotential heating is express as $Q_{op} = a_s\frac{\partial q}{\partial t}\varphi$. Here a_s is the empirical factor to scale the difference between the simulated value and the experimental value due to the limitation of length scale which leads to the calculated current density is larger than the real one. The charge flow rate $\frac{\partial q}{\partial t}$ can be estimated by:

$$\frac{\partial q}{\partial t} = nFC_m^s \frac{\partial \xi}{\partial t} \tag{37}$$

where F, C_m^s, $\frac{\partial \xi}{\partial t}$ represent the Faraday's constant, site density of the electrode (inverse of the molar volume) and the phase change rate.

2.3 Solid mechanics model

2.3.1 Purely elastic model

In the case of pure elastic effect, the elastic energy density (f_{elas}) is written as $f_{elas} = \frac{1}{2} C_{ijkl} \varepsilon_{ij} \varepsilon_{kl}$, where $C_{ijkl} = \frac{E}{2(1+\nu)}\left(\delta_{il}\delta_{jk} + \delta_{ik}\delta_{jl}\right) + \frac{E\nu}{(1+\nu)(1-2\nu)}\delta_{ij}\delta_{kl}$ is the anisotropic elastic stiffness tensor, and E, ν, δ_{ij} represent the elastic modulus of the entire system, the Poisson's ratio and the Kronecker's delta function. The elastic modulus E is contributed by the Li metal (E^m), the polymer electrolyte (E^e) and the nanofiber (E^f), i.e., $E = h(\xi)E^m + [1-h(\xi)]\{h(\phi)E^f + [1-h(\phi)]E^e\}$, in which $h(\xi)$ and $h(\phi)$ are the interpolating functions for the two phase-field variables that continuously change from 0 to 1. The elastic strain tensor (ε_{ij}) is calculated by using the total strain (ε_{ij}^{total}) minus the local eigenstrain (ε_{ij}^0), the latter of which is caused by the Li dendrite growth and thus can be expressed as $\varepsilon_{ij}^0 = V_{ij}\xi\delta_{ij}$, where V_{ij} is the Vegard strain coefficients obtained from DFT calculation in previous literatures[163]. The total strain ε_{ij}^{total} is assumed to be 0 for simplicity as only one strain component needs to be calculated. To better visualize the strain evolution,

we use the hydrostatic strain (e_h) which is evaluated by averaging the normal strain component, i.e., $e_h = \frac{1}{3}(\varepsilon_{xx} + \varepsilon_{yy} + \varepsilon_{zz})$.

2.3.2 Elasto-plastic model

To obtain the elastic energy density (f_{elas}) in the total free energy of the system (Eq. (29)), the local strain distribution needs to be determined. Based on the continuum mechanics, the displacement of any point in a continum material can be represented as $\mathbf{u} = \mathbf{x} - \mathbf{X}$, where **u** is a continuous displacement field, **x** is the position of that point at time *t*, and **X** is the position at *t*=0. Thus the total deformation gradient is defined as $\mathbf{F}(\mathbf{X},t) = \nabla_X \mathbf{x}$, where ∇_X represents the gradient operator with respect to **X**. The total deformation gradient (**F**) can further be decomposed into the multiplication of three deformation gradients, i.e.,

$$\mathbf{F} = \mathbf{F_e}\mathbf{F_{inel}}, \quad \mathbf{F_{inel}} = \mathbf{F_0}\mathbf{F_p} \tag{38}$$

where $\mathbf{F_e}$ and $\mathbf{F_{inel}}$ represent the elastic and inelastic deformation gradients, the latter of which can be further decomposed into the deformation gradient ($\mathbf{F_0}$) arising from the Vegard strain due to the local concentration inhomogeneity, and the plastic deformation gradient ($\mathbf{F_p}$).

The local phase transformation strain (ε_{ij}^0) caused by the Li dendrite formation (from Li-ion) and growth can be expressed as $\varepsilon_{ij}^0 = V_{ij}\xi\delta_{ij}$, where V_{ij} is the Vegard strain coefficients which can be obtained from previous literature[163], δ_{ij} is the Kronecker's delta function. Then $\mathbf{F^0}$ can be written as $\mathbf{F_0} = \mathbf{I} + \boldsymbol{\varepsilon}^0$ where **I** is the second-order identity tensor.

The mechanical equilibration of the system occurs at the speed of sound, and is much faster than the Li dendrite growth rate. Therefore, a mechanical equilibrium equation will be solved to estimate the hydrostatic and deviatoric stresses across the entire system, i.e.,

$$\nabla \cdot \mathbf{P}^{\mathbf{T}} + \mathrm{f}_V = 0 \tag{39}$$

where **P** is the first Piola-Kirchhoff stress tensor, f_V is the volume forces and will be ignored in this work. **P** is related to the second Piola-Kirchhoff stress tensors (**S**) via $\mathbf{P} = \mathbf{FS}$, where **S** is the second Piola-Kirchhoff stress tensor. It is related to the Cauchy stress (**σ**) as,

$$\mathbf{S} = J\mathbf{F}_{\mathbf{inel}}^{-1}\boldsymbol{\sigma}\mathbf{F}_{\mathbf{inel}}^{-\mathbf{T}}; \quad \boldsymbol{\sigma} = \mathbf{C} : \boldsymbol{\varepsilon}^{\mathbf{e}} \tag{40}$$

where J is the Jacobian operator. It converts the infinitesimal element of the volume in the initial configuration into the corresponding fraction of the volume in the intermediate configuration, i.e., $J = \det(\mathbf{F})$. **C** is the elastic constant tensor written as $C_{ijkl} = \frac{E}{2(1+\nu)}\left(\delta_{il}\delta_{jk} + \delta_{ik}\delta_{jl}\right) + \frac{E\nu}{(1+\nu)(1-2\nu)}\delta_{ij}\delta_{kl}$, where E, ν , δ_{ij} denote the elastic modulus of the entire system, the Poisson's ratio, and the Kronecker's delta function. E is dependent on the elastic modulus of the electrode (E^m) and the electrolyte (E^e), i.e., $E = E^m h(\xi) + E^e(1 - h(\xi))$. Finally, $\boldsymbol{\varepsilon}^{\mathbf{e}}$ is the elastic strain tensor and is written as $\boldsymbol{\varepsilon}^{\mathbf{e}} = \frac{\mathbf{1}}{\mathbf{2}}(\mathbf{F}_{\mathbf{e}}^{\mathrm{T}}\mathbf{F}_{\mathbf{e}} - \mathbf{I})$ where $\mathbf{F}_{\mathbf{e}} = \mathbf{F}\mathbf{F}_{\mathbf{inel}}^{-1}$.

According to the von Mises stress criterion, plastic deformation happens when the von Mises equivalent stress (σ_v) exceeds the yield strength (σ_y). The von Mises

equivalent stress is defined as $\sigma_v = \sqrt{(3/2)\tau_{ij}\tau_{ij}}$, where τ_{ij} is the deviatoric part of Cauchy stress (σ_{ij}), i.e., $\tau_{ij} = \sigma_{ij} - tr(\sigma_{ij})\delta_{ij}/3$. The variation of the yield strength follows the isotropic strain hardening law (Eq. (41)) as,

$$\sigma_y = \sigma_{y_0} + H\varepsilon_{pl}{}^m \tag{41}$$

where σ_{y_0} denotes the initial yield strength, H is the hardening modulus, and m is the hardening exponent. The associated J_2-flow rule is used to obtain the plastic stretch rate as in Eq. (42),

$$\Delta\varepsilon_{ij}^p = \frac{3}{2}\frac{\tau_{ij}}{\sigma_v}\varepsilon_{eq}^p \tag{42}$$

Here $\Delta\varepsilon_{ij}^p$ denotes the incremental plastic strain obtained at each load step, ε_{eq}^p is the equivalent plastic strain rate and can be calculated as $\varepsilon_{eq}^p = \sqrt{\frac{2}{3}\Delta\varepsilon_{ij}^p\Delta\varepsilon_{ij}^p}$. Then the plastic deformation gradient is written as $\mathbf{F_p} = \mathbf{I} + \boldsymbol{\varepsilon}^{\mathbf{p}}$.

By solving Eq. (39), the total deformation gradient **F** can be obtained from $\mathbf{F} = \mathbf{I} + \nabla\mathbf{u}$, where **u** is the displacement field. Once **F** is obtained, the other mechanical field variables, such as the first and second Piola-Kirchhoff stress tensors (**P** and **S**), and the elastic strain tensor ($\boldsymbol{\varepsilon}^{\mathbf{e}}$) can be defined as a function of **F**. Finally, the elastic energy density can be calculated from $f_{elas} = \frac{1}{2}C_{ijkl}\varepsilon_{ij}^e\varepsilon_{kl}^e$, in which ε_{ij}^e is the component of the elastic strain tensor ($\boldsymbol{\varepsilon}^{\mathbf{e}}$).

2.4 Analytical calculation of Effective Li ion conductivity

Several analytical formulations have been proposed to predict the overall effective conductivity of the composites, such as the Brick-Layer Model, the Maxwell Theory (MWT), and the McLachlan's Generalized EMT (GEMT)[164,165]. Here we use the GEMT formulation extended from two-phase to three-phase by following the method developed by Nan and Smith[166] to calculate the effective conductivity of the nanocomposite electrolyte in section 5.3. We assumed that the Al_2O_3 nanofibers are cylindrical morphology. The effective conductivity ($\tilde{\sigma}$) of a composite fiber, which is composed of the Al_2O_3 nanofiber itself and the conductive shell, can be calculated by the following approach,

$$\tilde{\sigma}=\sigma^{f}\tilde{g}+\sigma^{s}(1-\tilde{g}) \tag{43}$$

where the volume fraction of the Al_2O_3 nanofiber in the composite fiber $\tilde{g}$ can be calculated as:

$$\tilde{g}=\frac{r^2}{(r+\delta)^2}=\frac{1}{(1+\alpha)^2} \tag{44}$$

Here r is the radius of the nanofiber, δ is the thickness of the conductive shell, and $\alpha=\delta/r$ is the ratio between the shell thickness and the nanofiber radius. Then the effective conductivity of the entire system can be written as,

$$\sigma_{eff}=\tilde{\sigma}\left(\frac{g}{\tilde{g}}\right)+\sigma^{M}\left(1-\frac{g}{\tilde{g}}\right) \tag{45}$$

in which g is the volume fraction of the Al_2O_3 nanofiber in the entire system, and $g/\tilde{g}$ is the volume fraction of the composite nanofiber in the entire system. Therefore, the effective conductivity curve as a function of the volume fraction (g) consists of two distinct regions. In the first region, the effective conductivity continues to increase with g. This is due to the increasing amount of the highly conductive shell. The turning point indicates that the electrolyte is saturated by the conductive shell and no polymer phase remains when $g = \tilde{g}$. After the threshold, the volume fraction of the conductive shell will not increase, while the volume fraction of the nanofibers continues to increase. Since the nanofiber has the lowest ionic conductivity among the three phases, it results in a decrease of the effective conductivity. For this region, the GEMT equation is written as:

$$g\frac{(\sigma^f)^{1/t}-\sigma_{eff}^{1/t}}{(\sigma^f)^{1/t}+(1/g_e-1)\sigma_{eff}^{1/t}}+(1-g)\frac{(\sigma^s)^{1/t}-\sigma_{eff}^{1/t}}{(\sigma^s)^{1/t}+(1/g_e-1)\sigma_{eff}^{1/t}}=0 \tag{46}$$

The value of t in the Eq.(46) should be chosen to match the experimental results according to Dudney *et. al*[167]. Here we choose $t = 0.625$ to get a good consistency between analytical values and the COMSOL results.

It is seen that the results obtained from numerical simulations and analytical calculations agree well with each other. Both methods show the maximum effective conductivity to be ~ 3.0×10^{-3} S/cm when the volume fraction of the Al_2O_3 nanofiber (V_f) is ~ 40%. This is almost an order of magnitude higher than pure poly(vinylidene fluoride-co-hexafluoropropylene) (P(VDF-HFP)) electrolyte.

2.5 Model implementation

2.5.1 Parameters used in the model

We choose Li metal as the anode material in our system and employ the phase-field model to simulate a realistic $Li^+ + e^- \leftrightarrow Li$ electrodeposition process in a half-cell system. The electrolyte may vary and will be specified in different chapters. The entire model is in two dimension (2D) and is solved by the finite element method on the platform of COMSOL Multiphysics 5.4. The total system size is $9l_0 \times 9l_0$ with an adaptive mesh size from 1.8×10^{-4} to 9×10^{-2} l_0, defined by the COMSOL default extremely fine mode. The Li^+ concentration (c_{Li^+}) is normalized by dividing with the bulk concentration of Li^+ (c_0), i.e., $c^*_{Li^+} = c_{Li^+} / c_0$, where c_0 =1mol/L. Similarly, most parameters are normalized by the characteristic energy density E_0, the characteristic length l_0, the characteristic time step Δt_0, the characteristic strength S_0=1GPa and their combinations. These characteristic values also vary in different chapters, e.g., E_0 =1.5×10^6J/m^3, l_0=100μm, Δt_0=400s in chapter 3 while in chapter 4 and 5, l_0=10μm and 1μm, respectively, the E_0 and Δt_0 will also be modified to keep the real values and normalized values consistent. The charge transfer coefficients are set to be $\alpha = \beta = 0.5$. As only temperature solved by heat transfer model is coupled to the electrochemical model, the heat transfer model is solved in a separate COMSOL preset module with complete unit system, so the parameters related to the heat transfer model are not normalized. All parameters used in chapter 3, 4, 5 and their normalized method are listed in Table 2 unless specified.

Table 2 Parameters used in the phase-field model

Parameters	Symbols	Real Values	Symbols	Normalized Values	References
Interfacial mobility	L_ξ	5.6×10^{-6} $m^3/(J\times s)$	$\tilde{L}_\xi = L_\xi \times (E_0 \times \Delta t_0)$	3333	[168,169]
Reaction constant	L_η	1.39×10^{-6} $m^3/(J\times s)$	$\tilde{L}_\eta = L_\eta \times (E_0 \times \Delta t_0)$	833.25	[168,169]
Gradient energy coeff. 1	κ_0	1.5×10^{-4} J/m	$\tilde{\kappa}_0 = \kappa_0 / (E_0 \times l_0^2)$	0.01	[168,169]
Li^+ diffusivity in the electrode	D^m	2.5×10^{-14} m^2/s	$\tilde{D}^m = D^m / (l_0^2 / \Delta t_0)$	10^{-3}	[168,169]
Li^+ diffusivity in the electrolyte	D^e	2.5×10^{-11} m^2/s	$\tilde{D}^e = D^e / (l_0^2 / \Delta t_0)$	1.0	[170]
Electric conductivity in the electrode	σ^m	1.0×10^6 S/m	$\tilde{\sigma}^m = \sigma^m / (\frac{l_0^2}{\Delta t_0} \bullet \frac{c_0 F^2}{RT})$	10^7	[168,169]
Electric conductivity in the electrolyte	σ^e	1.0×10^{-1} S/m	$\tilde{\sigma}^e = \sigma^e / (\frac{l_0^2}{\Delta t_0} \bullet \frac{c_0 F^2}{RT})$	1.0	[77]
elastic modulus of the electrode	E^m	4.9GPa	$\tilde{E}^m = E^m / 1GPa$	4.9	[136]

Initial yield strength of the electrode	$\sigma_{y_0}^m$	0.4MPa	$\tilde{\sigma}_{y_0}^m = \sigma_{y_0}^m / 1GPa$	4×10^{-4}	171,172
Initial yield strength of the polymer electrolyte	$\sigma_{y_0}^e$	0.77MPa	$\tilde{\sigma}_{y_0}^e = \sigma_{y_0}^e / 1GPa$	7.7×10^{-4}	168 173, 174
Partial molar volume of the electrode	V_m	1.3×10^{-5} m^3/mol	$\tilde{V}_m = V_m \times c_0 / 10^3$	1.3×10^{-5}	136
Partial molar volume of polymer electrolyte	V_e	1.674×10^{-4} m^3/mol	$\tilde{V}_e = V_e \times c_0 / 10^3$	1.674×10^{-4}	136
Lithium transference number	t_{Li^+}	0.3		0.3	136,137
Strength coefficient of the electrode	H_m	1.9MPa	$\tilde{H}_m = H_m / 1GPa$	1.9×10^{-3}	171, 172
Strength coefficient of the electrolyte	H_e	3.5MPa	$\tilde{H}_e = H_e / 1GPa$	3.5×10^{-3}	173,174

Hardening exponent of the electrode	m_m	0.4		0.4	[171,172]
Hardening exponent of the polymer electrolyte	m_e	0.4		0.4	[173,174]
Poisson's ratio	v	0.36		0.36	[152]
Eigenvalues of the strain tensor	V_1	-0.866×10^{-3}		-0.866×10^{-3}	[163]
	V_2	-0.773×10^{-3}		-0.773×10^{-3}	
	V_3	-0.529×10^{-3}		-0.529×10^{-3}	
Charge transfer coefficients	α, β	0.5		0.5	[168,169]
Accumulation constant	K	1.8mol/L	$\tilde{K} = K / c_0$	1.8	[168,169]
Strength of anisotropy	δ	0.02		0.02	[168,169]
Mode of anisotropy	Ω	4.0		4.0	[168,169]
Current constant	R	1.5×10^5J/m^3	$\tilde{R} = R / E_0$	0.1	[168,169]

Thermal conductivity of electrode	κ^m	85W/(m·K)			[175]
Thermal conductivity of electrolyte	κ^e	0.2W/(m·K)			[175]
Specific heat capacity of electrode	$C_{p,m}$	3.55J/(g·K)			[176]
Specific heat capacity of electrolyte	$C_{p,e}$	2.5J/(g·K)			[177,178]
Density of electrode	ρ^m	0.534g/cm^3			[176]
Density of electrolyte	ρ^e	0.95g/cm^3			[179]
Scaling factor	a_s	0.033			[155]
Heat convection coefficient	h	10W/(m^2·K)			[151]
Emissivity	$\in_R$	0.49			[151]
Stefan-Boltzmann constant	σ_R	5.67×10^{-8} W/(m^2·K^4)			[151]

2.5.2 Boundary conditions

For the electrochemical part, zero-flux boundary conditions are applied to the four boundaries for the order parameter ξ . When solving the Li^+ transport and the electrical potential distribution, Dirichlet boundary conditions are applied at the right side and left/right sides of the system, respectively, while zero-flux boundary conditions are used for the other sides. For the heat transfer part, the initial temperature is set as 300K. The convection and radiation boundary conditions[151] are set at the let/right sides of the system, e.g. $\kappa_{eff}(\nabla T)n = h(300-T)+\in_R \sigma_R(300^4-T^4)$ where n is the normal of the boundaries, h is the heat convection coefficient, $\in_R \sigma_R$ are the emissivity and the Stefan-Boltzmann constant, while the upper and lower sides are heat insulation. For the mechanical part, periodic boundary conditions are applied to the top and bottom sides of the system, while fixed constraint boundary conditions are used for the other sides. The 2D approximation is made such that the out-of-plane strain vanishes[180]. All the boundary conditions above are shown schematically in Figure 2-2.

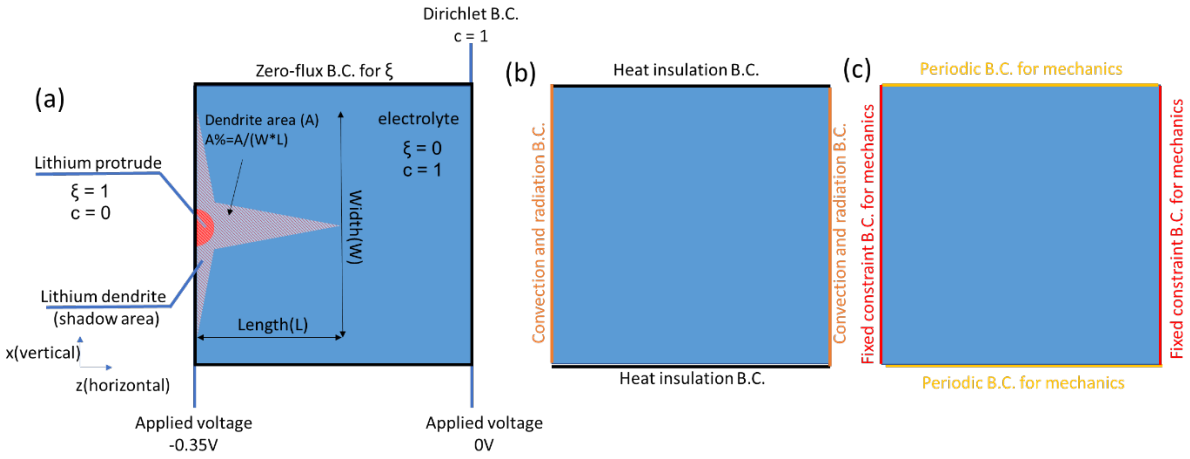

Figure 2-2 Boundary conditions (B.C.) set for the three parts (a)electrochemical part (b) heat transfer part (c) solid mechanics part. (a) also shows the definition of dendrite length (L), width (W) and area ratio (A%).

2.6 Machine learning models

2.6.1 SISSO model

We select four key mechanical properties of the system, i.e., the elastic modulus of the metal electrode (E^m) and the solid electrolyte (E^e), and the initial yield strength of the metal electrode ($\sigma_{y_0}^m$) and the electrolyte ($\sigma_{y_0}^e$) as the primary features (or "fingerprints") to identify the potential materials used for the metal anode and the solid electrolyte in the cell. On the other hand, we employ the vertical length of the dendrite structure ($\tilde{L}$) and the area ratio ($\tilde{A}\%$) as the target properties in the machine learning approach.

To obtain the correlations between the four primary features (E^m , E^e , $\sigma_{y_0}^m$, $\sigma_{y_0}^e$) and the two target properties ($\tilde{L}$, $\tilde{A}\%$), a compressed-sensing method named Sure Independence Screening and Sparsifying Operator (SISSO) is used[181]. The SIS tackles the immense and correlated features, and the SO optimizes the solution from combinations of features. Before building the feature space, the initial yield strengths and elastic modulus are divided by 1MPa and 1GPa respectively to obtain dimensionless results and avoid small number, the target properties, $\tilde{L}$ and $\tilde{A}\%$, are obtained by the dendrite length L and area ratio $A\%$ divided by L_0 and $A_0\%$, respectively, which are the calculated dendrite length and area ratio in the half-cell with PEO electrolyte and lithium metal electrode. To expand the feature space, we assume that the bottom-level feature space (Φ_0) only contains the bottom-level fingerprints, i.e., the four primary features (E^m , E^e , $\sigma_{y_0}^m$, $\sigma_{y_0}^e$). Then the 1st order feature space (Φ_1) will contain complex features (x_j) that are constructed by mathematical operations performed on the bottom-level primary features in Φ_0. We define

an operator (H^m) that includes 10 basic mathematical operations, i.e., H^m ={+, -, ×, /, log, ^-1, ^2, ^3, $\sqrt{}$, $\sqrt[3]{}$, | - |}, in which the superscript (m) indicates that only meaningful combinations are considered by grouping the features with the same unit. Following a similar process, feature spaces of higher order (Φ_2, Φ_3) can also be built from the combinations of H^m and the features in the lower-level feature spaces. The number of features in Φ_1, Φ_2, Φ_3 are calculated to be 54, 3183 and 14360474, respectively.

We use Root Mean Square Error (RMSE) as the metrics of this SISSO model,

$$\text{RMSE} = \sqrt{\frac{1}{n}\sum_{i=1}^{n}(y_i - \hat{y}_i)^2} \tag{47}$$

in which *n* is the number of simulation dataset in the high-throughput database, y_i is the *i*th value obtained from the phase-field simulation, and $\hat{y}_i$ is the *i*th predicted value from the machine learning model. $\hat{y}_i$ is obtained from the summation of all the features (x_j) in the entire feature space ($\Phi_0 \sim \Phi_3$), weighted by their associated coefficients (θ_j), i.e., $\hat{y}_i = \sum_{j=1}^{m} \theta_j x_j$, which provides a quantitative prediction of the target properties. The regularizer or the sparsifying operator in this model is 'L_0', which is written as,

$$L_0 = \sum_{j=1,\theta_j \neq 0}^{m} \theta_j^0 \tag{48}$$

where θ_j is the *j*th coefficient and *m* is the number of coefficients. Both RMSE and L_0 are minimized during the machine learning process to extract the best *n*D descriptors.

A total of 2337 phase-field simulation results from different combinations of the initial four features are performed to generate a high-throughput database. These datasets are split into the training and test dataset with the ratio of 8:2 after random shuffle. A total of 1870 simulation results are used to train the SISSO model and obtain the corresponding analytical equations, while the remaining 467 simulation results are only used to test and evaluate the trained SISSO model.

2.6.2 Deep Neural Network (DNN) model

To benchmark the SISSO model, an additional Deep Neural Network (DNN) model is also implemented which belongs to supervised learning models. It needs the dataset which contains both the input and corresponding output. After random shuffle, the whole dataset is split into train set, validation set and test set which are 64%, 16% and 20% of the whole dataset, respectively. The DNN consists of 4 hidden dense layers with 64 neurons in each layer and the activation function is ReLu function[182]. So for each neuron, it can be expressed as

$$h_j = \max(0, \sum_{i=1}^{n} \theta_i x_i + b) \tag{49}$$

where h_j means jth neuron, x_i , θ_i and b represent the input from previous layer, its corresponding weight and bias, respectively, and n is the number of inputs from previous layer. The optimizer which is for the update of θ_i and b is set to be RMSprop[183] with a learning rate of 0.0005. A dropout layer[184] of 10% rate is added after the 2nd hidden layer and L_1_L_2 regularization[185,186], namely, elastic net is used at the output layer with $l_1=5\times10^{-4}$ and $l_2=2\times10^{-3}$. Both are the widely used methods to prevent neural networks from

overfitting. After training, the coefficient of determination, denoted R^2, is used to evaluate the model by comparing the model prediction results and true values in the testing set. R^2 formula is as below:

$$R^2 = 1 - \frac{\sum_{i}^{n} (y_{true,i} - y_{pred,i})^2}{\sum_{i}^{n} (y_{true,i} - \bar{y})^2} \tag{50}$$

n is the size of test set, $y_{pred,i}$ and $y_{true,i}$ are the model predicted value of *i*th sample in test set and its corresponding true value, $\bar{y}$ is the mean of test set. The value of R^2 gets closer to 1 means the better prediction accuracy.

2.7 Density functional theory calculations

All calculations related to the Zn battery solvation energy in this study are performed by Vienna Ab Initio Simulation Package (VASP), which is a plane wave based density functional theory (DFT) code[187–190]. Projector Augmented Wave (PAW) approach is used to describe the electron-ion interaction, and Perdew-Burke-Ernzerhof (PBE) functional with Generalized Gradient Approximation (GGA)[191] is used for exchange correlation. The size of the supercell is chosen to be 20Å×20Å×20Å, while the k-points sampling is set as (2×2×2) with an automatically generated mesh in the first Brillouin Zone[192]. A cutoff energy of 400eV is used for all the calculations and the energy convergence criterion for the structural optimization is 10^{-6}eV. Van der Waals correction has been considered in all calculations. The solvation energy (E_{sol}) of the Zn^{2+} ion in aqueous electrolyte with/without the addition of THF is calculated as follows[157]:

$$E_{sol} = E_{total} - E_{H_2O/THF+H_2O} - E_{Zn^{2+}} \quad (51)$$

where E_{total} is the total energy of the Zn^{2+} solvation structures configured with H_2O and THF molecules. $E_{H_2O/THF+H_2O}$ and $E_{Zn^{2+}}$ are the energies of the H_2O/ H_2O+THF molecule clusters and the isolated Zn^{2+} ion, respectively.

Chapter 3. Electrodeposition behavior under different diffusion and reaction rates

3.1 Dendrite growth in bare solid electrolyte

We start with a planar electrode with poly(vinylidene fluoride-co-hexafluoropropylene) (PVDF-HFP) as solid electrolyte as shown in Figure 3-1(a). In this section, the mechanical effect is not considered, and the system size is chosen to be 900 μm ×900 μm with t_0 equals to 50s. In the initial state, the electrode/electrolyte interface is flat (Figure 3-1 (a)). At 250s, the interface moves to towards the electrolyte, and small protrudes are seen (Figure 3-1 (b)). However, after 250s evolution, there is almost no growth in bulk while the small Li protrudes continue to grow into large dendrites as shown in Figure 3-1 (c). This is due to the uneven electrodeposition rate of Li ions at the surface, when a rough surface is generated, the irreversible dendrite growth will happen. From Figure 3-1 (d), it is clearly seen that the temperature of Li metal electrode can reach up to 328K which is also close to the real values[193]. The Li-ion concentration gradient and electrostatic potential gradient at the Li metal/electrolyte interface as shown in Figure 3-1 (e)(f) induce a large electrochemical driving force for the Li dendrite growth, based on the Butler-Volmer kinetics in Eq.(30). Comparing with the experimental results, the smooth Li anode surface is similar to that as shown in Figure 3-2(b)&(d), while the small protrude surface morphology looks like the dendritic morphology shown in Figure 3-2 (a)&(c).

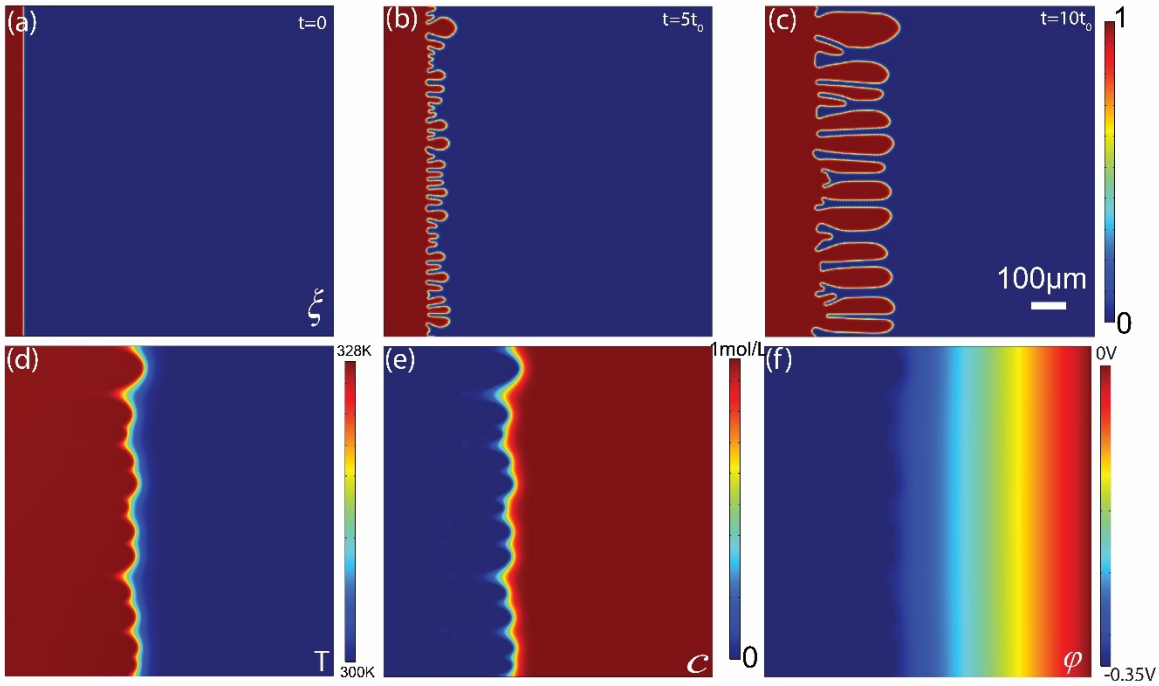

Figure 3-1 Phase-field Simulation results starting from a planar electrode. (a-c) morphology evolution at (a)t=0 (b)t=5t0 (c)t=10t0 and the related (d) temperature distribution, (e)concentration profile and (f)potential distribution. Here t0 equals 50s.

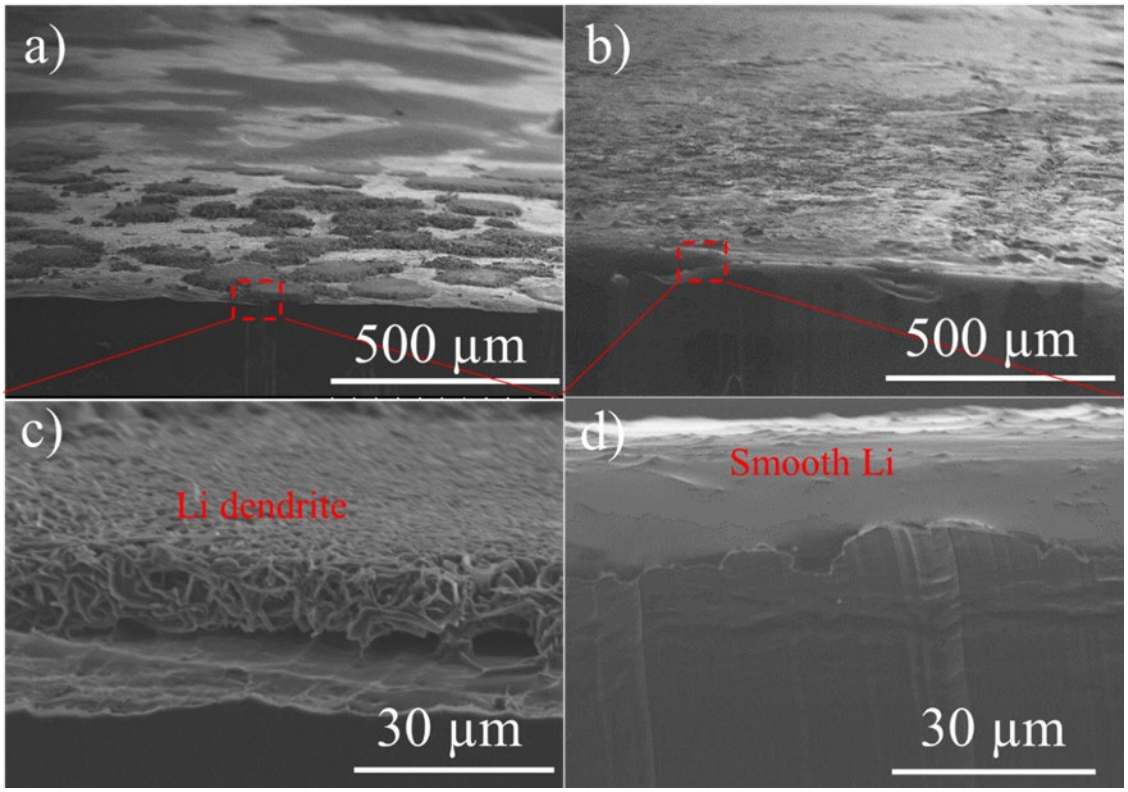

Figure 3-2 SEM image of comparison between the (a)(c) Li dendrite morphology and (b)(d) smooth Li surface. (Figures provided through the courtesy of Prof. Yue Zhou from South Dakota State University)

3.2 Effect of Li-ion diffusion barrier on the electrodeposition behaviors

To further understand the effects of Li-ion diffusion rate and electrodeposition rate on the Li dendrite growth, we first modify the diffusion rate by changing the diffusion barrier (E_d) at a fixed deposition rate (E_a=0.15eV). The relation between Li-ion diffusivity (D) and the diffusion barrier is expressed as $D = D^0 \exp(-\frac{E_d}{RT})$ where the D^0 is the standard diffusion coefficient for 1M electrolyte. Based on this expression, Li-ion diffusivity is dependent on both the local temperature and the diffusion barrier, the latter of which varies among different types of solid electrolyte For simplicity, we vary E_d from 0.05eV to 0.15eV[155]. Figure 3-3 (a)-(c) illustrates the final morphologies of Li metal/solid

electrolytes after 500s evolution. It is seen that when the diffusion barrier increases from 0.05eV to 0.15eV (corresponding to the decrease of Li-ion diffusivity), the electrode/electrolyte interface changes from a smooth surface to a rough surface with small protrudes of Li metal, and finally to a Li dendrite morphology. This indicates that a lower Li-ion diffusion rate is responsible for the Li dendrite growth. It has been previous reported that the fast Li ion transfer provides sufficient cations in all directions and creates a smooth surface[194]. Therefore, we further plotted the 1D Li-ion concentration profiles along the horizontal directions with different magnitudes of E_d's. It is seen that when E_d =0.05eV and 0.10eV (black and blue curves), the Li-ion concentration decrease smoothly near the interface due to a relatively large Li-ion diffusivity, which promotes a smooth EEI due the Li deposition. On the contrary, when E_d = 0.15eV (red curve), a sharp Li-ion concentration gradient is seen at the EEI, causing Li dendrite formation and growth during the electrodeposition. Our simulation reveals that the Li-ion diffusivity could play a key role in determine the morphology of the EEI, which agrees with previous studies[194].

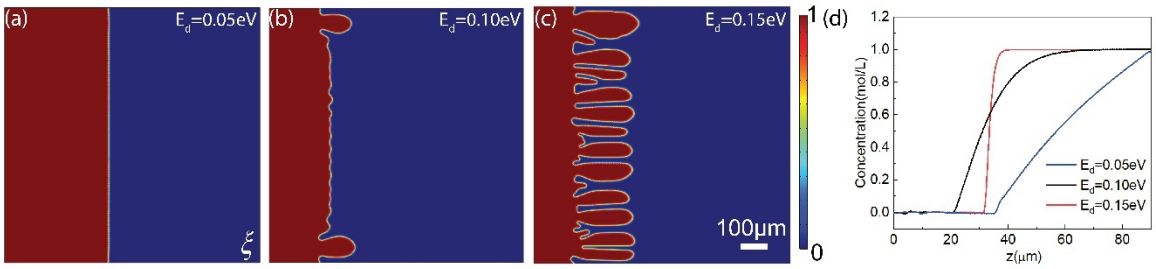

Figure 3-3 Dendrite growth under different diffusion barriers (a) 0.05eV (b) 0.10eV (c) 0.15eV and (d) corresponding concentration gradient along horizontal direction.

3.3 Effect of reaction barrier on the electrodeposition behaviors

To understand the effect of electrodeposition reaction rate on the Li dendrite growth, we fix the diffusion rate at E_d=0.15eV and modifying the reaction rate. The reaction rate is related to the reaction energy barrier E_a as $R = R^0 \exp(-\frac{E_a}{RT})$, where R^0 is the standard reaction rate in 1M electrolyte. Here we chose E_a from 0.15eV to 0.25eV[155].Figure 3-4 (a)-(c) illustrates the final morphologies of Li metal/solid electrolytes after 500s evolution. It is clearly seen that under lower reaction barrier (higher reaction rate), Li dendrites form and grow (Fig. 3-3 (a)). When the reaction barrier increases (reaction rate decreases), the Li dendrite is inhibited and eventually form a relatively smooth EEI. It is also seen that the difference in EEI morphology is almost negligible when E_a is greater than 0.20eV. To further understand this behavior, we compared the 1D reaction rate (R) along horizontal direction for all three cases. (Figure 3-4(d)). It is seen that the overall reaction rate of E_a = 0.15eV is much higher than the other two, while the reaction rates under the reaction energy barriers of 0.20eV and 0.25eV are pretty close. It has been previous reported that a larger reaction barrier which corresponds to a lower intrinsic exchange current and reaction rate leads to a non-dendritic morphology. Thus our simulation results agree well with previous reports[157].

In a brief summary, the dendrite may grow under a low diffusion rate or a high reaction rate. When the diffusion rate is low, there will be insufficient Li ions transported to the electrode surface. This causes Li ions to accumulate at the protrude of the surface as it has a relatively shorter transport pathway than the rest of the electrode surface. As a result, these protrudes preferably grow into a minor dendrite which further shorten the transport pathway in a self-accelerating way, and finally promote the Li dendrite growth.

The high reaction rate also plays a similar role as the low diffusion rate. High reaction rate makes the Li ion deposit to the electrode surface rapidly, which creates an area with insufficient Li ions near the surface. Then it will fall to the cycle of low diffusion rate described above.

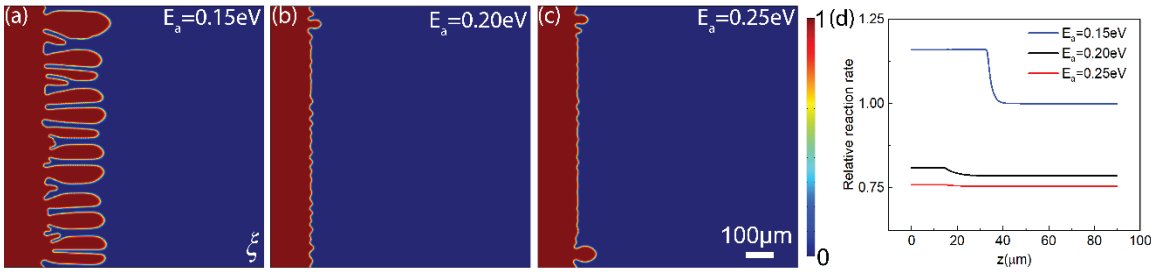

Figure 3-4 Dendrite growth under different reaction barrier (a) 0.15eV (b) 0.20eV (c) 0.25eV and (d) corresponding reaction rate along horizontal direction.

Chapter 4. Dendrite inhibition by mechanical effects

4.1 Purely elastic strain effect on the Li dendrite growth

We start with a bare solid electrolyte, poly(vinylidene fluoride-co-hexafluoropropylene) (P(VDF-HFP)) whose elastic modulus is 5GPa, in the absence of nanofiller additives. Here we focus on a single dendrite to avoid the interference among multiple Li dendrites, and to obtain a better understanding of how the mechanical properties of the solid electrolyte would have effects on the dendrite growth. Therefore, the system size is set as 90×90μm with t_0=5s. The initial state of the system consists of a solid electrolyte phase of high Li^+ concentration, with a small protrude of Li metal located at the Li anode/solid electrolyte interface representing the nucleation of a Li dendrite, where Li^+ concentration is zero, as shown in Figure 4-1(a), (e). The electrical potential is fixed at the anode (φ =-0.35V) and the right end of the simulation size (φ =0.0V), and linearly increases in the system in the initial state (Figure 4-1(i)). In this and next models, the temperature is set to be uniform as 300K in the system. We choose elastic strain ε_{ij} = 0 inside the electrolyte as the reference state (Figure 4-1(m)). The initial Li^+ concentration (c_{Li^+}), electrical potential (φ) distribution, and hydrostatic elastic strain (e_h) are also shown in (e), (i) and (m), respectively, and they remain the same for all other simulations hereafter unless otherwise specified. During the charging process, the Li metal nucleate grows into a tree-like morphology and the corresponding Li^+ concentration and electrical potential are obtained by solving Eqs.(30)(32)(33), as shown in Figure 4-1 (a) ~ (p). This results in a large concentration gradient and an electric potential gradient in the vicinity of the Li metal/electrolyte interface, giving rise to a large overpotential that acts as the driving force

of Lithium dendrite growth. Meanwhile, the overpotential is also seen at the interfacial region due to the differences in the electrical conductivity of the Li metal and the electrolyte. Since the pure electrolyte is chosen as the reference state with zero strain, the penetration of Li dendrite into the electrolyte induces a local compressive strain (Figure 4-1 (m) ~ (p)). Furthermore, the surface tension is lower at the tip of the deposit based on $\kappa_{\xi} = \kappa_0[1 + \delta\cos(\omega\theta)]$, such that the deposit has a preference to grow at the dendrite tip. On the other hand, the Li^+ concentration gradient at the tip becomes even higher, causing the whole deposit to grow in a dendrite morphology. The lithium dendrite growth begins when there is a positive lithium-ion concentration gradient. Our model is thus able to capture the Li dendrite morphology and growth kinetics, and yield results that are in agreement with previous literature[168,169].

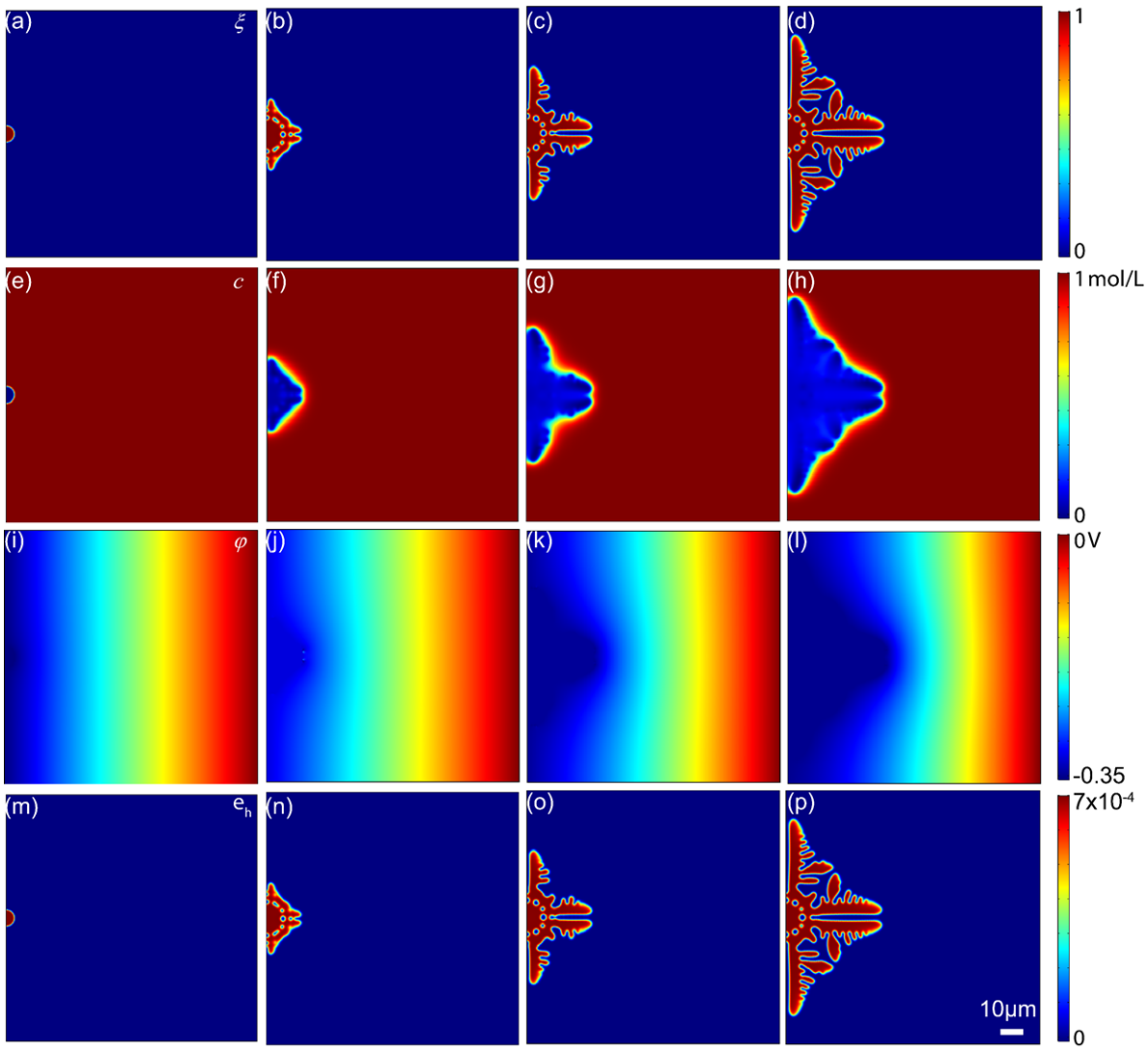

Figure 4-1 Phase-field Simulation of the evolution of Li dendrite structure (represented by the phase field variable ξ, (a) ~ (d)), the Li ion concentration c, (e) ~ (h), the electric potential distribution ϕ, (i) ~ (l) and the elastic strain eh, (m) ~ (p) at different time steps. (a), (e), (i), (m): t = 0; (b), (f), (j), (n): t = 3.3t_0; (c), (g), (k),(o): t = 6.7 t_0; (d), (h), (l), (p): t = 10 t_0). Here t_0 equals 5s.

We then incorporate the mechanic interaction between the Li metal and the electrolyte by setting E^m = 4.9 GPa, and modifying E^e from 1.0 to 17.0 GPa to represent the different solid electrolyte materials. Figure 4-2(a)-(e) illustrate the Li dendrite morphology after same evolution time in solid electrolytes of different elastic moduli. It is seen that the electrolyte with smaller elastic modulus than the Li metal promotes the

dendrite growth (Figure 4-2(a), (b)), while those with larger elastic modulus than the Li metal inhibits the dendrite growth (Figure 4-2(d) and (e)). These results are in good agreement with well recognized argument that dendrite growth can be effectively suppressed when the elastic modulus of the SE is twice of that of Li metal[136]. To further understand it, we compare the mechanical driving force at the electrode-electrolyte interface for the Li dendrite growth, calculated as $-\frac{\partial f_{mech}}{\partial \xi}$ (Figure 4-2 (f) ~ (j)) and the sum of the remaining driving force $-\frac{\partial (f_{ch}+f_{grad}+f_{elec})}{\partial \xi}$ (Figure 4-2 (k) ~ (o)). Here we only plot the mechanical driving force at the interface, which plays a dominant role in the Li dendrite evolution. Meanwhile the driving force inside the Li metal and the electrolyte remains constant and has less effect on Li dendrite growth. It is seen that the remaining driving forces at the dendrite tip remain positive in all cases, indicating that the electrochemical reaction as described by the Butler-Volmer kinetics favors the dendrite growth. On the other hand, the mechanical driving force at the interface ranges from -9.0 to 3.0 (10^{-3} J/m^3), which is close to and partially offsets the remaining driving force. When E^e is smaller than E^m, the mechanical driving force is positive (Figure 4-2(f), (g)), which favors the ξ evolution from 0.0 to 1.0, i.e., the Li dendrite growth in the electrolyte is further promoted. This driving force further increases when the difference (E^m - E^e) enlarges resulting in a larger dendrite size. When E^e is larger than E^m, the mechanical driving force becomes negative (Figure 4-2(i), (j)), which favors the ξ evolution from 1.0 to 0.0, i.e., the Li dendrite growth is inhibited. Our results imply that the relative magnitude of the elastic

modulus between the Li metal and electrolyte determines whether the dendrite growth is promoted or suppressed.

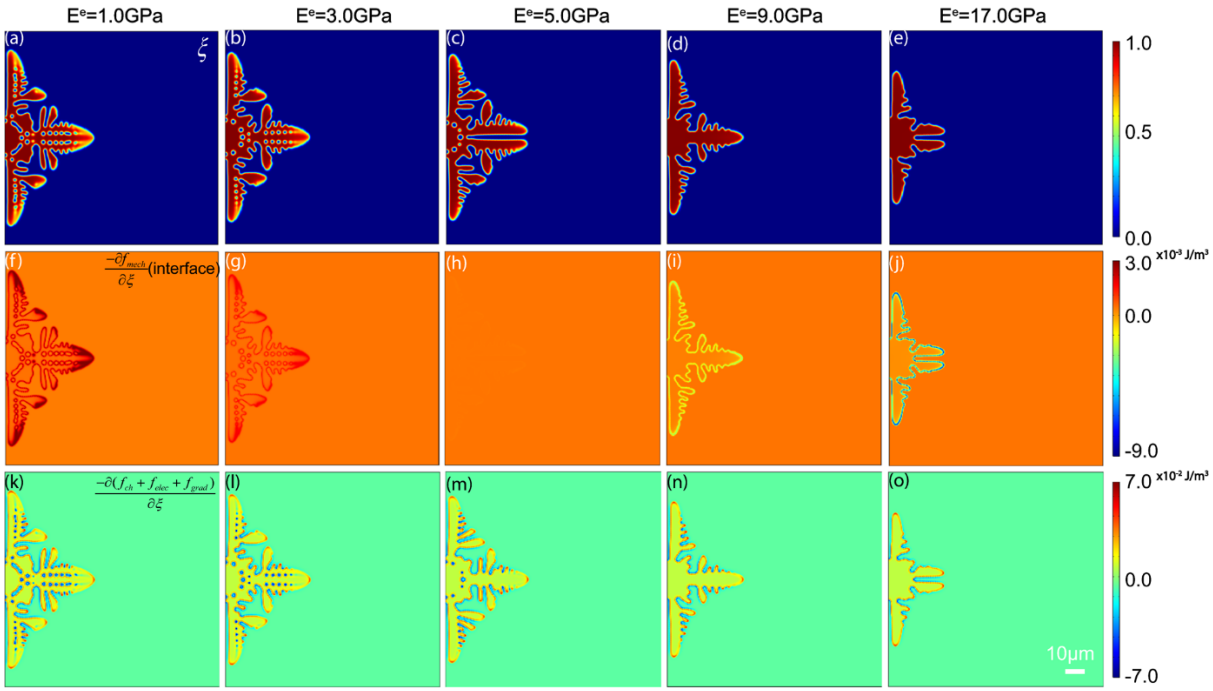

Figure 4-2 Phase-field simulation results of Li dendrite growth in pure polymer electrolyte of various elastic modulus ranging from 1.0GPa to 17.0GPa. (a) ~ (e) the phase-field variable after $10t_0$ evolution; (f) ~ (j) the mechanical strain driving force at the electrode-electrolyte interface; (k) ~ (o) the sum of the remaining driving force from chemical bulk energy, electrostatic energy and gradient energy

4.2 Elasto-plastic effect on the Li dendrite growth

We start with the case when the Li dendrite grows inside the PEO polymer electrolyte. The elastic modulus of the electrolyte is set as 0.3GPa and the yield strength is set as 0.77MPa. Figure 4-3 shows the temporal evolutions of the Li dendrite morphology (ξ), lithium-ion concentration (c_{Li^+}), electrical field component distribution (E_x), local hydrostatic strain (ε_h), and equivalent plastic strain (ε_{eq}^p), respectively. First, a lithium

protrude is introduced at the center of the Li anode surface to mimic the surface roughness (Figure 4-3 (a)). Under an applied bias of -0.35V, the Li ions segregate in the vicinity of the protrude due to the local electric field enhancement, and are subsequently reduced to Li metal by the electrons in the electrode. This results in a progressive growth of the Li protrude into a dendrite morphology under inhomogeneous interfacial energy (Figure 4-3(b)-(d)). Figure 4-3(e) illustrates the 1D temporal evolutions of the Li^+ concentration (c_{Li^+}), and the electric field component (E_x) along the direction as indicated by the arrows in 2D plots in Figure 4-3(e), respectively. The largest variations of c_{Li^+} and E_x are seen at the Li dendrite/electrolyte interface, causing large gradients of c_{Li^+} and E_x that lead to a large electrochemical driving force based on the Butler-Volmer kinetics (Eq.(30)), which eventually promotes the Li dendrite growth. The electric field (E_x) variation along tip directions indicates that the maximum electric field at the tip region increases over time, which implies that the Li dendrite structure is a self-accelerating process, in agreement with previous reports[195]. The hydrostatic strain $\varepsilon_h = \frac{1}{3}(\varepsilon_{11}^e + \varepsilon_{22}^e + \varepsilon_{33}^e)$ and equivalent plastic strain ε_{eq}^p are further plotted in Figure 4-3(f)-(g). The hydrostatic strain reaches the maximum value (~3.5×10^{-4}) near the electrode-electrolyte interface, while that in the interior region of Li metal is around 3×10^{-5}. It is noteworthy that there also exists a substantial hydrostatic strain in the electrolyte region near the bevel edge of dendrite, and the size of this region increases with the dendrite growth. The equivalent plastic strain mainly exists inside the lithium metal. Its magnitude of the highest value at some point is almost an order of magnitude higher than the hydrostatic strain, indicating a significant plastic deformation in the Li metal due to its low initial yield strength.

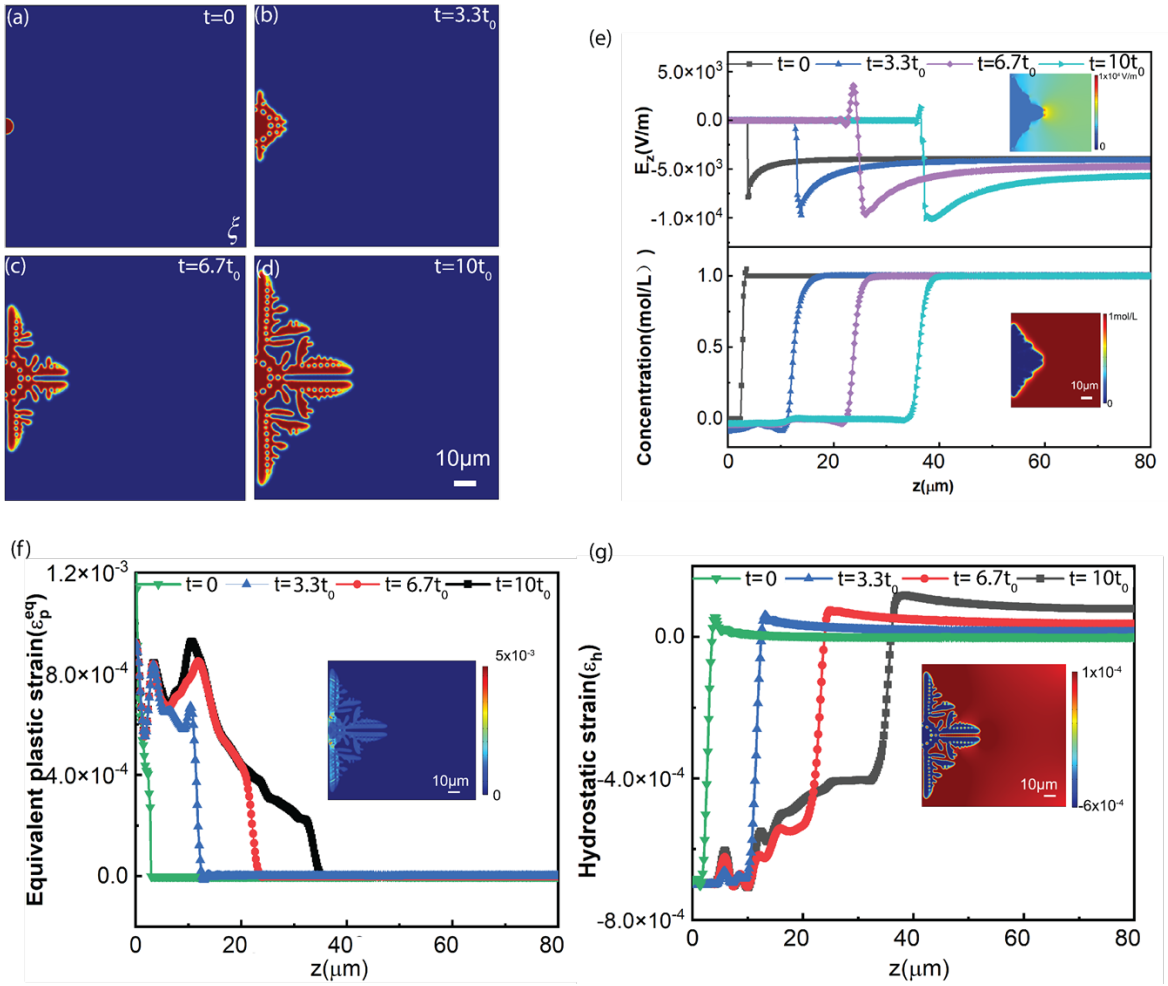

Figure 4-3 Phase-field simulation results of Li dendrite growth in PEO. (a)-(d) the temporal evolution of dendrite morphology from 0s to $10t_0$, (e) Evolutions of Li-ion concentration (c_{Li^+}) (lower) and the electrical field component (E_z) (upper) along the arrow segment indicated in the inset figures, (f) equivalent plastic (ε_{eq}^{p}) and (g) hydrostatic strain (ε_h) evolution with time along the arrow segment indicated in the inset figures. Here t_0 equals 5s.

4.2.1 Effect of elastic modulus of solid electrolyte on the dendrite growth

To further understand the mechanical properties of the solid electrolyte on the Li anode stability, we simulate the Li dendrite growth behavior in solid electrolyte with

various elastic modulus (E^e) that ranges from 5.0 to 50GPa. While the yield strength of the solid electrolyte ($\sigma^e_{y_0}$) usually increases with increasing E^e , here we assume that $\sigma^e_{y_0}$ is fixed to be 7.7MPa in all cases to better understand the elastic effect of the electrolyte. The elastic modulus (E^m) and the yield strength ($\sigma^m_{y_0}$) of the Li metal electrode are chosen to be 5GPa and 0.4MPa, respectively. Figure 4-4 (a)-(d) illustrate the final morphology of the Li dendrites after evolving for 50s in solid electrolyte of different elastic moduli (E^e). It is clearly seen that when E^e increases, the dendrite growth is inhibited in the horizontal direction (along *z*). This trend agrees well with our previous work and the well-recognized theory[136,196]. To further understand this effect, we compare the elastic driving force at the electrode-electrolyte interface, calculated as $\frac{-\partial f_{elas}}{\partial \xi}$ (Figure 4-4(e)-(h)), with the sum of the remaining driving force $\frac{-\partial (f_{ch} + f_{grad} + f_{elec})}{\partial \xi}$. The sum of the remaining driving force is found to be positive along the Li/electrolyte interface, indicating that the electrochemical reaction as described by the Butler−Volmer kinetics favors the Li dendrite growth. Furthermore, the remaining driving forces are almost constant (~6×10^{-2} J/m^3) in all cases, due to the fact that the gradients of the Li^+ concentration and the electrical potential that determine the Butler−Volmer kinetics are less dependent on the elastic modulus of the electrolyte. In contrast, the elastic driving force at the interface varies from -3 to -12 (10^{-3} J/m^3) when E^e changes from 5.0 to 50GPa. Since a negative elastic driving force favors the ξ evolution from 1.0 to 0.0, i.e., the Li dendrite growth is inhibited, thus a more negative elastic driving force due to a larger elastic modulus of the electrolyte can better

offset the positive remaining driving force, and finally lead to a better Li dendrite inhibition effect. The von Mises stress distributions (Figure 4-4(i)-(l)) indicate that the plastic yielding could occur based on the overall level of deviatoric stress τ_{ij}. It is seen that larger deviatoric stress (light blue region) is mainly distributed at the tips of the dendrite, and in the spacings between neighboring Li dendrite branches. The magnitude of the von Mises stress increases with increasing E^e.

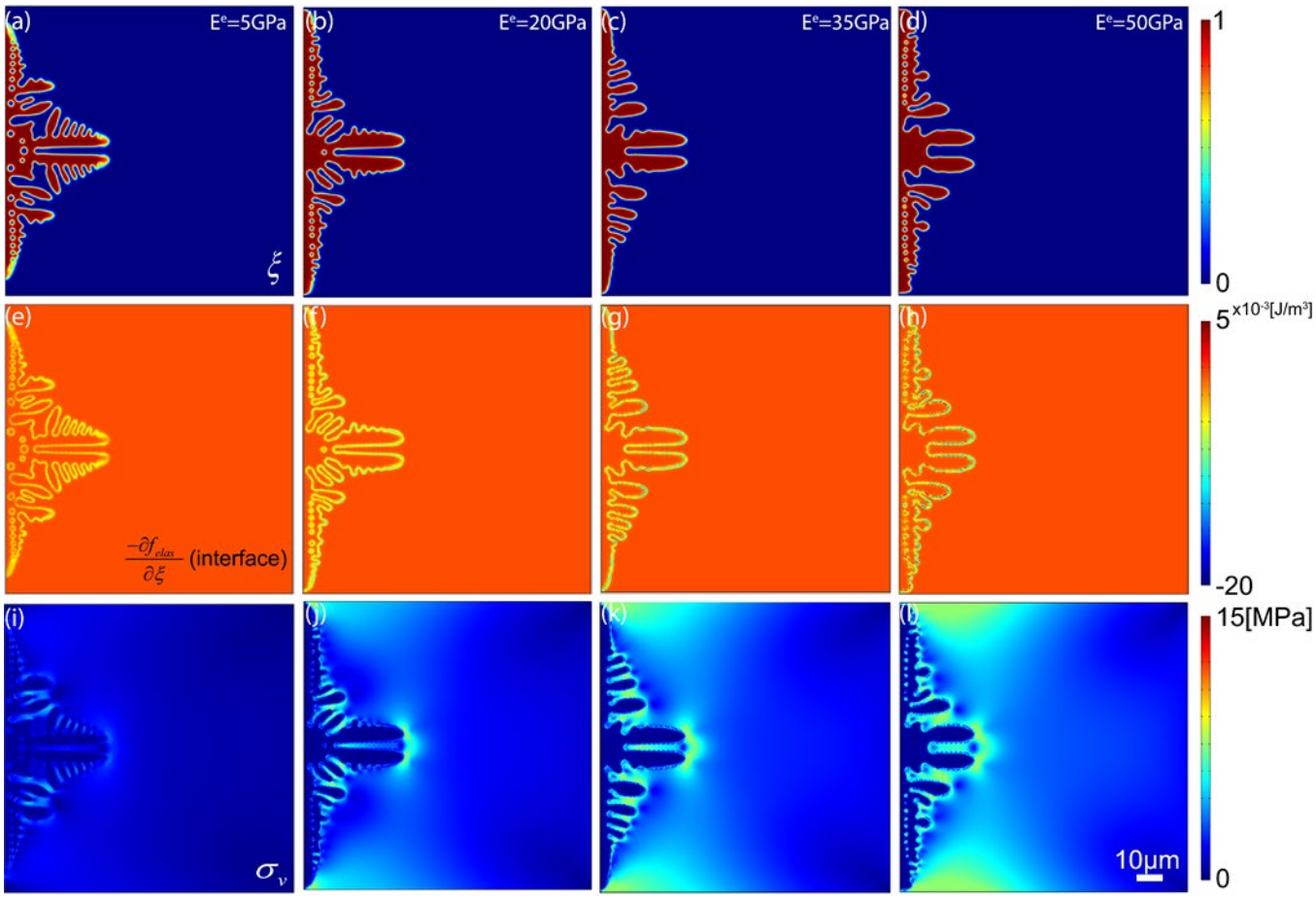

Figure 4-4 Dendrite morphology (a)-(d), the corresponding elastic driving force (e)-(h) and the von Mises stress distribution (i)-(l) from the phase-field simulation results after 50s evolution in solid electrolytes of different elastic moduli (Eᵉ). The elastic moduli of the electrolyte are (a)5GPa; (b) 20GPa; (c) 35GPa; (d) 50GPa. The yield strength of the electrolyte ($\sigma_{y_0}^e$) is fixed to be 7.7MPa.

4.2.2 Effect of yield strength of solid electrolyte on the dendrite growth

We further study the effect of yield strength of the solid electrolyte ($\sigma_{y_0}^e$) on the Li dendrite growth. Here the magnitude of $\sigma_{y_0}^e$ is selected to be from 0.77 to 77MPa, while the elastic modulus of the electrolyte is fixed to be 35GPa. The elastic modulus and the yield strength of the metal electrode are chosen to be the same as in section 4.2. Figure 4-5 (a)-(c) illustrates the final morphology of Li dendrite after 50s evolution. It is seen that the Li dendrite growth is effectively inhibited when $\sigma_{y_0}^e$ increases from 0.77MPa to 7.7MPa (Figure 4-5(a)-(b)). This is because of the decrease of the elastic driving force at the electrode-electrolyte interface, which inhibits the Li dendrite growth (Figure 4-5(d)-(e)). However, when $\sigma_{y_0}^e$ further increases from 7.7MPa to 77MPa, the vertical length of the dendrite remains almost the same (Figure 4-5 (b)-(c)), indicating that the inhibition effect is less significant when $\sigma_{y_0}^e$ is above 7.7MPa (Figure 4-5 (e)-(f)). To further understand this trend, we compare the distributions of the von Mises stress (σ_v) under different $\sigma_{y_0}^e$ s (Figure 4-5(g)-(i)). The maximum deviatoric stress is found to be inside the electrolyte and close to the electrode-electrolyte interface. Furthermore, the maximum deviatoric stress does not exceed the yield strength of the electrolyte. When $\sigma_{y_0}^e$ increases from 0.77MPa to 7.7MPa, the maximum σ_v also increases accordingly, which acts as the major inhibition factor to the Li dendrite growth. However, when σ_v reaches its maximum value under given E^e (~10 MPa for E^e =35GPa in this case), further increase of $\sigma_{y_0}^e$ (from 7.7MPa to 77MPa) can no longer enhance the deviatoric stress to further inhibit the Li dendrite growth (Figure 4-5(i)). This is further illustrated in a schematic stress-strain curve

of the solid electrolyte with different $\sigma_{y_0}^e$'s (Figure 4-5(j)). Under a smaller $\sigma_{y_0}^e$ (case 1), the maximum deviatoric stress (σ_v^1) with a given deformation strain is mainly limited by the initial yield strength of the electrolyte ($\sigma_{y_0}^e$). In this case, the increase of $\sigma_{y_0}^e$ (from case 1 to 2) gives rise to a larger deviatoric stress (σ_v^2) to effectively suppress the Li dendrite growth. However, when $\sigma_{y_0}^e$ exceeds the maximum limit of the deviatoric stress that could be induced under given elastic modulus, further increase of $\sigma_{y_0}^e$ (case 2 to 3) could no longer enhance σ_v^2, and is less effective in the Li dendrite suppression. In this case, the Li dendrite can only be inhibited by further increasing the elastic modulus of the solid electrolyte (case 4 ~ 6 in Figure 4-5(k)). Therefore, effective inhibition of the Li dendrite growth requires both a large elastic modulus that is able to induce large deviatoric stress, and a corresponding yield strength that allows the deviatoric stress to reach its maximum value.

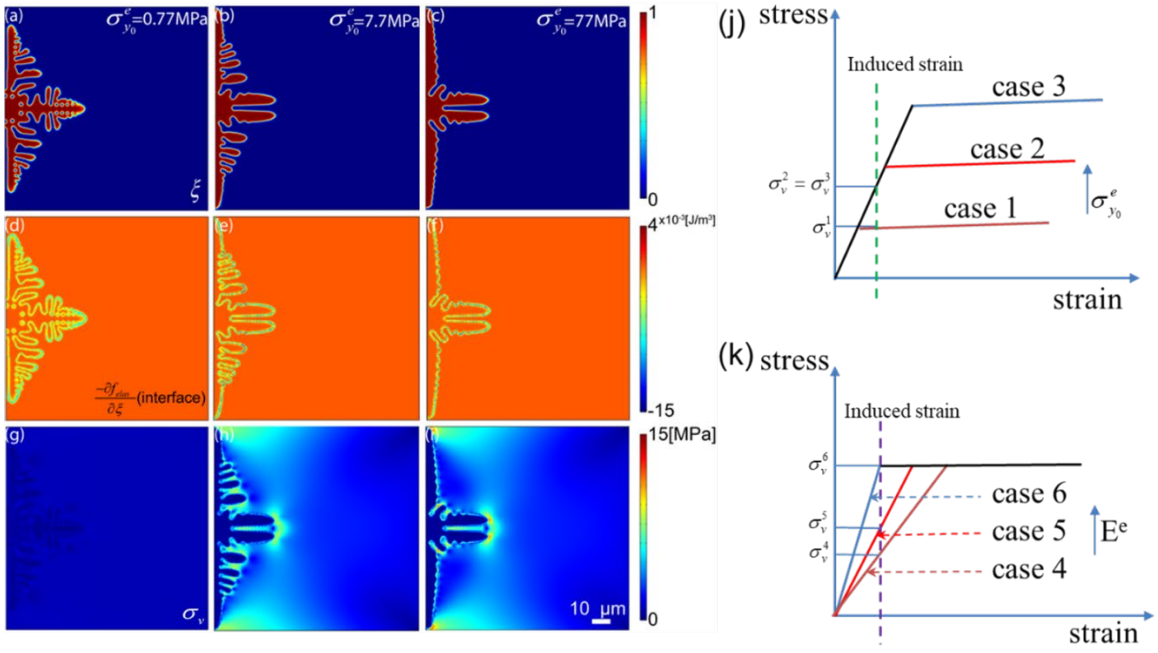

Figure 4-5 Dendrite morphology(a)-(c), elastic driving force (d)-(f) and corresponding von Mises stress distribution (g)-(i) from the phase-field modeling after 500s evolution in the polymer electrolyte of different yield strength ($\sigma_{y_0}^e$): (a) 0.77MPa; (b) 7.7MPa; (c) 77MPa. The elastic modulus of electrolyte (E^e) is fixed at 35GPa. (j)-(k) Schematic diagram of the von Mise stress change when the yield strength increases at fixed elastic modulus (j), and when the elastic modulus increases at fixed yield strength (k), based on the assumption of fixed induced strain.

4.2.3 Effect of yield strength of metal electrode on the dendrite growth

As the yield strength of Li metal may vary by several orders of magnitude (10^{-1} ~10^{1}MPa) which is dependent on the creep behavior, stretch rate and size effect[15–18], here we continue to investigate the effect of the yield strength of metal electrode ($\sigma_{y_0}^m$) on the metal dendrite growth. Figure 4-6 (a)-(c) illustrates the final morphology of the metal dendrite after 50s evolutions when $\sigma_{y_0}^m$ varies from 0.4 to 40MPa. The elastic modulus of the Li metal electrode and the solid electrolyte, and the yield strength of the electrolyte are set to be 5GPa, 35GPa, and 0.77MPa, respectively. From Figure 4-6(a)-(c), it is seen that

the Li dendrite growth is better inhibited when $\sigma_{y_0}^m$ increases, similar to the inhibition effect by the solid electrolyte (Figure 4-5(a)-(c)). However, the major difference is that here both the horizontal (along *z*) and vertical (along *x*) growth of the dendrite structure are inhibited when $\sigma_{y_0}^m$ increases, while in Figure 4-5(a)-(c) only the vertical growth of the dendrite structure is suppressed, and its lateral growth is slightly promoted when σ_{y0}^e increases. The elastic driving forces ($-\partial f_{elas} / \partial \xi$) under different $\sigma_{y_0}^m$'s are further compared in Figure 4-6(d)-(f). It is seen that their values are almost the same along the electrode-electrolyte interface for all cases. However, from the von Mises stress distribution as shown in Figure 4-6(g)-(i), the high deviatoric stress is mainly seen inside the metal electrode, which increases with increasing $\sigma_{y_0}^m$. This is significantly different from the deviatoric stress distribution and magnitude under different $\sigma_{y_0}^e$'s, in which maximum deviatoric stress are seen inside the electrolyte and along the electrode-electrolyte interface (Figure 4-5(g)-(i)). Therefore, the deviatoric stress might be responsible for the inhibition of Li dendrite growth. Our simulation results are different from previous studies by Barai *et. al.* [140] as shown in Figure 4-7. In their work, the effective suppression of the dendritic protrusion occurs when the lithium electrode undergoes plastic deformation, and the polymer electrolyte is only elastically deformed. However, based on out simulation results, the Li dendrite can be better inhibited when both lithium electrode and polymer electrolyte are in the elastic deformation region. This is because a high Li metal yield strength enables the electrode to endure higher stress induced by the mechanical suppression. It is noteworthy that here we only show one scenario of the effect of $\sigma_{y_0}^m$ on

the metal dendrite growth (E^m =5GPa, E^e =35GPa, $\sigma_{y_0}^e$ =0.77MPa). In fact, under different combinations of the E^m , E^e , and $\sigma_{y_0}^e$, the trend of the Li dendrite growth with increasing $\sigma_{y_0}^m$ may not be monotonous, which makes the overall trend more complicated as shown in Figure 4-8. Therefore, a more comprehensive analysis of the effect of yield strength of the metal electrode is needed.

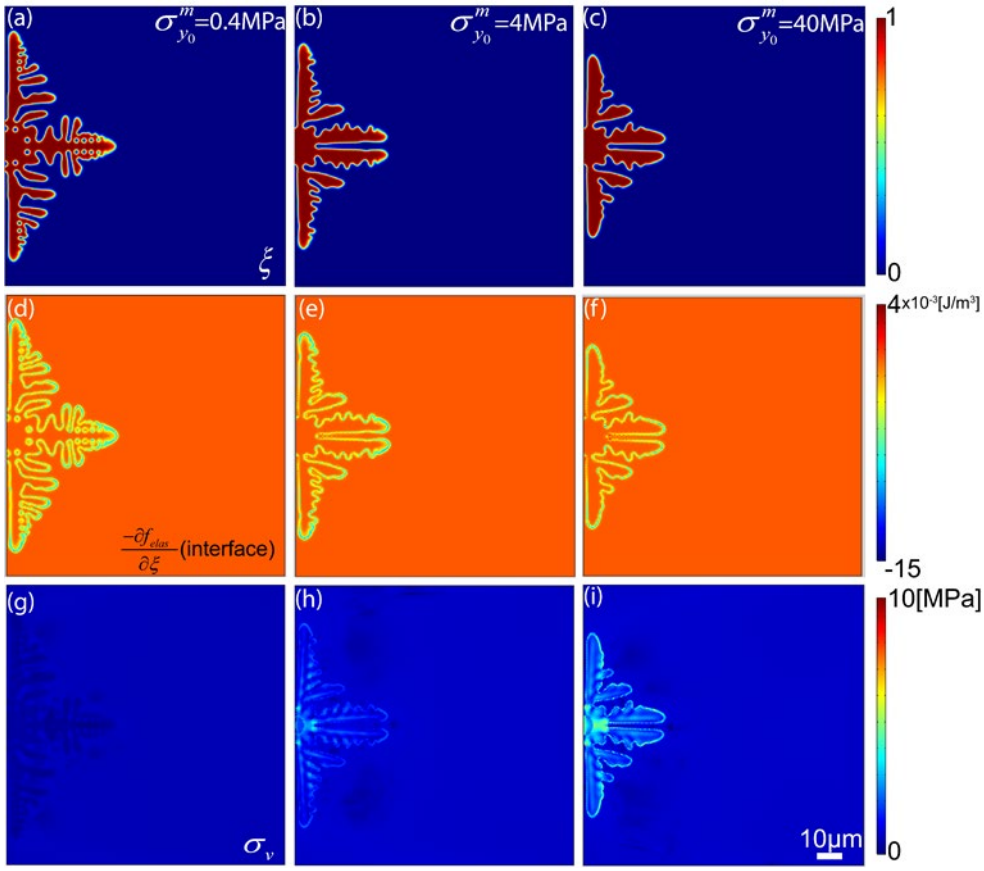

Figure 4-6 Dendrite morphology(a)-(c), the corresponding elastic driving force(d)-(f) and the von Mises stress distribution (g)-(i) from the phase-field model after 50s evolution under the Li metal of different initial yield strength. The initial yield strengths of metal are as indicated in the first row of figure which are: 0.4MPa (a)(d)(g); 4MPa (b)(e)(h) and 40MPa (c)(f)(i). The elastic modulus of the electrolyte is 35GPa.

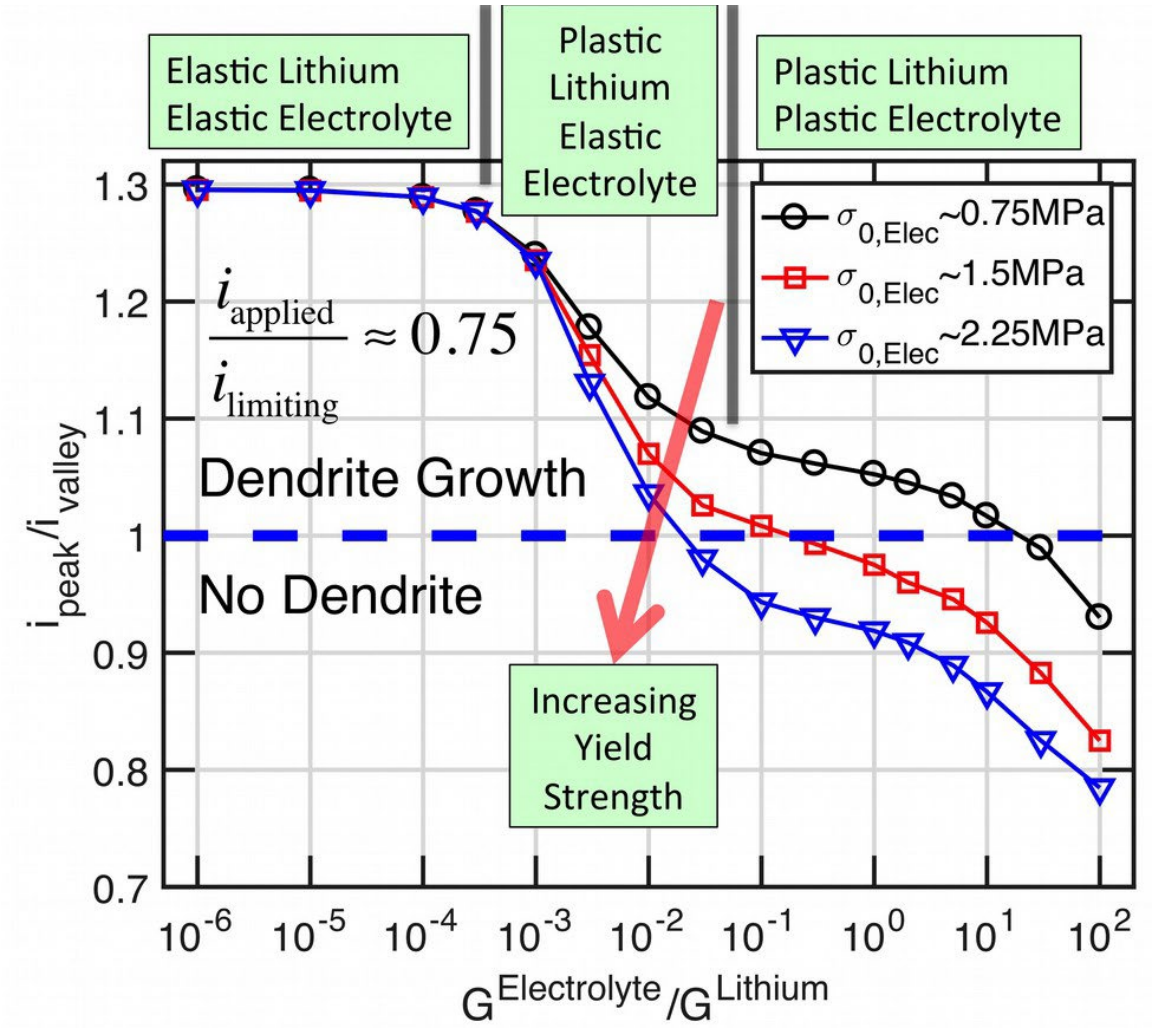

Figure 4-7 Ratio of current at the peak over that at the valley plotted with respect to the shear modulus of the electrolyte phase. Increasing yield strength of the electrolyte phase helps to stabilize the deposition of lithium. The applied current is 75% of the limiting current for that particular system. The overall curve can be divided into three different zones: a) Low electrolyte modulus, where only elastic deformation of lithium and electrolyte occurs. b) medium electrolyte modulus, where elastic deformation of the electrolyte is accompanied with plastic deformation of lithium metal. c) High shear modulus of the electrolyte, where elastic-plastic deformation of both lithium and electrolyte occurs[140].

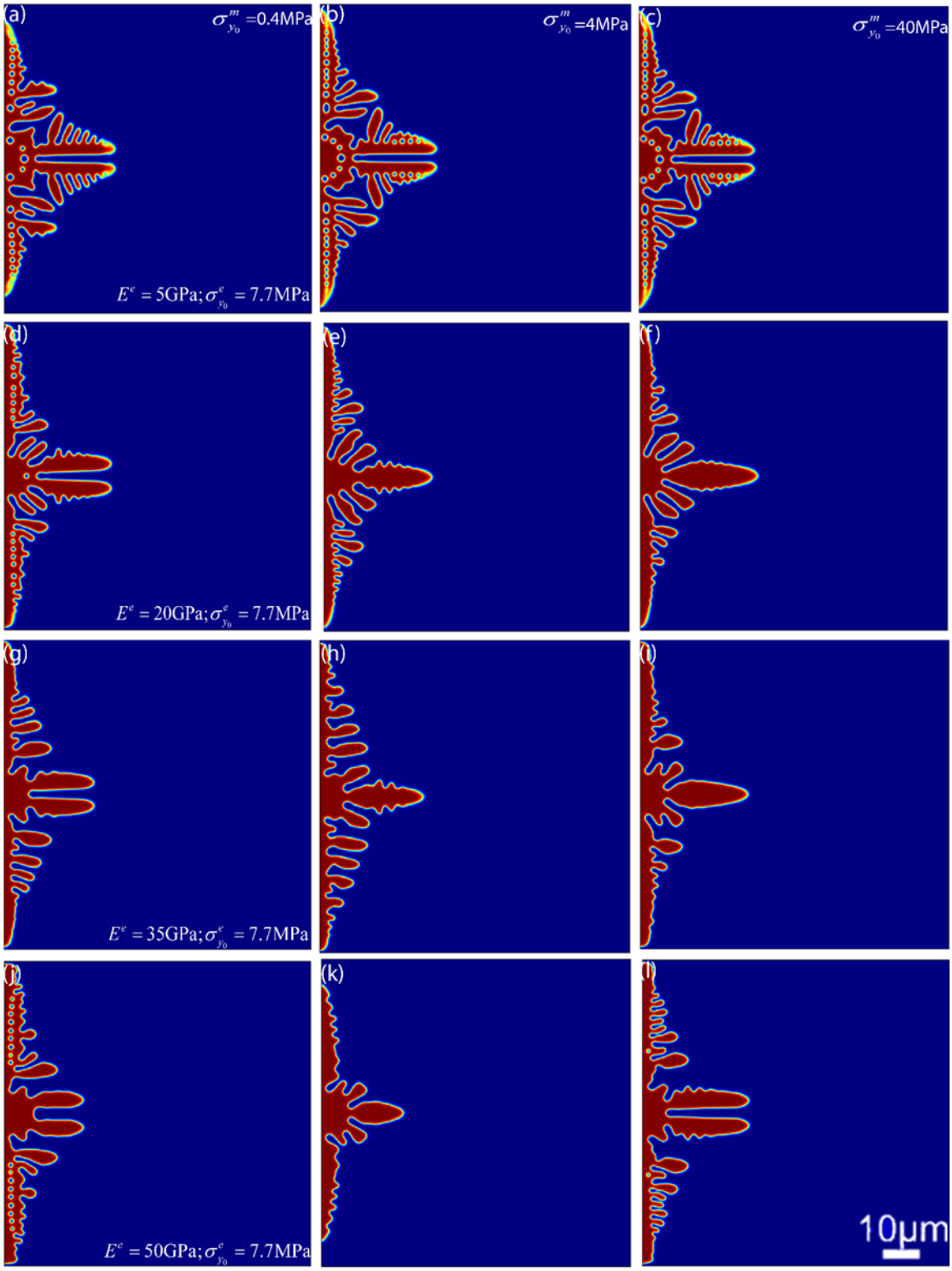

Figure 4-8 Different trends of the effect from metal's yield strength under the electrolyte with different mechanical properties.

4.3 High-throughput phase-field simulations

To investigate the overall trend of the inhibitory effect from the three mechanical properties ($\sigma_{y_0}^m$, $\sigma_{y_0}^e$ and E^e), we perform the high-throughput phase-field simulations by varying the magnitudes of the above three mechanical properties, and calculating the corresponding dendrite length (L) and the area ratio (A%). Here L measures the growth rate of the Li dendrite. It is directly obtained from the simulated dendrite morphology. A% illustrates the side growth of the dendrite, which is calculated from the dendrite area (A) divided by the product of dendrite length (L) and width (W), i.e., $A\% = A/(W \times L)$, as illustrated in Figure 2-2 (a). Thus, a low value of A% indicates the limited side growth under the similar dendrite main growth (L) along the vertical direction. The ranges of $\sigma_{y_0}^m$, $\sigma_{y_0}^e$ and E^e are chosen to be 0.4-20MPa, 1-45MPa and 0.3-50GPa, respectively, which include most of the polymer electrolytes, and cover the variation of $\sigma_{y_0}^m$ caused by the creep, stretch rate, and size effect. The high-throughput calculation results are shown in Figure 4-9 (a) and (b). From Figure 4-9 (a), it is seen that the Li dendrite lengths after 500s evolution vary from 170μm to 447μm. As a general trend, under a combination of higher $\sigma_{y_0}^e$ and higher E^e , the Li dendrite length is minimized among all-range of $\sigma_{y_0}^m$. In contrast, increasing the $\sigma_{y_0}^m$ only helps to mitigate the dendrite growth at a higher E^e but lower $\sigma_{y_0}^e$. On the other hand, the plot of area ratio (A%) (Figure 4-9(b)) indicates that the combination of higher $\sigma_{y_0}^e$ and E^e also contributes to the inhibition of the dendrite side growth, while the influence of $\sigma_{y_0}^m$ is not obvious compared to the other two parameters.

To clearly identify the trends from the 3D database, the 2D maps of the dendrite length and area ratios are plotted as a function of any two out of the three parameters. Figure 4-9(c) shows the Li dendrite length as a function of E^e and $\sigma_{y_0}^e$ at a fixed $\sigma_{y_0}^m$ of 0.4MPa. A region of low dendrite length is clearly seen at the upper-right corner of Figure 4-9(c) (a red circle), which corresponds to certain solid electrolyte of higher elastic modulus and yield strength. In contrast, at a fixed E^e = 20GPa (Figure 4-9(d)) or a fixed $\sigma_{y_0}^e$ = 2MPa(Figure 4-9(e)), the region corresponding to the lowest dendrite length in the 2D maps is scattered. The trend in the area ratio (Figure 4-9(f-h)) is also similar to the dendrite length, i.e., increasing E^e and $\sigma_{y_0}^e$ help inhibit the dendrite side growth. Based on our simulation results, the solid electrolyte with both higher E^e and $\sigma_{y_0}^e$ is most effective in the dendrite inhibition and thus could potentially increase the life cycles of the cells under similar testing conditions. This agrees with a recent report on the trend of the cycle life of various solid-electrolyte battery systems[77], in which different solid electrolytes, such as PEO [136], lithium sulfide ($Li_2S–P_2S_5–MS_x$)[197], and thin film LiPON[198] with increasing elastic moduli from 0.3GPa to 77GPa, also exhibit increasing life cycles from 400 to 10,000, which are generally considered to be due to a stable Li plating/stripping during the charge/discharge cycling. However, if only the condition of higher E^e is met, tuning the yield strength of the metal ($\sigma_{y_0}^m$) can also help reduce the dendrite growth. Our simulation results agree with previous literature that mechanically stiff solid-state electrolyte (high E^e & $\sigma_{y_0}^e$) are more effective in preventing the dendrite propagation[136]. Meanwhile, the initial yield strength of Li metal is related its creep behavior, which plays a critical role in the mechanical suppression of dendrite growth. On the one hand, when

E^e is high, the induced mechanical stack stress can suppress void formation in the metal through beneficial creep[199–202] . On the other hand, the detrimental creep will, in extreme cases, cause the lithium extrusion around the electrolyte and eventually cause short circuit[203]. The complexity in the creep behavior of Li metal may be the reason for different trends of the inhibitory effects of Li dendrite from the yield strength of metal electrodes.

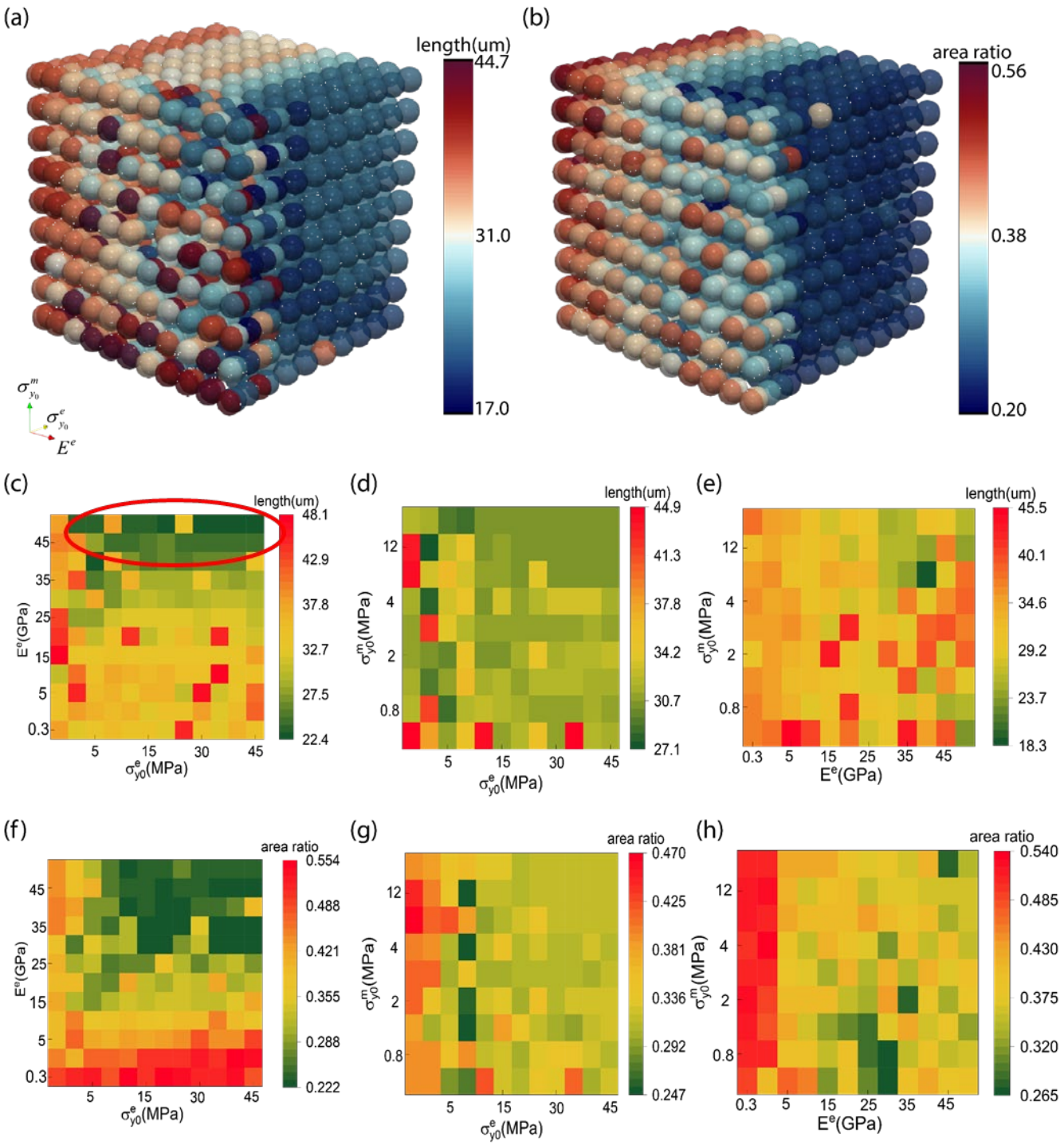

Figure 4-9 High-throughput phase-field simulation results. (a) the length and (b) the area ratio of the dendrite growth by parameterizing the three mechanical properties, i.e., the initial yield strength of metal ($\sigma_{y_0}^m$) and electrolyte ($\sigma_{y_0}^e$) and elastic modulus of electrolyte (E^e). 2D mapped dendrite length (c)-(e) and area ratio

(f)-(h) as cross sections of the 3D results by fixing one of the three properties ((c)&(f) $\sigma_{y_0}^m$ is fixed at 0.4MPa, (d)&(g) E^e at 20GPa, (e)&(h) $\sigma_{y_0}^e$ at 2MPa). The elastic modulus of lithium metal is set to be 5GPa.

4.4 Machine learning models

Based on the high-throughput calculation results, we develop a machine-learning model to explore the correlation between the mechanical properties (elastic moduli and initial yield strength) and the dendrite morphology (length and area ratio). In addition to the three parameters ($\sigma_{y_0}^m$, $\sigma_{y_0}^e$, E^e) from the high-throughput simulations, elastic modulus of the metal electrode (E^m) is also included, so that the model can also provide some guidance to other battery systems. It is noteworthy that the dendrite length and area ratio are dependent on many factors, such as the initial protuberant morphology, interfacial roughness, internal temperature in the cell, as well as the external conditions such as the magnitude and duration of the applied voltage, current density, etc[168]. Here we develop a machine learning model not to quantitatively predict the dendrite morphology, but to elucidate the relative importance of the mechanical properties of the electrode and electrolyte in the dendrite growth behavior. A recently developed Sure Independence Screening and Sparsity Operator (SISSO)[181] machine learning approach is employed to train the database and predict the dendrite length as well as area ratio. SISSO not only allow us to screen the combinations of input parameters with physical meanings to build the huge feature space using the sure independence screening (SIS) but also filter out the correlated features with sparsity operator (SO). The root mean squared error (RMSE) is used as the metrics to construct the features in descriptors. After training the datasets, we choose the

3D-descriptor as the predictive expression of relative dendrite length ($\tilde{L}$) with RMSE = 0.163 and relative area ratio ($\tilde{A}\%$) with RMSE = 0.109, as shown in Eqs.(52)(53).

$$\begin{aligned}\tilde{L} = &-1.25\times10^{-2}\times\left(\frac{\tilde{E}^e}{\sqrt{\tilde{E}^m}}+\log\tilde{\sigma}^m_{y_0}\sqrt{\tilde{E}^m}\right)\\ &+5.30\times10^{-2}\times\left\|\log\tilde{E}^e-\log\tilde{\sigma}^e_{y_0}\right|-\left|\log\tilde{E}^m-\log\tilde{\sigma}^m_{y_0}\right\|+0.97\end{aligned} \tag{52}$$

$$\begin{aligned}\tilde{A}\% = &-0.41\times(\tilde{E}^e-\tilde{\sigma}^m_{y_0})\frac{\sqrt[3]{\tilde{\sigma}^e_{y_0}}}{\tilde{E}^e+\tilde{\sigma}^e_{y_0}}\\ &+8.4\times10^{-5}\times(\tilde{E}^m-\left|\tilde{E}^e-\tilde{\sigma}^m_{y_0}\right|)(\tilde{\sigma}^e_{y_0}+\tilde{\sigma}^m_{y_0}-\left|\tilde{E}^e-\tilde{E}^m\right|)+1.296\end{aligned} \tag{53}$$

where $\tilde{E}^e$, $\tilde{E}^m$ are the reduced values of E^e, E^m, which are normalized by 1GPa, while $\tilde{\sigma}^e_{y_0}$, $\tilde{\sigma}^m_{y_0}$ represent the reduced values of $\sigma^e_{y_0}$, $\sigma^m_{y_0}$, which are normalized by 1MPa, $\tilde{L}$ and $\tilde{A}\%$ are obtained via dividing L and $A\%$ by L_0 and $A_0\%$, the latter of which are calculated from the phase-field simulation using PEO solid electrolyte and Li metal electrode.

When the elastic modulus of the metal is fixed (E^m =5GPa), the first term on the right-hand side of Eq.(52) indicates that when E^e or $\sigma^m_{y_0}$ increases, the dendrite length will decrease (due to a negative coefficient of -0.00125), and E^e plays a more critical role than $\sigma^m_{y_0}$ since $\sigma^m_{y_0}$ is in the logarithm. The second term in Eq.(52) reveals that electrolyte with a higher $\sigma^e_{y_0}$ (combined with a higher E^e, as $\log E^e$ needs to be greater than $\log\sigma^e_{y_0}$) can also inhibit the dendrite. When $\sigma^e_{y_0}$ is much smaller than 1MPa, it will promote the dendrite growth. The second term also explains that when $\sigma^e_{y_0}$ is small, increasing $\sigma^m_{y_0}$ (such that $\log\sigma^m_{y_0}$ becomes greater than $\log E^m$) will also result in a smaller dendrite length

L. From Eq.(53), the area ratio (*A*%) is highly dependent on E^e. With a relatively higher E^e, the decrease of $\sigma_{y_0}^e$ and $\sigma_{y_0}^m$ tend to further reduce *A*%. The second term in Eq.(53) has limited effect on *A*% due to its much smaller coefficient (8.4×10^{-5}) compared to the first term in Eq.(53).

The dependence of dendrite morphology on the elastic modulus of the metal electrode (E^m) is complicated. From the first term in Eq.(52), with a lower $\sigma_{y_0}^m$ (e.g., smaller than 1MPa), the increase of E^m will increase the dendrite length. However, this reduction may be offset if the initial yield strength of the metal ($\sigma_{y_0}^m$) is high so that log $\tilde{\sigma}_{y_0}^m$ becomes positive. From Eq.(52), the side growth (area ratio) has less correlation with E^m, as E^m is only included in the second term of Eq.(53) with a much smaller coefficient (8.4×10^{-5}). It is noteworthy that the current model assumes the same Li metal electrochemical reaction kinetics while tuning the elastic modulus of the metal electrode. Therefore the results obtained from this machine learning model can only qualitatively predict the trend of dendrite growth for other metal electrode battery systems.

Finally, we compare the values of the dendrite length and area ratio in the test datasets (not used for training the machine learning model), which are predicted from the machine learning (ML) model and calculated from the phase-field modeling (PFM). These results are plotted in Figure 4-10(a), (c). It is seen that these datasets are clustered near a straight line, where the phase-field-calculated and machine-learning-predicted values are equal to each other. This indicates the machine learning model merits a good prediction to the dendrite morphology. The percentage of the prediction errors are plotted in Figure 4-10(b) and (d), which reveal that most prediction errors are in the range of $\pm$ 20%.

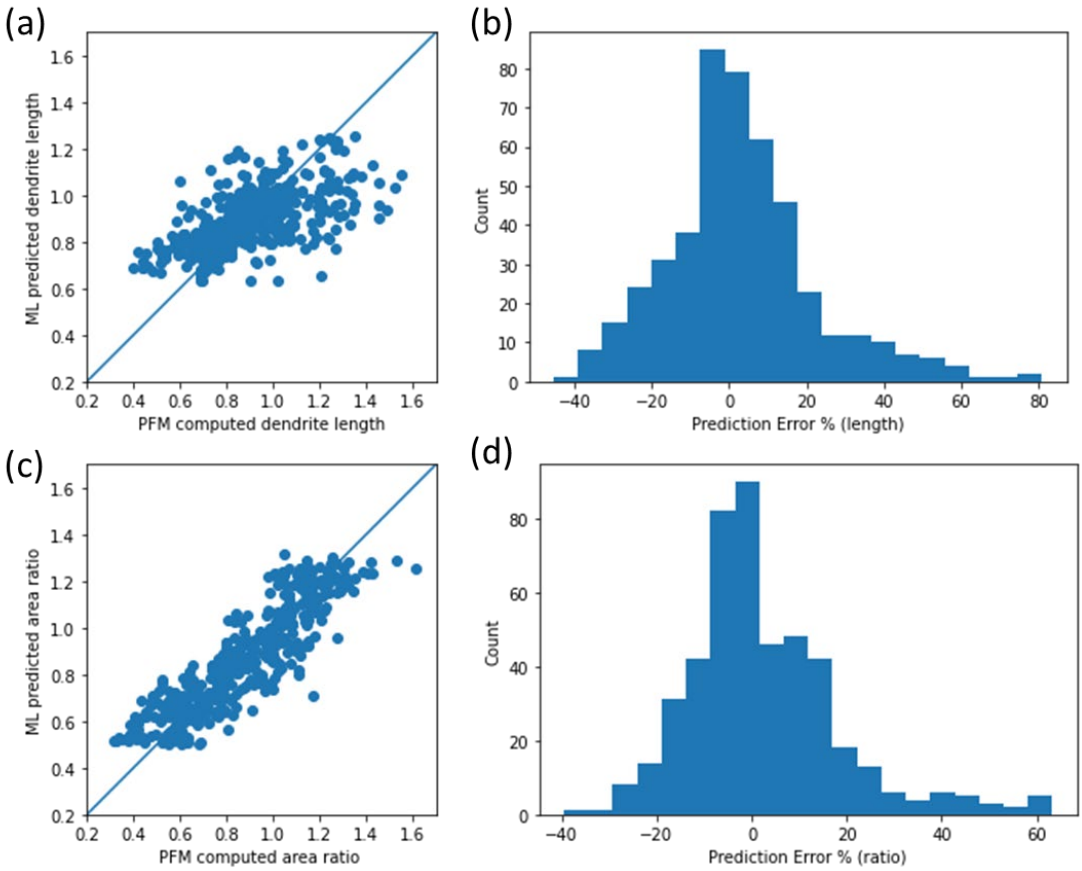

Figure 4-10 Comparisons of predicted values from SISSO model and true values from phase-field simulation for (a) dendrite length and (c) area ratio. Corresponding percentages of prediction error for (b) dendrite length and (d) area ratio.

The DNN model results are as shown in Figure 4-11. It shows that both prediction errors are also in the range of ± 15% which is slightly better than SISSO results. The prediction accuracies between DNN model and SISSO model are not very different. From the coefficient of determination, R^2, for dendrite length, R^2 equals 0.57 and 0.38 as of DNN model and SISSO model, while for area ratio, R^2 equals 0.84 and 0.80 as of DNN model and SISSO model, respectively, which are acceptable. However, the DNN model cannot output analytical equations, such as Eqs.(52)(53) from the SISSO model. With acceptable

sacrifice of prediction accuracy, SISSO model is able to generate the direct connections between mechanical properties and dendrite growth which is easy to analyze.

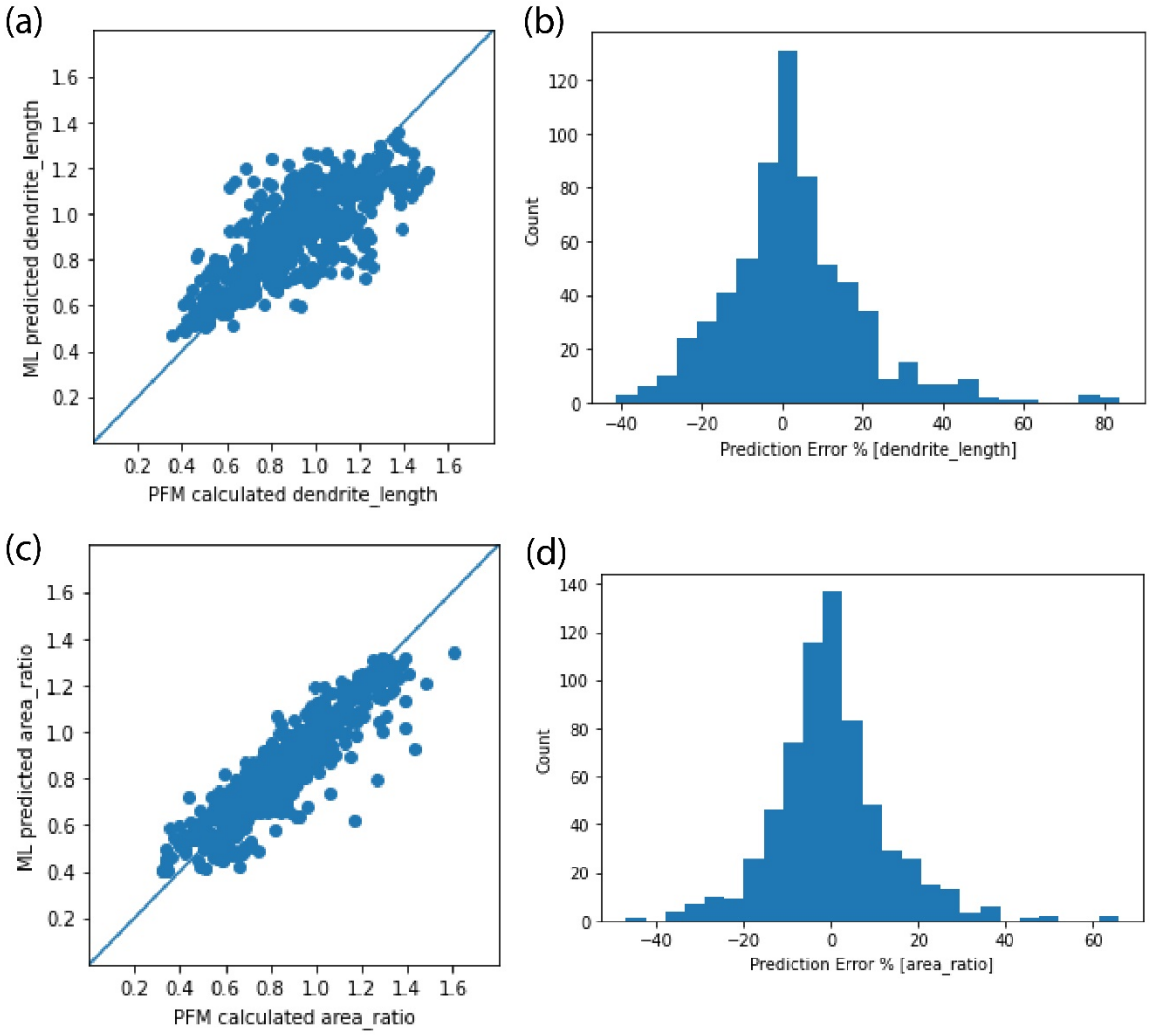

Figure 4-11 Comparisons of predicted values from DNN model and true values from phase-field simulation for (a) dendrite length and (c) area ratio. Corresponding percentages of prediction error for (b) dendrite length and (d) area ratio.

Chapter 5. Dendrite inhibition by nanofillers

5.1 Li dendrite growth in solid composite electrolyte embedded with nanofibers

We continue to study the effect of Al_2O_3 nanofiber embedded in the PVDF-HFP polymer electrolyte on the Li dendrite growth, as the modulus of Al_2O_3 is much higher than both the Li metal and the matrix electrolyte. A smaller system size is used, as 9×9μm together with t_0=0.5s. The temperature of entire system is set to be 300K. Several assumptions are made for the simulations. First, all the nanofibers are assumed to be parallel to each other, and uniformly distributed in the polymer electrolyte. It has recently been reported that such an alignment could enhance the Li^+ conductivity[204]. Second, the nanofibers do not contact with the metal electrode, i.e., there is a narrow spacing between the anode and front of the nanofibers, which allows the nucleus to initially grow freely near the electrode/electrode interface before reaching the front of the nanofibers. Third, only purely elastic effect is considered in this system. For simplicity, we fixed the positions of the nanofibers in the polymer matrix, i.e., ϕ is not evolving. The elastic moduli of the Al_2O_3 nanofiber and the polymer electrolyte are set to be 300GPa and 4.9GPa, and the diffusion coefficient and initial concentration of Li^+ in the nanofibers are 2.5×10^{-15} m^2/s and 0.0 mol/L, respectively. Figure 5-1 illustrates the morphology of the Li dendrite with different diameters and volume fractions of the oxide nanofiber. It is seen that Li deposits are confined in the electrolyte between the adjacent nanofibers, due to much larger elastic modulus of the nanofibers. These nanofiber arrays lead to Li^+ transport along horizontal direction rather than other random directions, as compared to Figure 4-1 (a)~(c). As a result, the Li deposits are isolated and could not accumulate into large dendrite. It is believed that inhomogeneous Li stripping/platting is the major reason for Li dendrite growth in solid

electrolytes[36,205,206]. Therefore, the introduction of Al_2O_3 nanofiber of higher elastic modulus could effectively suppress the dendrite growth.

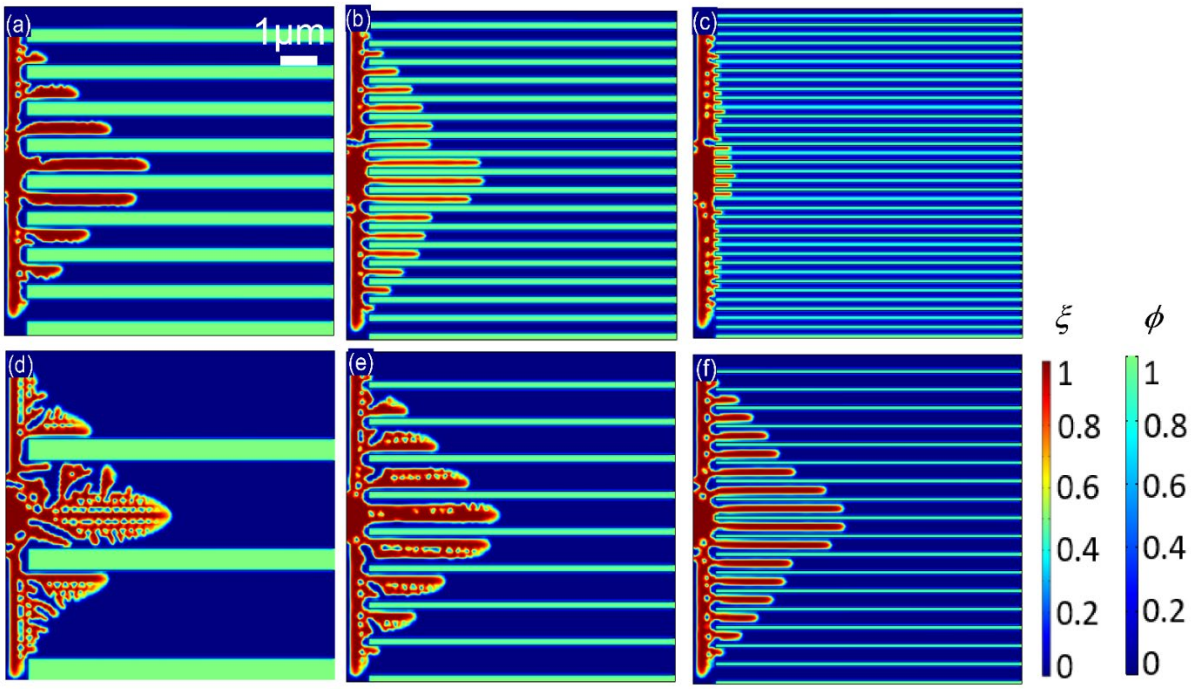

Figure 5-1 Simulation results of Li dendrite morphology in polymer electrolyte embedded with well aligned nanofiber of different sizes (d) and volume fractions (V_f). (a): d = 0.4μm, V_f = 40%; (b): d = 0.2μm, V_f = 40%; (c): d = 0.1μm, V_f = 40%; (d): d = 0.6μm, V_f = 20%; (e): d = 0.2μm, V_f = 20%; (f): d = 0.1μm, V_f = 20%.

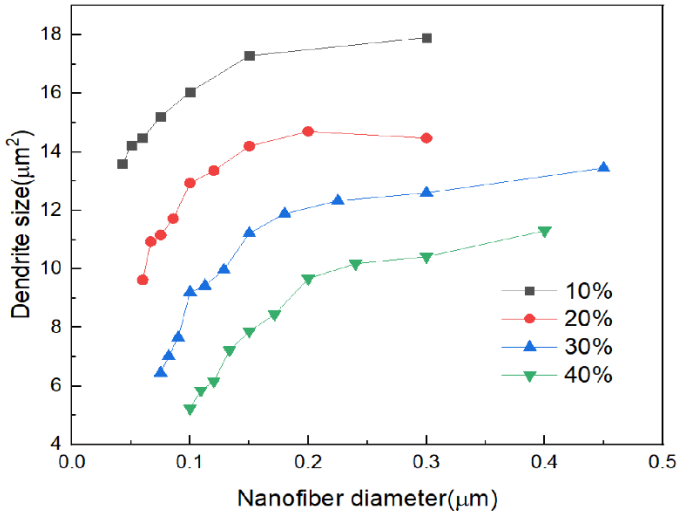

Figure 5-2 Li dendrite size in Al_2O_3 nanofiber embedded polymer electrolyte of different volume fractions (10% ~ 40%) and diameters (0.05 ~ 0.5 μm) of the Al_2O_3 nanofiber.

The dependences of the dendrite size on the nanofiber volume fractions (V_f = 10% ~ 40%) and diameters (d = 0.05 ~ 0.5μm) are illustrated in Figure 5-2. It is seen that the dendrite size decreases with increasing nanofiber density, the latter of which can be controlled by either increasing V_f or decreasing d such that there exist more nanofibers in the system. This implies that the size of the electrolyte channel between adjacent nanofibers could be a key factor for dendrite growth. To validate this, we generate a single channel of electrolyte, aside with two nanofibers, while the Li dendrite is only allowed to grow in this narrow channel (Figure 5-3(a)). We set E^e to be 4.9GPa, and will revisit it later. When the channel width (w) decreases, the width of the dendrite structure (m) decreases accordingly, as dendrites are prohibited in the nanofiber region. Meanwhile the length (l) of the dendrite structure remains almost constant initially, and significantly decrease when w reaches ~ 0.1 μm (Figure 5-3 (a) ~ (c)). To understand this effect, we compared the evolutions of the Li^+ concentration (c_{Li^+}) along the horizontal directions (z) with different nano-channel widths (w), as shown in Figure 5-3 (d) ~ (f). When w = 6.0μm, c_{Li^+} is equal to its bulk limit (1.0 mol/L) in the electrolyte, and reduces to 0.0 mol/L in the Li metal (Figure 5-3(d)). The location where c_{Li^+} decreases captures dendrite/electrolyte interface, which moves along z with evolving time. The large c_{Li^+} concentration gradient indicates slow motion of Li^+, causing Li dendrite to grow further toward the bulk electrolyte where Li ions are sufficient. When w = 0.5μm, the c_{Li^+} in the electrolyte decreases to 0.9 mol/L (Figure 5-3(e)). This slightly reduces the Li^+ concentration gradient at the Li/electrolyte interface, as well as the length of the Li dendrite (Figure 5-3(b)). When w = 0.1μm, c_{Li^+} in the electrolyte continue to decrease with evolving time, while c_{Li^+} increase to 0.1mol/L at the Li metal surface. This

results in a reduced Li^+ concentration gradient across the Li metal/electrolyte interface, implying a fast Li^+ transport in the system. This is probably because the narrower channel blocks the Li^+ transport in the vertical directions, i.e, Li^+ can only move along horizontal (z) direction. The fast Li^+ transport thus reduces the Li^+ concentration gradient at the interface, and inhibits the Li dendrite growth. It has been recently reported that smoothen the Li^+ concentration gradients near the electrode surface could mitigate the Li dendrite growth[194,207]. Our simulation results indicate that the Li^+ transport in the solid electrolyte governs in the Li dendrite growth, which agrees with literature[208]. It is reported that the metal deposits morphology is controlled by the confined channels as demonstrated in Figure 5-4.

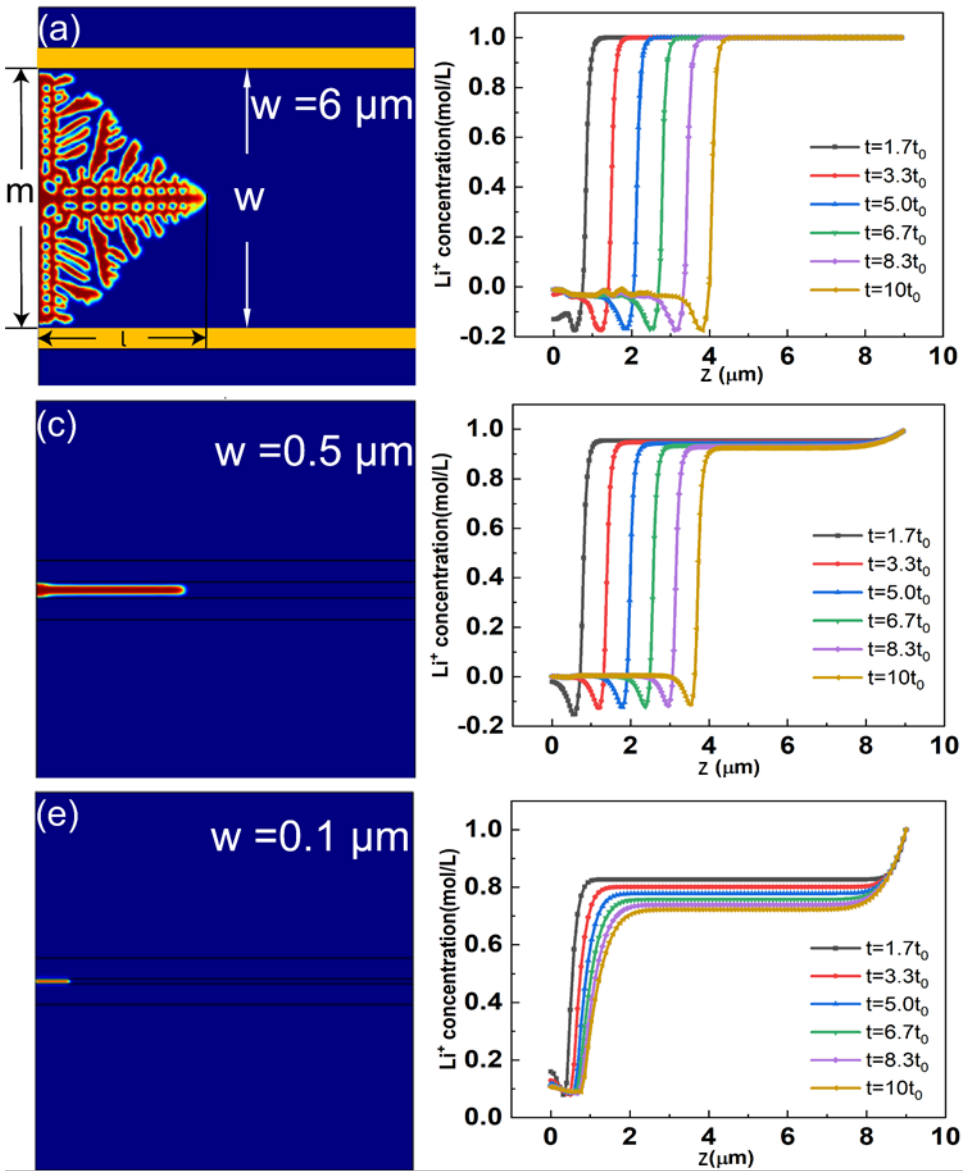

Figure 5-3 Li dendrite morphology (a)~(c) after 10s evolution, and the 1D evolution of the Li^+ concentration along z direction (d) ~ (f) in the nanochannels confined by two parallel Al_2O_3 nanofibers electrolyte of different channel widths: (a, d) 6μm (b, e) 0.5μm and (c, f) 0.1μm. Here t_0 equals 0.5s

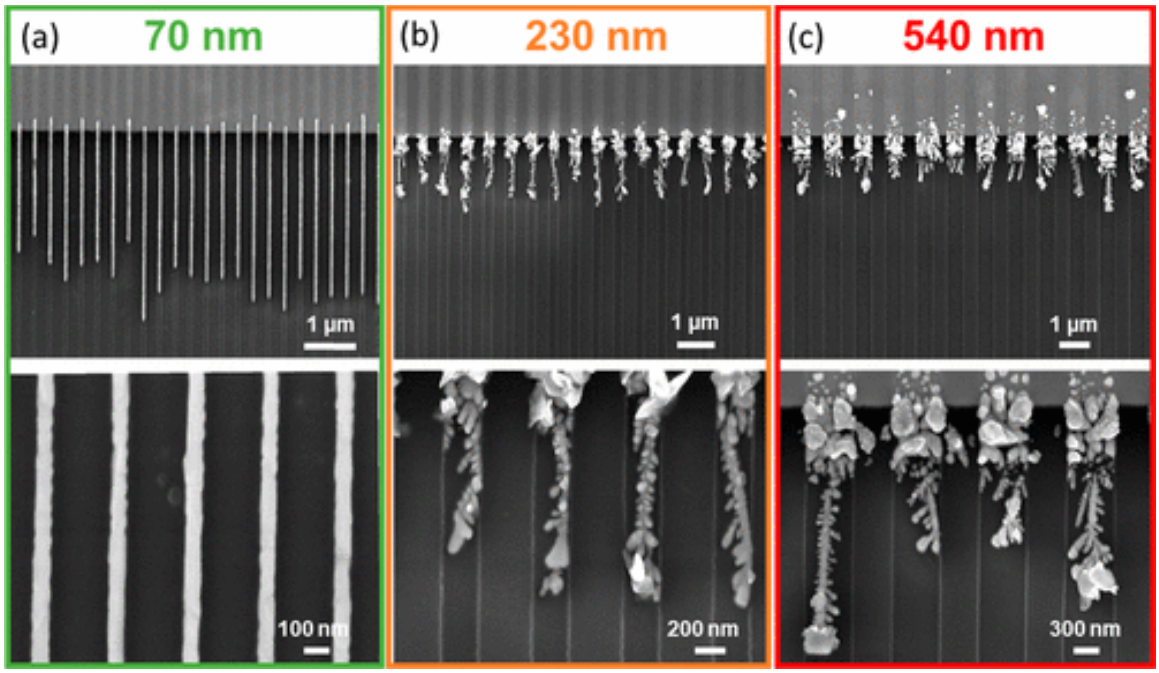

Figure 5-4 SEM images of silver morphology as deposited between Pt and Ag electrodes and confined PEO-$AgClO_4$ channels, after a galvanostatic step with current density of −0.2 mA/cm^2.[208]

5.2 Combined effects of nanochannel size and elastic modulus of the electrolyte on the Li dendrite growth

In previous section, we assumed the elastic modulus of the electrolyte (E^e) is 4.9GPa. Here we further discuss the combined effect of the elastic modulus and the nano-channel size of the electrolyte on the Li dendrite growth. We chose three different elastic moduli (1.0, 5.0 and 16GPa) representing three types of solid electrolyte of different hardness, as well as three typical channel sizes of the electrolyte (0.2, 0.5 and 1.0 μm). This results in a total of 9 combinations, as shown in Figure 5-5. The modulus of the Li metal and the Al_2O_3 nanofiber are chosen to be the same as those in previous simulations. By comparing along the three columns, it is clearly seen that at given channel size, higher

elastic modulus yields a slower dendrite growth, which agrees with our previous results in Section 5.1. On the other hand, by comparing along the three rows, it is also found that at given elastic modulus of the electrolyte, larger channel size results in a faster dendrite growth. The variation of the dendrite length at E^e = 5GPa (Figure 5-5 (d) ~ (f)) seems to be more obvious. This is better visualized by the dependence of the dendrite length on the channel size for different E^e's (Figure 5-5 (j)), in which l changes from 2.0 to 3.5 μm at E^e =5GPa (red line). This is because for E^e =16GPa, the mechanical inhibit effect is strong enough that the channel width effect is less appreciable (blue line). When E^e =1.0 GPa (soft electrolyte, black line), the effect of the channel width becomes smaller since Li dendrite can grow fast enough. The variation of the dendrite length (Δl) with decreasing channel width as a function of electrolyte elastic modulus (Figure 5-5 (k)) shows that the maximum Δl appears at E^e = 5GPa.

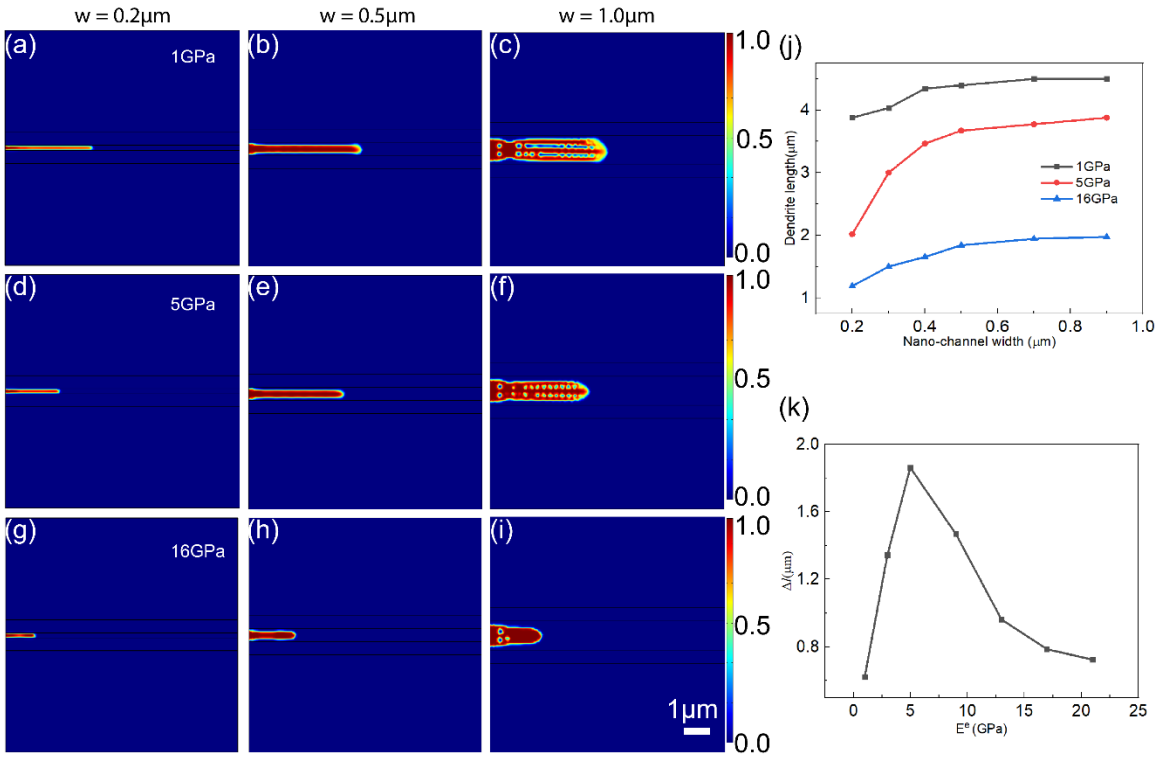

Figure 5-5 Dependence of dendrite growth within channels of different widths (0.2, 0.5 and 1.0 μm) for electrolyte of different magnitude of elastic modulus: (a) ~ (c) E^e = 1GPa, (d) ~ (f) E^e = 5GPa, (g) ~ (i) E^e = 16GPa; (j) Variation of Li dendrite length after 5s growth with different electrolyte channel widths and elastic modulus; (k) Dendrite length change when the channel decreases from 1.0μm to 0.2μm for different E^e 's.

5.3 Effective Li ion conductivity in solid composite electrolyte

The addition of nanofiller in the polymer electrolyte can not only inhibit the dendrite growth but can also modify the Li^+ conductivity compared to pure polymer electrolyte. This is due to the formation of an amorphous layer surrounding the nanofillers, which lowers the degree of crystallization of the polymer film[209]. The overall effective conductivity of the system can thus be calculated from the volume fraction of the nanofiller additives, the amorphous interface layer, and the polymer matrix, and their relative ionic conductivities. To do that, we further developed a numerical model to simulate the local distribution of the ionic current densities (J) and calculate the effective Li^+ conductivity in

Al_2O_3 embedded P(VDF-HFP) nanocomposite electrolyte. The relative ionic conductivities of the polymer matrix (σ^M), the conductive amorphous shell (σ^s), and the insulating nanofiller (σ^f) are chosen to be 3.98×10^{-4} S/cm, 5.63×10^{-3} S/cm, and 10^{-8} S/cm based on literature[210]. To obtain the local current density distribution, a voltage of 1.0V is applied to the bottom electrode while the top electrode is grounded. Figure 5-6(a) shows three distinct regions of local ionic current densities. The overall effective Li^+ conductivities is then calculated as $\sigma_{eff} = J_{total} / E$, where $J_{total} = \sum_i J_i$ is the total current density and E is the applied electric field. From Figure 5-6(b), σ_{eff} initially increases with V_f, due to the increasing amount of the highly conductive shell, and then decreases with V_f, due to nanofiber with lowest conductivity occupying the majority of the system. The turning point indicates that the electrolyte is saturated by the conductive shell and no polymer phase remains. Based on our simulation, the maximum effective conductivity is ~ 3.0×10^{-3} S/cm with 40% Al_2O_3 nanofiber. For comparison, we also calculated σ_{eff} using the McLachlan's Generalized Effective Medium Theory (GEMT)[164–166]. Both the numerical simulations (black line) and the analytical calculations (red line) yield similar trends for the effective conductivity on V_f. The maximum σ_{eff} and the corresponding V_f agree in both methods. There is a discontinuity of the analytical curve at $V_f = 0.4$, and a moderate deviation between the two curves when $V_f > 0.4$. This is because two different equations are used for $V_f < 0.4$ and $V_f > 0.4$ in the analytical calculations (see Section 2.4 for details). Finally, we synthesized the alumina nanofiber embedded P(VDF-HFP) solid composite electrolyte, measured its Li ion conductivity and compared with that of bare P(VDF-HFP) electrolyte at a variety of temperatures. The results are shown in Figure 5-7.

Clearly the Li ion conductivity is enhanced by several times after introducing the Al_2O_3 nanofiber at all temperatures. Our results imply that the volume fraction of the nanofiber embedded in the solid composite electrolyte should be well controlled to inhibit the Li dendrite growth, without sacrificing the overall effective Li^+ conductivity of the composite electrolyte.

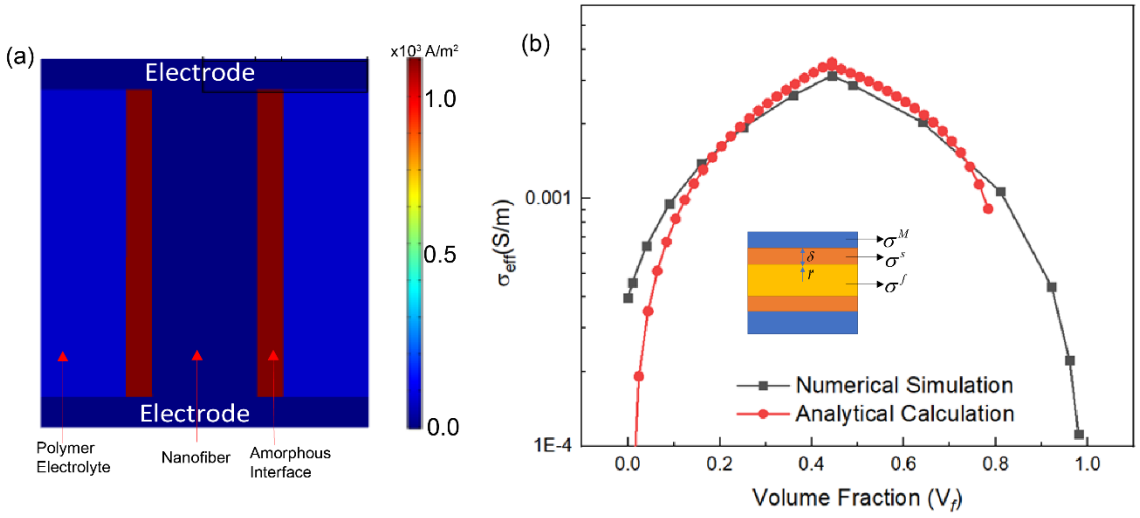

Figure 5-6 (a) Numerical simulation of the local distribution of the ionic current density (b) Comparison of the effective conductivity obtained from numerical simulation and GEMT analytical calculation (inset: 2D schematic diagram of a 3D nanofiber system consisting of the nanofiller, amorphous layer, and the polymer matrix)

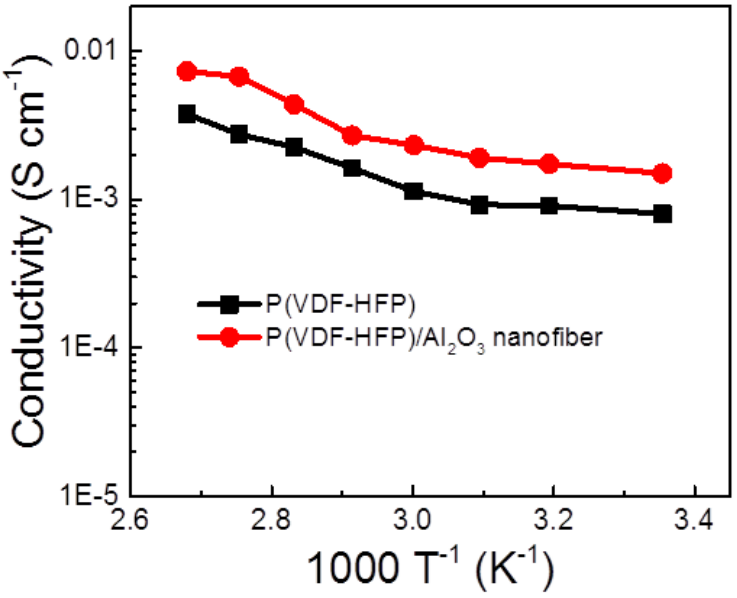

Figure 5-7 Measured ionic conductivity of pure P(VDF-HFP) electrolyte and P(VDF-HFP)/ Al2O3 nanofiber nanocomposite electrolyte.

Chapter 6. Simulations of dead Li formation

6.1 Formation of the dead Li during the discharge process

During the charging process, Li ions are reduced to Li atoms under a negative bias and deposited onto the Li metal anode. Inhomogeneous Li ion deposition form Li dendrite structure. During the discharging process, these Li atoms will be oxidized into Li ions under a positive bias, and stripped away from the Li metal. A critical problem during the discharging process is the formation of deal Li, in which Li dendrite is disconnected from the Li metal, and is no longer able to participate in the subsequent charge/discharge process in the absence of electrons provided from the Li anode. This causes significant reduction of batter capacity due to loss of active materials. Therefore, understanding the mechanism of dead Li formation is key to the stability and performance of Li metal batteries. In this chapter, we systematically explore the underlying mechanism of dead Li formation, and how it is dependent on the initial Li dendrite morphology and the external conditions (such as discharge current, voltages and temperature).

To study the formation of dead Li, a dendritic Li metal morphology is first generated. Here we start with a planar electrode with some random noise to mimic the surface roughness, as shown in Figure 6-1(a), and simulate the Li ion deposition under a negative overpotential. It is seen that initially the Li ions deposit homogeneously onto the planar electrode, until some small protrudes are formed on the flat surface (Figure 6-1(b)&(c)), and finally grow into dendritic morphology (Figure 6-1(d)). Here we separate the entire Li metal electrode into two parts: the dense Li part and the dendritic part. Figure 6-1(i) clearly shows that at the beginning, the Li ions are entirely reduced to the dense Li metal, and its amount increases quickly with time (blue curve in Figure 6-1(i)). After ~500s,

the Li dendrite appears and its amount increases rapidly (red curve in Figure 6-1(i)). Finally, almost all the Li ions are reduced and form Li dendrite.

Next, we choose the Li dendrite structure after 2000s as the initial structure as shown in Figure 6-1(e), and apply a positive voltage of 0.15V at the anode to study the Li stripping process. During this process, the dendritic part of Li metal is not completely converted into Li ions and several pieces of dead Li form, which are shown as the green parts in Figure 6-1(f) and (g). Combining the morphology evolution in Figure 6-1(e)-(h) and the Li amount consumption curve in Figure 6-1(j), it is clearly seen that in the initial stage, the dendritic Li is consumed at a high rate due to the relatively large contact area with the surrounding electrolyte, which leads to a large slope in the curve. At ~200s, some parts of the Li dendrite are disconnected from the planar electrode and form dead Li (Figure 6-1(f)&(g)). When the dendritic Li is fully consumed or becomes the dead Li, the dense Li acts as main role of discharging and the consumption rate decreases. Figure 6-2 also shows the corresponding Li ion concentration and the potential distribution during the discharge process. It is seen that in the initial stage of discharging as shown in Figure 6-2(a), all the Li metals are active Li, the Li ions are generated at the tip of dendritic structure due to the large potential drop, which causes the relatively high Li ion concentration near the tip (Figure 6-2(d)). The potential inside the Li metal remains at around 0.15V. After the first piece of dead Li is formed (Figure 6-2(b)), the potential inside the dead Li reduces to around 0.11V, which is close to the electric potential in the electrolyte surrounding the dead Li (Figure 6-2(h)). As a result, local Li ion concentration near the dead Li is reduced (Figure 6-2(e)), indicating that dead Li can no longer be oxidized into Li ion. Similar phenomenon can also be observed after the new dead Li is formed (Figure 6-2(c)).

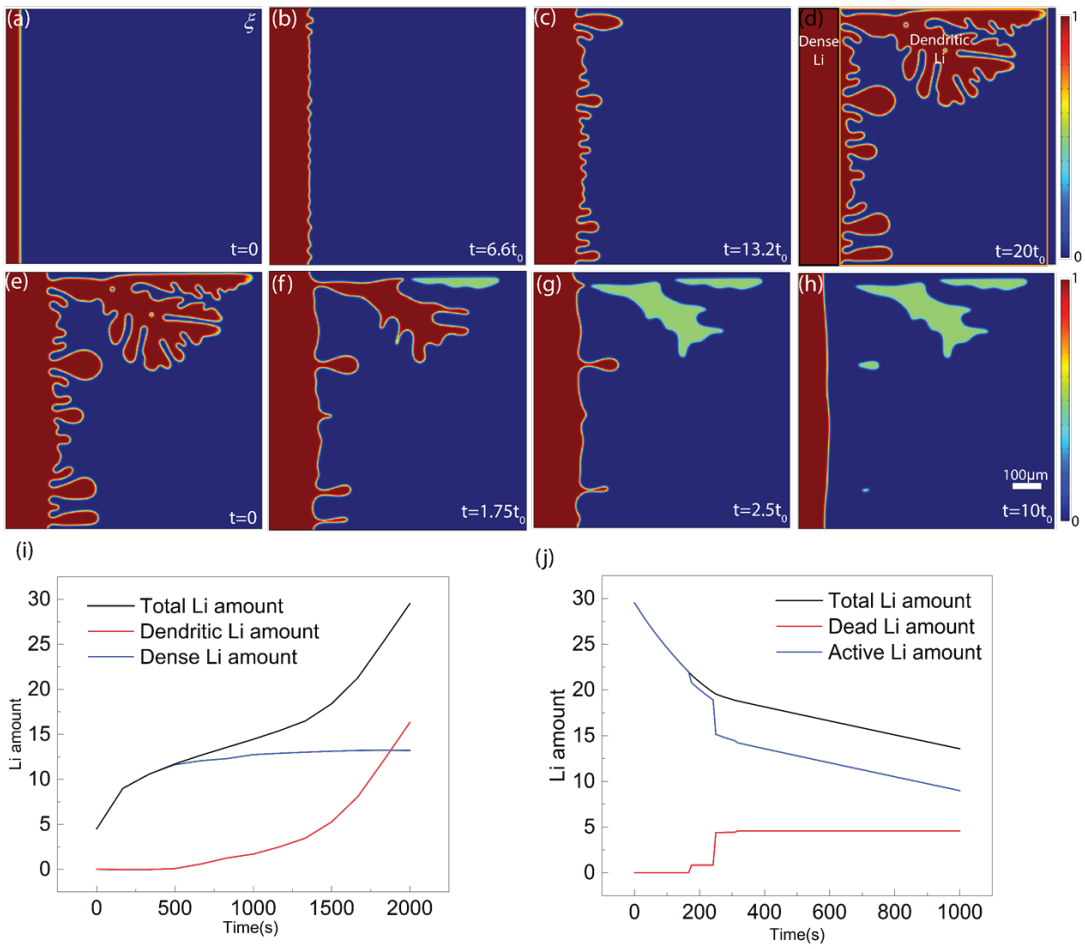

Figure 6-1 Phase-field simulation results of (a)-(c) dendrite growth on a planar electrode and (e)-(h) the discharge process with showing the dead Li formation (green area). (i) the growth curves of total Li , dendritic Li and dense Li amounts in which the dense Li and dendritic Li are as separated in (d). (j) the consumption curves of total Li, dead Li and active Li amounts. Here t_0 equals 100s.

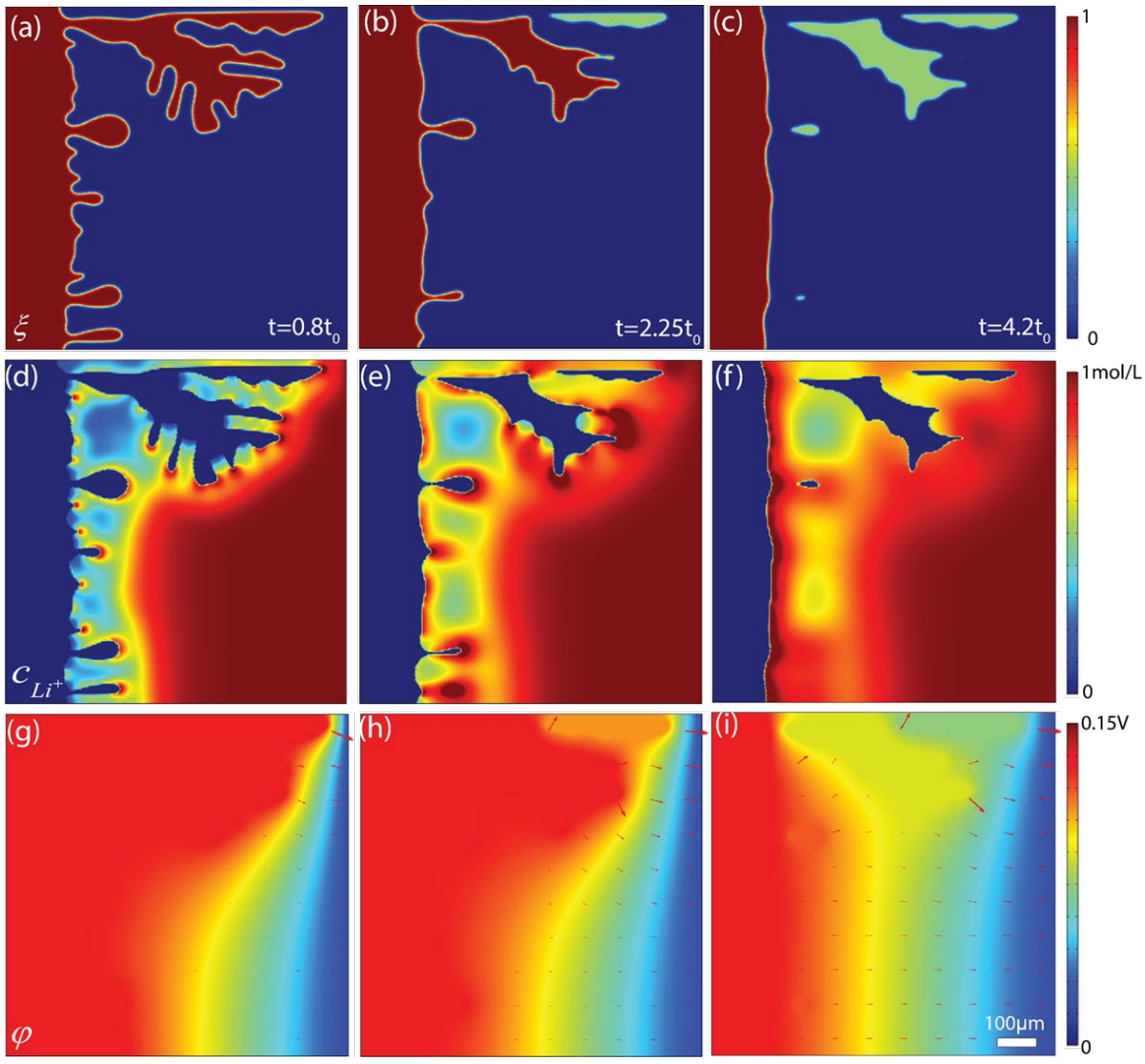

Figure 6-2 Phase-field simulation results of (a)-(c) the discharge process with showing the dead Li formation (green area) (d)-(f) corresponding Li ion concentrations (g)-(i) corresponding potential distribution(red arrows indicate the relative value and direction of the electric field). (a)(d)(g) t=83s, (b)(e)(h) t=225s, (c)(f)(i)=420s. Here t_0 equals 100s

6.2 Effects of the initial Li amount and discharge voltage on dead Li formation

Here we continue to study the effects of the initial Li amount (ILA) and the discharge voltages on the dead Li formation. ILA is related to the state of charge (SOC). By using the Li dendrite structure at different stages during the charging process as the initial structure for the discharging simulation, it is easy to control the initial Li amount.

Lower part in Figure 6-3(a) shows the dependence of capacity loss on the discharge voltages with different initial Li amounts. The capacity loss is calculated from the dead Li amount divided by the initial Li amount. It is clearly seen that the initial Li amount affects the capacity loss significantly. For the high initial Li amount of 29.5 (in reduce unit), the capacity loss can reach up to 20% which is unacceptable. With the decrease of initial Li amount, the capacity loss also decreases and becomes close to 0 when the initial Li amount reduces to 16. Figure 6-3(b) (upper part) clearly shows that the dead Li amount is almost linearly proportional to the dendritic Li amount for different discharge voltages, which means that the initial amount of Li dendrites is the main reason of dead Li formation. The conversion rate of Li dendrite into dead Li also increases with the initial dendritic Li amount, and eventually reaches ~30% when the initial Li dendrites are at a considerable amount (>16). This agrees with previous experimental reports[211] that a high SOC cycle (corresponding to a large initial Li amount in our simulation) will lead to a large capacity loss.

Another factor that will affect the dead Li formation is the discharge voltage. Here we modify the discharge voltages from 0.16V-0.25V under different initial Li amounts. From Figure 6-3(a) (lower part), it is seen that the effect of discharge voltage is not as obvious as the initial Li amount. To better demonstrate its effect, Figure 6-3(a) upper one shows the relative dead Li amount by using the dead Li amount divided by maximum value of the dead Li amount under the specific initial Li amount. It is revealed that decreasing the discharge voltage can also lead to the decrease of dead Li amount. The effect of decreasing the discharge voltage also depends on the different initial Li amount, e.g. for high initial Li amount, decreasing the voltage from 0.2V to 0.16V can lead to about 20%

decrease of dead Li while for the low initial Li amount, it can eliminate the dead Li. Therefore, the effect of discharge voltage is more significant under a low initial Li amount. Figure 6-3(b) also shows a low dead Li amount and low conversion rate at the lower discharge voltage. In this case, to avoid the formation of dead Li, a low discharge voltage should be kept during discharging. However, the discharge voltage is related to the output power of the battery which is also critical. So, the output power and the formation of dead Li should be balanced by utilizing a proper discharge voltage.

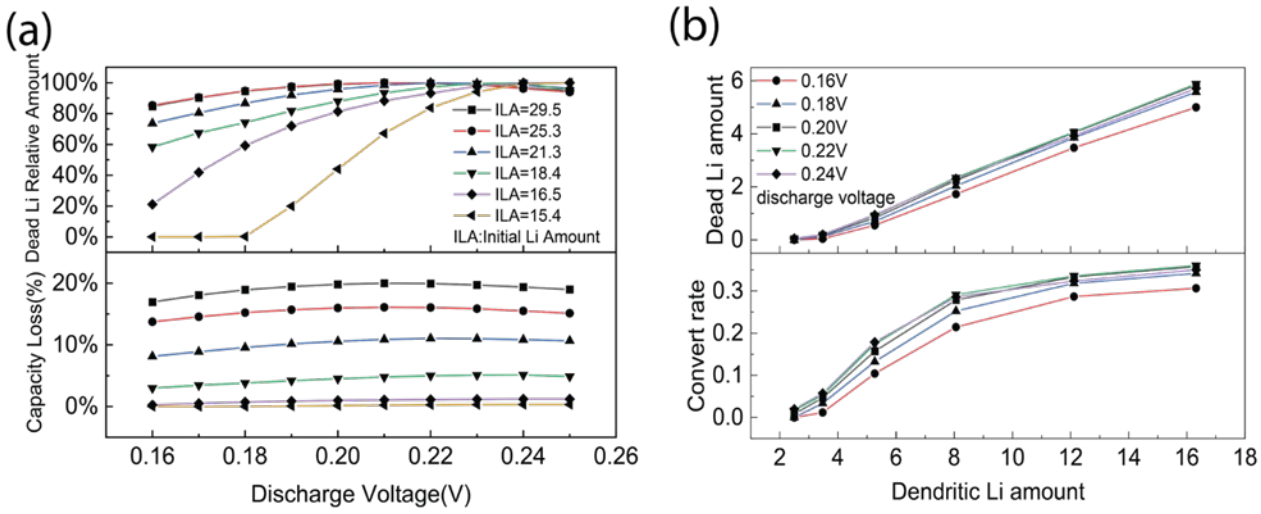

Figure 6-3 (a) (upper) dead Li relative amount and (lower) the capacity loss under different initial Li amounts and different discharge voltages. (b) (upper) the dead Li amount and (lower) the convert rate of dendritic Li to dead Li under different discharge voltages and dendritic Li amounts.

Chapter 7. Zn battery solvation energy

7.1 Introduction

Zinc is a promising anode material because of its high theoretical capacity (5855 mAh mL^{-1} and 820 mAh g^{-1}) and low redox potential (-0.76 V versus the standard hydrogen electrode, SHE)[212–215]. Moreover, zinc's compatibility with non-flammable aqueous electrolytes makes zinc batteries safe, environmentally friendly, and cost-effective[216,217]. Therefore, aqueous zinc batteries (AZBs) are considered as an alternative to lithium-ion batteries in large-scale energy storage. However, AZBs suffer from electrode corrosion, poor Coulombic efficiency (CE), and dendrite growth during cycling, resulting in limited cycle life[218,219]. These challenges stem from the interaction between Zn metal and the aqueous electrolytes, which causes the decomposition of water to generate H_2 and produce an inactive by-product $Zn(OH)_4^{2-}$ on the Zn-metal surface[220,221].

Herein, for the first time, a common organic compound of THF was introduced into the 2M $ZnSO_4$ electrolyte. The THF was selected as the representative of cyclic ether in our study because of its small molecular size and one oxygen atom as a proton acceptor within the molecule, which moderately disrupts the water network. THF can form a hydrogen bond with H_2O to decrease the water activity, thus optimizing the solvation structure of the Zn hydration layer to suppress the decomposition of water and the generation of by-products. Therefore, the Zn metal anode shows an improved electrochemical behavior in 2M $ZnSO_4$ electrolyte with a small amount of THF (5% by volume).

7.2 Results and Discussion

DFT simulations are performed to study the Zn^{2+} solvation energy in the aqueous electrolytes. For the 2M $ZnSO_4$ electrolyte, Zn^{2+} is considered to coordinate with six H_2O molecules ($Zn[H_2O]_6^{2+}$) based on previous references[222,223]. After adding the THF to the electrolyte, five H_2O molecules and one THF molecule are configured with Zn^{2+} ($Zn[H_2O]_5[THF]^{2+}$) to calculate the optimized solvation structure and energy. The optimized solvation structures of Zn^{2+} in two different electrolytes mentioned above are shown in Figure 7-1 (a)(b), respectively. First, the total energy (E_{total}) of $Zn[H_2O]_6^{2+}$ and $Zn[H_2O]_5[THF]^{2+}$ solvation structures are calculated. Then, E_{H_2O} and E_{THF+H_2O} are calculated by removing the Zn^{2+} ion from the two solvation structures. Meanwhile, the energy of a single Zn^{2+} ion ($E_{Zn^{2+}}$) is also calculated separately. Finally, the solvation energy (E_{sol}) is calculated as the difference between E_{total} , $E_{H_2O/THF+H_2O}$ and $E_{Zn^{2+}}$ (Eq.(51)). These results are summarized in Table 3. It is found that the solvation energy of $Zn[H_2O]_6^{2+}$ is calculated to be -13.496eV, which agrees with the values in previous literature[222,224]. On the other hand, the solvation energy of $Zn[H_2O]_5[THF]^{2+}$ is -14.827eV, which is 1.331eV lower than that of $Zn[H_2O]_6^{2+}$, indicating that $Zn[H_2O]_5[THF]^{2+}$ is a more stable solvation structure. Although more bonds are formed between Zn^{2+} ion and O atoms in $Zn[H_2O]_6^{2+}$ than in $Zn[H_2O]_5[THF]^{2+}$, the average bond length in $Zn[H_2O]_6^{2+}$ (2.06Å based on our DFT calculations) is longer than that in $Zn[H_2O]_5[THF]^{2+}$ (1.98Å), and based on the structures of six H_2O / five H_2O + one THF molecules in Figure 7-2, more hydrogen bonds breaks in the process of forming $Zn[H_2O]_6^{2+}$ than $Zn[H_2O]_5[THF]^{2+}$. Both of these contribute to a lower solvation energy in $Zn[H_2O]_5[THF]^{2+}$.

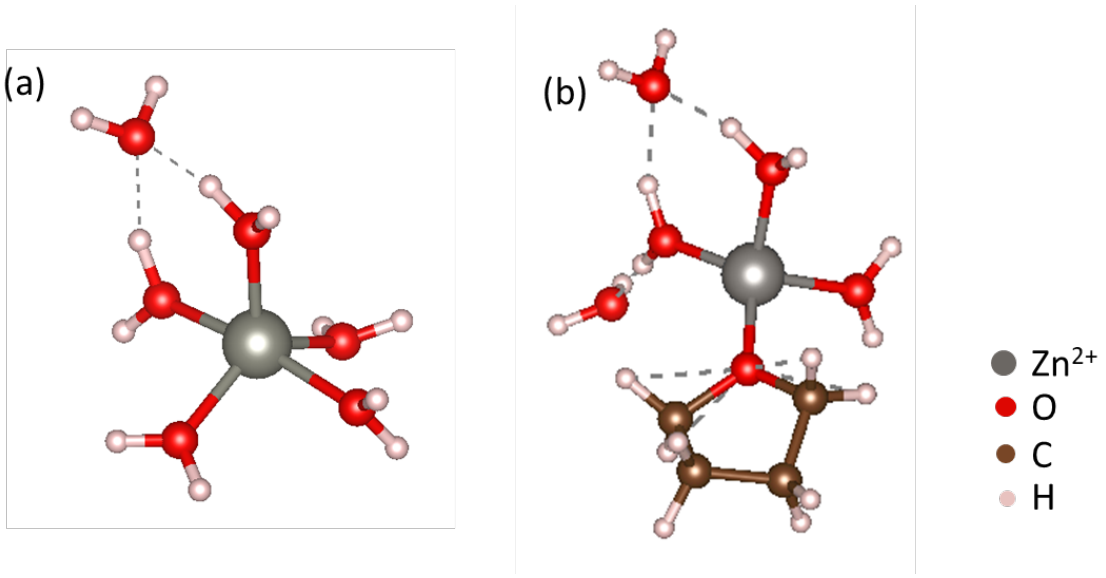

Figure 7-1 The optimized solvation structures of (a) $Zn[H_2O]_6^{2+}$ and (b) $Zn[H_2O]_5[THF]^{2+}$.

Table 3 The total energy of the two solvation structures (E_{total}), the energy of the H_2O/H_2O+THF molecule clusters ($E_{H_2O/THF+H_2O}$), and the energy of the isolated Zn^{2+} ion ($E_{Zn^{2+}}$). The corresponding solvation energies (E_{sol}) for the two solvation structure are calculated based on Eq.(51), and listed in the third column.

Species	Energy	E_{sol}
$E_{Zn^{2+}}$	+24.292eV	
E_{H_2O}	-87.738eV	
$E_{total(Zn[H_2O]_6^{2+})}$	-76.942eV	-13.496eV
E_{THF+H_2O}	-145.246eV	
$E_{total(Zn[H_2O]_5[THF]^{2+})}$	-135.781eV	-14.827eV

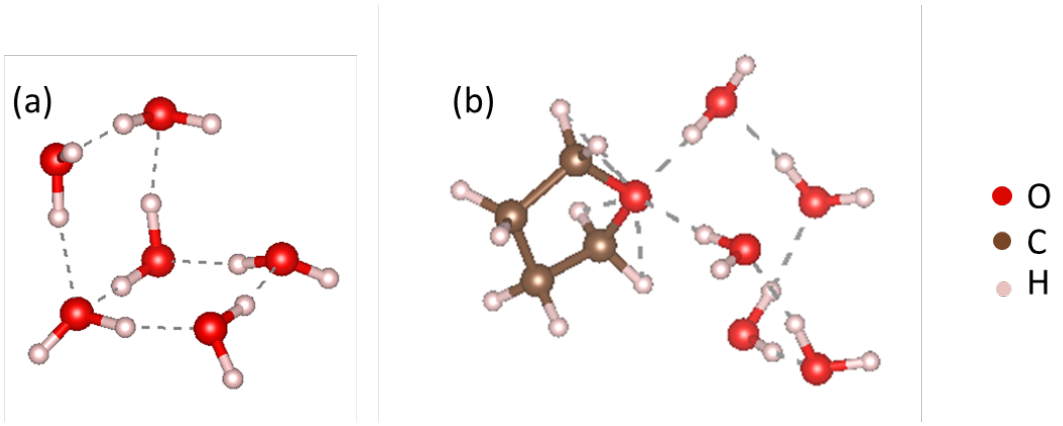

Figure 7-2 The optimized structures of (a) six H2O molecules and (b) five H2O and one THF molecules. Among them, it is seen that 7 hydron bonds formed in (a) and 10 hydron bonds formed in (b).

Chapter 8. Conclusions and Future Work

8.1 Conclusions

In conclusion, we develop a phase-field model coupled with heat transfer module, solid mechanics module and the nanofibers to study the electrodeposition process in solid state lithium battery system. Our simulation well captures the morphology of Li dendrite which agrees with experimental characterizations. The competition between diffusion rate and reaction rate is first explored. It is shown that a lower diffusion rate or a higher reaction rate will induce the Li dendrite on a smooth electrode as they both create an insufficient Li-ion area near the electrode. Then, the effect of the elastic and plastic mechanical properties of the Li metal and the solid electrolyte on Li dendrite growth are systematically investigated. It is revealed that electrolytes with high elastic modulus and initial yield strength can effectively inhibit the Li dendrite growth. This is because the high initial yield strength could help the electrolytes to endure higher deviatoric stresses that are induced by the higher elastic modulus, which eventually suppress the Li dendrite growth. Furthermore, increasing the initial yield strength of metal electrode could also lead to the dendrite inhibition in solid electrolytes of higher elastic modulus and lower initial yield strength. Also, high-throughput phase-field simulations are performed to explore the dependence of the Li dendrite morphology on the aforementioned mechanical properties of both the electrode and the electrolyte, and a machine learning model based on these high-throughput datasets yield interpretable analytical correlations between the materials properties and the dendrite morphology. This work thus provides a fundamental understanding of the mechanical inhibition effect on the dendrite growth in solid state batteries, and can

potentially guide the selection and design of electrode and electrolyte materials for better suppression of dendrite growth.

The introduction of 1D nanofiber arrays in the polymer electrolyte limit the Li^+ transport in random directions, thus favoring the fast Li^+ transport along horizontal direction and suppress the Li dendrite growth. This is due to the reduced Li^+ concentration in the electrolyte and improved Li^+ concentration at the metal surface, which decrease the Li^+ concentration gradient across the metal/electrolyte interface. The effect of nanochannel size on the Li dendrite growth has been recently observed experimentally, which further verify our simulation results. It is noteworthy that introducing the oxide nanofiber can also enhance the overall Li^+ conductivity in the composite electrolyte. To realize this the volume fraction of the nanofiber needs to be well controlled. We hope our work will incentive both theoretical and experimental studies on the effect of solid composite electrolyte on Li dendrite growth in the future.

Finally, the dead Li formation in the discharge process is also simulated by applying a positive overpotential. The dead Li is highly dependent on the dendritic part of Li metal electrode while the low discharge voltage can also inhibit the formation of dead Li. The discharge voltage should also be controlled to balance the output power and dead Li formation.

8.2 Future works

Solid electrolyte interface (SEI) layer plays an important role in the Li battery which involves the prevention of further electrolyte decomposition and the conduction of Li ions. In the charging process, the dendrite growth will lead to the rupture of the SEI layer which leads to the loss of active materials and the increase of internal resistance. In

the discharging process, dead Li is also formed due to the SEI layer completely covers the Li metal fragment. Therefore, the SEI layer should be considered during both processes. By introducing an extra order parameter, the SEI layer can be simulated and set as a layer evolving with the Li anode. Its thickness will also change with the surface curvature. With the introduction of SEI layer, the effects of its complicated properties (mechanical property, diffusivity) in the Li battery can be first explored. The aging of the Li battery can also be studied for the active material being consumed by the dead Li and SEI layer.

References

(1) Choi, J. W.; Aurbach, D. Promise and Reality of Post-Lithium-Ion Batteries with High Energy Densities. *Nat. Rev. Mater.* **2016**, *1* (4), 16013. https://doi.org/10.1038/natrevmats.2016.13.

(2) Goodenough, J. B.; Park, K.-S. The Li-Ion Rechargeable Battery: A Perspective. *J. Am. Chem. Soc.* **2013**, *135* (4), 1167–1176. https://doi.org/10.1021/ja3091438.

(3) Kim, H.; Jeong, G.; Kim, Y.-U.; Kim, J.-H.; Park, C.-M.; Sohn, H.-J. Metallic Anodes for next Generation Secondary Batteries. *Chem. Soc. Rev.* **2013**, *42* (23), 9011. https://doi.org/10.1039/c3cs60177c.

(4) Armand, M.; Tarascon, J.-M. Building Better Batteries. *Nature* **2008**, *451* (7179), 652–657. https://doi.org/10.1038/451652a.

(5) Lin, D.; Liu, Y.; Cui, Y. Reviving the Lithium Metal Anode for High-Energy Batteries. *Nat. Nanotechnol.* **2017**, *12* (3), 194–206. https://doi.org/10.1038/nnano.2017.16.

(6) Roth, E. P.; Orendorff, C. J. How Electrolytes Influence Battery Safety. *Interface Mag.* **2012**, *21* (2), 45–49. https://doi.org/10.1149/2.F04122if.

(7) Yang, C.; Fu, K.; Zhang, Y.; Hitz, E.; Hu, L. Protected Lithium-Metal Anodes in Batteries: From Liquid to Solid. *Adv. Mater.* **2017**, *29* (36), 1701169. https://doi.org/10.1002/adma.201701169.

(8) Zhang, W.; Nie, J.; Li, F.; Wang, Z. L.; Sun, C. A Durable and Safe Solid-State Lithium Battery with a Hybrid Electrolyte Membrane. *Nano Energy* **2018**, *45*, 413–419. https://doi.org/10.1016/j.nanoen.2018.01.028.

(9) Cheng, E. J.; Sharafi, A.; Sakamoto, J. Intergranular Li Metal Propagation through Polycrystalline Li6.25Al0.25La3Zr2O12 Ceramic Electrolyte. *Electrochimica Acta* **2017**, *223*, 85–91. https://doi.org/10.1016/j.electacta.2016.12.018.

(10) Campbell, C.; Lee, Y. M.; Cho, K. Y.; Lee, Y.-G.; Lee, B.; Phatak, C.; Hong, S. Effect of Nanopatterning on Mechanical Properties of Lithium Anode. *Sci. Rep.* **2018**, *8* (1), 2514. https://doi.org/10.1038/s41598-018-20773-8.

(11) Porz, L.; Swamy, T.; Sheldon, B. W.; Rettenwander, D.; Frömling, T.; Thaman, H. L.; Berendts, S.; Uecker, R.; Carter, W. C.; Chiang, Y. Mechanism of Lithium Metal Penetration through Inorganic Solid Electrolytes. *Adv. Energy Mater.* **2017**, *7* (20), 1701003. https://doi.org/10.1002/aenm.201701003.

(12) Li, Y.; Zhou, W.; Chen, X.; Lü, X.; Cui, Z.; Xin, S.; Xue, L.; Jia, Q.; Goodenough, J. B. Mastering the Interface for Advanced All-Solid-State Lithium Rechargeable Batteries. *Proc. Natl. Acad. Sci.* **2016**, *113* (47), 13313–13317. https://doi.org/10.1073/pnas.1615912113.

(13) Liu, Y.; Lin, D.; Yuen, P. Y.; Liu, K.; Xie, J.; Dauskardt, R. H.; Cui, Y. An Artificial Solid Electrolyte Interphase with High Li-Ion Conductivity, Mechanical Strength, and Flexibility for Stable Lithium Metal Anodes. *Adv. Mater.* **2017**, *29* (10), 1605531. https://doi.org/10.1002/adma.201605531.

(14) Liu, K.; Bai, P.; Bazant, M. Z.; Wang, C.-A.; Li, J. A Soft Non-Porous Separator and Its Effectiveness in Stabilizing Li Metal Anodes Cycling at 10 MA Cm^{-2} Observed in Situ in a Capillary Cell. *J. Mater. Chem. A* **2017**, *5* (9), 4300–4307. https://doi.org/10.1039/C7TA00069C.

(15) Campbell, C.; Lee, Y. M.; Cho, K. Y.; Lee, Y.-G.; Lee, B.; Phatak, C.; Hong, S. Effect of Nanopatterning on Mechanical Properties of Lithium Anode. *Sci. Rep.* **2018**, *8* (1), 2514. https://doi.org/10.1038/s41598-018-20773-8.
(16) Xu, C.; Ahmad, Z.; Aryanfar, A.; Viswanathan, V.; Greer, J. R. Enhanced Strength and Temperature Dependence of Mechanical Properties of Li at Small Scales and Its Implications for Li Metal Anodes. *Proc. Natl. Acad. Sci.* **2017**, *114* (1), 57–61. https://doi.org/10.1073/pnas.1615733114.
(17) LePage, W. S.; Chen, Y.; Kazyak, E.; Chen, K.-H.; Sanchez, A. J.; Poli, A.; Arruda, E. M.; Thouless, M. D.; Dasgupta, N. P. Lithium Mechanics: Roles of Strain Rate and Temperature and Implications for Lithium Metal Batteries. *J. Electrochem. Soc.* **2019**, *166* (2), A89–A97. https://doi.org/10.1149/2.0221902jes.
(18) Wang, Y.; Cheng, Y.-T. A Nanoindentation Study of the Viscoplastic Behavior of Pure Lithium. *Scr. Mater.* **2017**, *130*, 191–195. https://doi.org/10.1016/j.scriptamat.2016.12.006.
(19) Cano, Z. P.; Banham, D.; Ye, S.; Hintennach, A.; Lu, J.; Fowler, M.; Chen, Z. Batteries and Fuel Cells for Emerging Electric Vehicle Markets. *Nat. Energy* **2018**, *3* (4), 279–289. https://doi.org/10.1038/s41560-018-0108-1.
(20) Tarascon, J.-M.; Armand, M. Issues and Challenges Facing Rechargeable Lithium Batteries. In *Materials for Sustainable Energy*; Co-Published with Macmillan Publishers Ltd, UK, 2010; pp 171–179. https://doi.org/10.1142/9789814317665_0024.
(21) Scrosati, B. History of Lithium Batteries. *J. Solid State Electrochem.* **2011**, *15* (7–8), 1623–1630. https://doi.org/10.1007/s10008-011-1386-8.
(22) *Progress in Batteries and Solar Cells. 1990*; 1990.
(23) Murphy, D. W.; Carides, J. N. Low Voltage Behavior of Lithium/Metal Dichalcogenide Topochemical Cells. *J. Electrochem. Soc.* **1979**, *126* (3), 349–351. https://doi.org/10.1149/1.2129041.
(24) Murphy, D. *Materials for Advanced Batteries*; Springer: New York, NY, 1981.
(25) Manthiram, A. An Outlook on Lithium Ion Battery Technology. *ACS Cent. Sci.* **2017**, *3* (10), 1063–1069. https://doi.org/10.1021/acscentsci.7b00288.
(26) Bin, D.; Wen, Y.; Wang, Y.; Xia, Y. The Development in Aqueous Lithium-Ion Batteries. *J. Energy Chem.* **2018**, *27* (6), 1521–1535. https://doi.org/10.1016/j.jechem.2018.06.004.
(27) Liang, Z.; Zheng, G.; Liu, C.; Liu, N.; Li, W.; Yan, K.; Yao, H.; Hsu, P.-C.; Chu, S.; Cui, Y. Polymer Nanofiber-Guided Uniform Lithium Deposition for Battery Electrodes. *Nano Lett.* **2015**, *15* (5), 2910–2916. https://doi.org/10.1021/nl5046318.
(28) Safari, M.; Kwok, C. Y.; Nazar, L. F. Transport Properties of Polysulfide Species in Lithium–Sulfur Battery Electrolytes: Coupling of Experiment and Theory. *ACS Cent. Sci.* **2016**, *2* (8), 560–568. https://doi.org/10.1021/acscentsci.6b00169.
(29) Bruce, P. G.; Freunberger, S. A.; Hardwick, L. J.; Tarascon, J.-M. Li–O2 and Li–S Batteries with High Energy Storage. *Nat. Mater.* **2012**, *11* (1), 19–29. https://doi.org/10.1038/nmat3191.
(30) Jurng, S.; Brown, Z. L.; Kim, J.; Lucht, B. L. Effect of Electrolyte on the Nanostructure of the Solid Electrolyte Interphase (SEI) and Performance of Lithium Metal Anodes. *Energy Environ. Sci.* **2018**, *11* (9), 2600–2608. https://doi.org/10.1039/C8EE00364E.

(31) Kim, Y.; Koo, D.; Ha, S.; Jung, S. C.; Yim, T.; Kim, H.; Oh, S. K.; Kim, D.-M.; Choi, A.; Kang, Y.; Ryu, K. H.; Jang, M.; Han, Y.-K.; Oh, S. M.; Lee, K. T. Two-Dimensional Phosphorene-Derived Protective Layers on a Lithium Metal Anode for Lithium-Oxygen Batteries. *ACS Nano* **2018**, *12* (5), 4419–4430. https://doi.org/10.1021/acsnano.8b00348.
(32) Li, L.; Li, S.; Lu, Y. Suppression of Dendritic Lithium Growth in Lithium Metal-Based Batteries. *Chem. Commun.* **2018**, *54* (50), 6648–6661. https://doi.org/10.1039/C8CC02280A.
(33) Xu, R.; Zhang, X.-Q.; Cheng, X.-B.; Peng, H.-J.; Zhao, C.-Z.; Yan, C.; Huang, J.-Q. Artificial Soft-Rigid Protective Layer for Dendrite-Free Lithium Metal Anode. *Adv. Funct. Mater.* **2018**, *28* (8), 1705838. https://doi.org/10.1002/adfm.201705838.
(34) Xu, W.; Wang, J.; Ding, F.; Chen, X.; Nasybulin, E.; Zhang, Y.; Zhang, J.-G. Lithium Metal Anodes for Rechargeable Batteries. *Energy Env. Sci* **2014**, *7* (2), 513–537. https://doi.org/10.1039/C3EE40795K.
(35) Zachman, M. J.; Tu, Z.; Choudhury, S.; Archer, L. A.; Kourkoutis, L. F. Cryo-STEM Mapping of Solid–Liquid Interfaces and Dendrites in Lithium-Metal Batteries. *Nature* **2018**, *560* (7718), 345–349. https://doi.org/10.1038/s41586-018-0397-3.
(36) Cheng, X.-B.; Zhang, R.; Zhao, C.-Z.; Zhang, Q. Toward Safe Lithium Metal Anode in Rechargeable Batteries: A Review. *Chem. Rev.* **2017**, *117* (15), 10403–10473. https://doi.org/10.1021/acs.chemrev.7b00115.
(37) Chazalviel, J.-N. Electrochemical Aspects of the Generation of Ramified Metallic Electrodeposits. *Phys. Rev. A* **1990**, *42* (12), 7355–7367. https://doi.org/10.1103/PhysRevA.42.7355.
(38) Brissot, C.; Rosso, M.; Chazalviel, J.-N.; Lascaud, S. Dendritic Growth Mechanisms in Lithium/Polymer Cells. *J. Power Sources* **1999**, *81–82*, 925–929. https://doi.org/10.1016/S0378-7753(98)00242-0.
(39) Sand, H. J. S. III. *On the Concentration at the Electrodes in a Solution, with Special Reference to the Liberation of Hydrogen by Electrolysis of a Mixture of Copper Sulphate and Sulphuric Acid*. *Lond. Edinb. Dublin Philos. Mag. J. Sci.* **1901**, *1* (1), 45–79. https://doi.org/10.1080/14786440109462590.
(40) Rosso, M.; Gobron, T.; Brissot, C.; Chazalviel, J.-N.; Lascaud, S. Onset of Dendritic Growth in Lithium/Polymer Cells. *J. Power Sources* **2001**, *97–98*, 804–806. https://doi.org/10.1016/S0378-7753(01)00734-0.
(41) Cohen, Y. S.; Cohen, Y.; Aurbach, D. Micromorphological Studies of Lithium Electrodes in Alkyl Carbonate Solutions Using in Situ Atomic Force Microscopy. *J. Phys. Chem. B* **2000**, *104* (51), 12282–12291. https://doi.org/10.1021/jp002526b.
(42) Chen, N.; Dai, Y.; Xing, Y.; Wang, L.; Guo, C.; Chen, R.; Guo, S.; Wu, F. Biomimetic Ant-Nest Ionogel Electrolyte Boosts the Performance of Dendrite-Free Lithium Batteries. *Energy Environ. Sci.* **2017**, *10* (7), 1660–1667. https://doi.org/10.1039/C7EE00988G.
(43) Cheng, X.-B.; Zhao, M.-Q.; Chen, C.; Pentecost, A.; Maleski, K.; Mathis, T.; Zhang, X.-Q.; Zhang, Q.; Jiang, J.; Gogotsi, Y. Nanodiamonds Suppress the Growth of Lithium Dendrites. *Nat. Commun.* **2017**, *8* (1), 336. https://doi.org/10.1038/s41467-017-00519-2.

(44) Ding, F.; Xu, W.; Graff, G. L.; Zhang, J.; Sushko, M. L.; Chen, X.; Shao, Y.; Engelhard, M. H.; Nie, Z.; Xiao, J.; Liu, X.; Sushko, P. V.; Liu, J.; Zhang, J.-G. Dendrite-Free Lithium Deposition via Self-Healing Electrostatic Shield Mechanism. *J. Am. Chem. Soc.* **2013**, *135* (11), 4450–4456. https://doi.org/10.1021/ja312241y.
(45) Jiao, S.; Ren, X.; Cao, R.; Engelhard, M. H.; Liu, Y.; Hu, D.; Mei, D.; Zheng, J.; Zhao, W.; Li, Q.; Liu, N.; Adams, B. D.; Ma, C.; Liu, J.; Zhang, J.-G.; Xu, W. Stable Cycling of High-Voltage Lithium Metal Batteries in Ether Electrolytes. *Nat. Energy* **2018**, *3* (9), 739–746. https://doi.org/10.1038/s41560-018-0199-8.
(46) Tan, J.; Ryan, E. M. Structured Electrolytes to Suppress Dendrite Growth in High Energy Density Batteries: Structured Electrolytes to Suppress Dendrite Growth. *Int. J. Energy Res.* **2016**, *40* (13), 1800–1810. https://doi.org/10.1002/er.3560.
(47) Wood, S. M.; Pham, C. H.; Rodriguez, R.; Nathan, S. S.; Dolocan, A. D.; Celio, H.; de Souza, J. P.; Klavetter, K. C.; Heller, A.; Mullins, C. B. K+ Reduces Lithium Dendrite Growth by Forming a Thin, Less-Resistive Solid Electrolyte Interphase. *ACS Energy Lett.* **2016**, *1* (2), 414–419. https://doi.org/10.1021/acsenergylett.6b00259.
(48) Bai, M.; Xie, K.; Yuan, K.; Zhang, K.; Li, N.; Shen, C.; Lai, Y.; Vajtai, R.; Ajayan, P.; Wei, B. A Scalable Approach to Dendrite-Free Lithium Anodes via Spontaneous Reduction of Spray-Coated Graphene Oxide Layers. *Adv. Mater.* **2018**, *30* (29), 1801213. https://doi.org/10.1002/adma.201801213.
(49) Cha, E.; Patel, M. D.; Park, J.; Hwang, J.; Prasad, V.; Cho, K.; Choi, W. 2D MoS2 as an Efficient Protective Layer for Lithium Metal Anodes in High-Performance Li–S Batteries. *Nat. Nanotechnol.* **2018**, *13* (4), 337–344. https://doi.org/10.1038/s41565-018-0061-y.
(50) Li, W.; Yao, H.; Yan, K.; Zheng, G.; Liang, Z.; Chiang, Y.-M.; Cui, Y. The Synergetic Effect of Lithium Polysulfide and Lithium Nitrate to Prevent Lithium Dendrite Growth. *Nat. Commun.* **2015**, *6* (1), 7436. https://doi.org/10.1038/ncomms8436.
(51) Liang, X.; Pang, Q.; Kochetkov, I. R.; Sempere, M. S.; Huang, H.; Sun, X.; Nazar, L. F. A Facile Surface Chemistry Route to a Stabilized Lithium Metal Anode. *Nat. Energy* **2017**, *2* (9), 17119. https://doi.org/10.1038/nenergy.2017.119.
(52) Liu, K.; Pei, A.; Lee, H. R.; Kong, B.; Liu, N.; Lin, D.; Liu, Y.; Liu, C.; Hsu, P.; Bao, Z.; Cui, Y. Lithium Metal Anodes with an Adaptive "Solid-Liquid" Interfacial Protective Layer. *J. Am. Chem. Soc.* **2017**, *139* (13), 4815–4820. https://doi.org/10.1021/jacs.6b13314.
(53) Ma, L.; Kim, M. S.; Archer, L. A. Stable Artificial Solid Electrolyte Interphases for Lithium Batteries. *Chem. Mater.* **2017**, *29* (10), 4181–4189. https://doi.org/10.1021/acs.chemmater.6b03687.
(54) Jeong, S.-K.; Seo, H.-Y.; Kim, D.-H.; Han, H.-K.; Kim, J.-G.; Lee, Y. B.; Iriyama, Y.; Abe, T.; Ogumi, Z. Suppression of Dendritic Lithium Formation by Using Concentrated Electrolyte Solutions. *Electrochem. Commun.* **2008**, *10* (4), 635–638. https://doi.org/10.1016/j.elecom.2008.02.006.
(55) Yamada, Y.; Furukawa, K.; Sodeyama, K.; Kikuchi, K.; Yaegashi, M.; Tateyama, Y.; Yamada, A. Unusual Stability of Acetonitrile-Based Superconcentrated Electrolytes for Fast-Charging Lithium-Ion Batteries. *J. Am. Chem. Soc.* **2014**, *136* (13), 5039–5046. https://doi.org/10.1021/ja412807w.

(56) Liu, B.; Xu, W.; Yan, P.; Sun, X.; Bowden, M. E.; Read, J.; Qian, J.; Mei, D.; Wang, C.-M.; Zhang, J.-G. Enhanced Cycling Stability of Rechargeable Li-O_2 Batteries Using High-Concentration Electrolytes. *Adv. Funct. Mater.* **2016**, *26* (4), 605–613. https://doi.org/10.1002/adfm.201503697.
(57) Ma, Q.; Fang, Z.; Liu, P.; Ma, J.; Qi, X.; Feng, W.; Nie, J.; Hu, Y.-S.; Li, H.; Huang, X.; Chen, L.; Zhou, Z. Improved Cycling Stability of Lithium-Metal Anode with Concentrated Electrolytes Based on Lithium (Fluorosulfonyl)(Trifluoromethanesulfonyl)Imide. *ChemElectroChem* **2016**, *3* (4), 531–536. https://doi.org/10.1002/celc.201500520.
(58) Suo, L.; Hu, Y.-S.; Li, H.; Armand, M.; Chen, L. A New Class of Solvent-in-Salt Electrolyte for High-Energy Rechargeable Metallic Lithium Batteries. *Nat. Commun.* **2013**, *4* (1), 1481. https://doi.org/10.1038/ncomms2513.
(59) Yamada, Y.; Yamada, A. Review—Superconcentrated Electrolytes for Lithium Batteries. *J. Electrochem. Soc.* **2015**, *162* (14), A2406–A2423. https://doi.org/10.1149/2.0041514jes.
(60) Zheng, J.; Lochala, J. A.; Kwok, A.; Deng, Z. D.; Xiao, J. Research Progress towards Understanding the Unique Interfaces between Concentrated Electrolytes and Electrodes for Energy Storage Applications. *Adv. Sci.* **2017**, *4* (8), 1700032. https://doi.org/10.1002/advs.201700032.
(61) Khurana, R.; Schaefer, J. L.; Archer, L. A.; Coates, G. W. Suppression of Lithium Dendrite Growth Using Cross-Linked Polyethylene/Poly(Ethylene Oxide) Electrolytes: A New Approach for Practical Lithium-Metal Polymer Batteries. *J. Am. Chem. Soc.* **2014**, *136* (20), 7395–7402. https://doi.org/10.1021/ja502133j.
(62) Shin, W.-K.; Kannan, A. G.; Kim, D.-W. Effective Suppression of Dendritic Lithium Growth Using an Ultrathin Coating of Nitrogen and Sulfur Codoped Graphene Nanosheets on Polymer Separator for Lithium Metal Batteries. *ACS Appl. Mater. Interfaces* **2015**, *7* (42), 23700–23707. https://doi.org/10.1021/acsami.5b07730.
(63) Wu, H.; Zhuo, D.; Kong, D.; Cui, Y. Improving Battery Safety by Early Detection of Internal Shorting with a Bifunctional Separator. *Nat. Commun.* **2014**, *5* (1), 5193. https://doi.org/10.1038/ncomms6193.
(64) Yu, B.-C.; Park, K.; Jang, J.-H.; Goodenough, J. B. Cellulose-Based Porous Membrane for Suppressing Li Dendrite Formation in Lithium–Sulfur Battery. *ACS Energy Lett.* **2016**, *1* (3), 633–637. https://doi.org/10.1021/acsenergylett.6b00209.
(65) Zhang, J.; Yue, L.; Kong, Q.; Liu, Z.; Zhou, X.; Zhang, C.; Xu, Q.; Zhang, B.; Ding, G.; Qin, B.; Duan, Y.; Wang, Q.; Yao, J.; Cui, G.; Chen, L. Sustainable, Heat-Resistant and Flame-Retardant Cellulose-Based Composite Separator for High-Performance Lithium Ion Battery. *Sci. Rep.* **2015**, *4* (1), 3935. https://doi.org/10.1038/srep03935.
(66) Ghazi, Z. A.; He, X.; Khattak, A. M.; Khan, N. A.; Liang, B.; Iqbal, A.; Wang, J.; Sin, H.; Li, L.; Tang, Z. MoS_2 /Celgard Separator as Efficient Polysulfide Barrier for Long-Life Lithium-Sulfur Batteries. *Adv. Mater.* **2017**, *29* (21), 1606817. https://doi.org/10.1002/adma.201606817.
(67) Sun, J.; Sun, Y.; Pasta, M.; Zhou, G.; Li, Y.; Liu, W.; Xiong, F.; Cui, Y. Entrapment of Polysulfides by a Black-Phosphorus-Modified Separator for Lithium-Sulfur

Batteries. *Adv. Mater.* **2016**, *28* (44), 9797–9803. https://doi.org/10.1002/adma.201602172.
(68) Lu, Y.; Tu, Z.; Archer, L. A. Stable Lithium Electrodeposition in Liquid and Nanoporous Solid Electrolytes. *Nat. Mater.* **2014**, *13* (10), 961–969. https://doi.org/10.1038/nmat4041.
(69) Wu, M.; Wen, Z.; Jin, J.; Cui, Y. Effects of Combinatorial AlCl3 and Pyrrole on the SEI Formation and Electrochemical Performance of Li Electrode. *Electrochimica Acta* **2013**, *103*, 199–205. https://doi.org/10.1016/j.electacta.2013.03.181.
(70) Yoon, S.; Lee, J.; Kim, S.-O.; Sohn, H.-J. Enhanced Cyclability and Surface Characteristics of Lithium Batteries by Li–Mg Co-Deposition and Addition of HF Acid in Electrolyte. *Electrochimica Acta* **2008**, *53* (5), 2501–2506. https://doi.org/10.1016/j.electacta.2007.10.019.
(71) Xu, K. Nonaqueous Liquid Electrolytes for Lithium-Based Rechargeable Batteries. *Chem. Rev.* **2004**, *104* (10), 4303–4418. https://doi.org/10.1021/cr030203g.
(72) Quartarone, E.; Mustarelli, P. Electrolytes for Solid-State Lithium Rechargeable Batteries: Recent Advances and Perspectives. *Chem. Soc. Rev.* **2011**, *40* (5), 2525. https://doi.org/10.1039/c0cs00081g.
(73) Hu, Y.-S. Batteries: Getting Solid. *Nat. Energy* **2016**, *1* (4), 16042. https://doi.org/10.1038/nenergy.2016.42.
(74) Fergus, J. W. Ceramic and Polymeric Solid Electrolytes for Lithium-Ion Batteries. *J. Power Sources* **2010**, *195* (15), 4554–4569. https://doi.org/10.1016/j.jpowsour.2010.01.076.
(75) Xia, W.; Xu, B.; Duan, H.; Guo, Y.; Kang, H.; Li, H.; Liu, H. Ionic Conductivity and Air Stability of Al-Doped Li $_7$ La $_3$ Zr $_2$ O $_{12}$ Sintered in Alumina and Pt Crucibles. *ACS Appl. Mater. Interfaces* **2016**, *8* (8), 5335–5342. https://doi.org/10.1021/acsami.5b12186.
(76) Matsuyama, T.; Sakuda, A.; Hayashi, A.; Togawa, Y.; Mori, S.; Tatsumisago, M. Electrochemical Properties of All-Solid-State Lithium Batteries with Amorphous Titanium Sulfide Electrodes Prepared by Mechanical Milling. *J. Solid State Electrochem.* **2013**, *17* (10), 2697–2701. https://doi.org/10.1007/s10008-013-2157-5.
(77) Manthiram, A.; Yu, X.; Wang, S. Lithium Battery Chemistries Enabled by Solid-State Electrolytes. *Nat. Rev. Mater.* **2017**, *2* (4), 16103. https://doi.org/10.1038/natrevmats.2016.103.
(78) Inaguma, Y.; Liquan, C.; Itoh, M.; Nakamura, T.; Uchida, T.; Ikuta, H.; Wakihara, M. High Ionic Conductivity in Lithium Lanthanum Titanate. *Solid State Commun.* **1993**, *86* (10), 689–693. https://doi.org/10.1016/0038-1098(93)90841-A.
(79) Goodenough, J. B.; Hong, H. Y.-P.; Kafalas, J. A. Fast Na+-Ion Transport in Skeleton Structures. *Mater. Res. Bull.* **1976**, *11* (2), 203–220. https://doi.org/10.1016/0025-5408(76)90077-5.
(80) Thangadurai, V.; Weppner, W. Recent Progress in Solid Oxide and Lithium Ion Conducting Electrolytes Research. *Ionics* **2006**, *12* (1), 81–92. https://doi.org/10.1007/s11581-006-0013-7.
(81) Aono, H. Ionic Conductivity and Sinterability of Lithium Titanium Phosphate System. *Solid State Ion.* **1990**, *40–41*, 38–42. https://doi.org/10.1016/0167-2738(90)90282-V.

(82) Morimoto, H.; Awano, H.; Terashima, J.; Shindo, Y.; Nakanishi, S.; Ito, N.; Ishikawa, K.; Tobishima, S. Preparation of Lithium Ion Conducting Solid Electrolyte of NASICON-Type Li1+xAlxTi2−x(PO4)3 (x = 0.3) Obtained by Using the Mechanochemical Method and Its Application as Surface Modification Materials of LiCoO2 Cathode for Lithium Cell. *J. Power Sources* **2013**, *240*, 636–643. https://doi.org/10.1016/j.jpowsour.2013.05.039.
(83) Xu, X.; Wen, Z.; Wu, X.; Yang, X.; Gu, Z. Lithium Ion-Conducting Glass?Ceramics of $Li_{1.5}Al_{0.5}Ge_{1.5}(PO_4)_3$?$XLi_2O$ (X=0.0?0.20) with Good Electrical and Electrochemical Properties. *J. Am. Ceram. Soc.* **2007**, *90* (9), 2802–2806. https://doi.org/10.1111/j.1551-2916.2007.01827.x.
(84) Xu, X.; Wen, Z.; Yang, X.; Chen, L. Dense Nanostructured Solid Electrolyte with High Li-Ion Conductivity by Spark Plasma Sintering Technique. *Mater. Res. Bull.* **2008**, *43* (8–9), 2334–2341. https://doi.org/10.1016/j.materresbull.2007.08.007.
(85) Cruz, A. M.; Ferreira, E. B.; Rodrigues, A. C. M. Controlled Crystallization and Ionic Conductivity of a Nanostructured LiAlGePO4 Glass–Ceramic. *J. Non-Cryst. Solids* **2009**, *355* (45–47), 2295–2301. https://doi.org/10.1016/j.jnoncrysol.2009.07.012.
(86) Fu, J. Fast Li+ Ion Conducting Glass-Ceramics in the System Li2O–Al2O3–GeO2–P2O5. *Solid State Ion.* **1997**, *104* (3–4), 191–194. https://doi.org/10.1016/S0167-2738(97)00434-7.
(87) Thokchom, J. S.; Gupta, N.; Kumar, B. Superionic Conductivity in a Lithium Aluminum Germanium Phosphate Glass–Ceramic. *J. Electrochem. Soc.* **2008**, *155* (12), A915. https://doi.org/10.1149/1.2988731.
(88) Kasper, H. M. Series of Rare Earth Garnets Ln3+ 3M2Li+ 3O12 (M= Te, W). *Inorg. Chem.* **1969**, *8* (4), 1000–1002.
(89) Thangadurai, V.; Kaack, H.; Weppner, W. J. F. Novel Fast Lithium Ion Conduction in Garnet-Type $Li_5La_3M_2O_{12}$ (M = Nb, Ta). *J. Am. Ceram. Soc.* **2003**, *86* (3), 437–440. https://doi.org/10.1111/j.1151-2916.2003.tb03318.x.
(90) Geiger, C. A.; Alekseev, E.; Lazic, B.; Fisch, M.; Armbruster, T.; Langner, R.; Fechtelkord, M.; Kim, N.; Pettke, T.; Weppner, W. Crystal Chemistry and Stability of "$Li_7La_3Zr_2O_{12}$" Garnet: A Fast Lithium-Ion Conductor. *Inorg. Chem.* **2011**, *50* (3), 1089–1097. https://doi.org/10.1021/ic101914e.
(91) Murugan, R.; Ramakumar, S.; Janani, N. High Conductive Yttrium Doped Li7La3Zr2O12 Cubic Lithium Garnet. *Electrochem. Commun.* **2011**, *13* (12), 1373–1375. https://doi.org/10.1016/j.elecom.2011.08.014.
(92) Allen, J. L.; Wolfenstine, J.; Rangasamy, E.; Sakamoto, J. Effect of Substitution (Ta, Al, Ga) on the Conductivity of Li7La3Zr2O12. *J. Power Sources* **2012**, *206*, 315–319. https://doi.org/10.1016/j.jpowsour.2012.01.131.
(93) Ohta, S.; Kobayashi, T.; Asaoka, T. High Lithium Ionic Conductivity in the Garnet-Type Oxide Li7−X La3(Zr2−X, NbX)O12 (X=0–2). *J. Power Sources* **2011**, *196* (6), 3342–3345. https://doi.org/10.1016/j.jpowsour.2010.11.089.
(94) Deviannapoorani, C.; Dhivya, L.; Ramakumar, S.; Murugan, R. Lithium Ion Transport Properties of High Conductive Tellurium Substituted Li7La3Zr2O12 Cubic Lithium Garnets. *J. Power Sources* **2013**, *240*, 18–25. https://doi.org/10.1016/j.jpowsour.2013.03.166.

(95) Kennedy, J.; Sahami, S.; Shea, S.; Zhang, Z. Preparation and Conductivity Measurements of SiS2□Li2S Glasses Doped with LiBr and LiCl. *Solid State Ion.* **1986**, *18–19*, 368–371. https://doi.org/10.1016/0167-2738(86)90142-6.
(96) Kanno, R.; Murayama, M. Lithium Ionic Conductor Thio-LISICON: The Li[Sub 2]S-GeS[Sub 2]-P[Sub 2]S[Sub 5] System. *J. Electrochem. Soc.* **2001**, *148* (7), A742. https://doi.org/10.1149/1.1379028.
(97) Hayashi, A.; Ohtomo, T.; Mizuno, F.; Tadanaga, K.; Tatsumisago, M. All-Solid-State Li/S Batteries with Highly Conductive Glass–Ceramic Electrolytes. *Electrochem. Commun.* **2003**, *5* (8), 701–705. https://doi.org/10.1016/S1388-2481(03)00167-X.
(98) Liu, Z.; Fu, W.; Payzant, E. A.; Yu, X.; Wu, Z.; Dudney, N. J.; Kiggans, J.; Hong, K.; Rondinone, A. J.; Liang, C. Anomalous High Ionic Conductivity of Nanoporous β-Li $_3$ PS $_4$. *J. Am. Chem. Soc.* **2013**, *135* (3), 975–978. https://doi.org/10.1021/ja3110895.
(99) Mizuno, F.; Hayashi, A.; Tadanaga, K.; Tatsumisago, M. New, Highly Ion-Conductive Crystals Precipitated from Li2S-P2S5 Glasses. *Adv. Mater.* **2005**, *17* (7), 918–921. https://doi.org/10.1002/adma.200401286.
(100) Rangasamy, E.; Liu, Z.; Gobet, M.; Pilar, K.; Sahu, G.; Zhou, W.; Wu, H.; Greenbaum, S.; Liang, C. An Iodide-Based Li $_7$ P $_2$ S $_8$ I Superionic Conductor. *J. Am. Chem. Soc.* **2015**, *137* (4), 1384–1387. https://doi.org/10.1021/ja508723m.
(101) Hayashi, A.; Muramatsu, H.; Ohtomo, T.; Hama, S.; Tatsumisago, M. Improved Chemical Stability and Cyclability in Li2S–P2S5–P2O5–ZnO Composite Electrolytes for All-Solid-State Rechargeable Lithium Batteries. *J. Alloys Compd.* **2014**, *591*, 247–250. https://doi.org/10.1016/j.jallcom.2013.12.191.
(102) Minami, K.; Hayashi, A.; Ujiie, S.; Tatsumisago, M. Electrical and Electrochemical Properties of Glass–Ceramic Electrolytes in the Systems Li2S–P2S5–P2S3 and Li2S–P2S5–P2O5. *Solid State Ion.* **2011**, *192* (1), 122–125. https://doi.org/10.1016/j.ssi.2010.06.018.
(103) Muramatsu, H.; Hayashi, A.; Ohtomo, T.; Hama, S.; Tatsumisago, M. Structural Change of Li2S–P2S5 Sulfide Solid Electrolytes in the Atmosphere. *Solid State Ion.* **2011**, *182* (1), 116–119. https://doi.org/10.1016/j.ssi.2010.10.013.
(104) Alamgir, M.; Abraham, K. M. Li Ion Conductive Electrolytes Based on Poly(Vinyl Chloride). *J. Electrochem. Soc.* **1993**, *140* (6), L96–L97. https://doi.org/10.1149/1.2221654.
(105) Capiglia, C. Structure and Transport Properties of Polymer Gel Electrolytes Based on PVdF-HFP and LiN(C2F5SO2)2. *Solid State Ion.* **2000**, *131* (3–4), 291–299. https://doi.org/10.1016/S0167-2738(00)00678-0.
(106) Feuillade, G.; Perche, Ph. Ion-Conductive Macromolecular Gels and Membranes for Solid Lithium Cells. *J. Appl. Electrochem.* **1975**, *5* (1), 63–69. https://doi.org/10.1007/BF00625960.
(107) Zhou, Y. F.; Xie, S.; Ge, X. W.; Chen, C. H.; Amine, K. Preparation of Rechargeable Lithium Batteries with Poly(Methyl Methacrylate) Based Gel Polymer Electrolyte by in Situ?-Ray Irradiation-Induced Polymerization. *J. Appl. Electrochem.* **2004**, *34* (11), 1119–1125. https://doi.org/10.1007/s10800-004-2726-5.

(108) Chen-Yang, Y. Polyacrylonitrile Electrolytes 1. A Novel High-Conductivity Composite Polymer Electrolyte Based on PAN, LiClO4 and α-Al2O3. *Solid State Ion.* **2002**, *150* (3–4), 327–335. https://doi.org/10.1016/S0167-2738(02)00457-5.
(109) Di Noto, V.; Zago, V. Inorganic-Organic Polymer Electrolytes Based on PEG400 and Al[OCH(CH[Sub 3])[Sub 2]][Sub 3]. *J. Electrochem. Soc.* **2004**, *151* (2), A216. https://doi.org/10.1149/1.1635825.
(110) Liu, Y.; Lee, J. Y.; Hong, L. In Situ Preparation of Poly(Ethylene Oxide)–SiO2 Composite Polymer Electrolytes. *J. Power Sources* **2004**, *129* (2), 303–311. https://doi.org/10.1016/j.jpowsour.2003.11.026.
(111) Magistris, A. Transport and Thermal Properties of (PEO)n–LiPF6 Electrolytes for Super-Ambient Applications. *Solid State Ion.* **2000**, *136–137* (1–2), 1241–1247. https://doi.org/10.1016/S0167-2738(00)00594-4.
(112) Marcinek, M.; Ciosek, M.; Zukowska, G.; Wieczorek, W.; Jeffrey, K.; Stevens, J. Ionic Association in Liquid (Polyether–AlO–LiClO) Composite Electrolytes. *Solid State Ion.* **2005**, *176* (3–4), 367–376. https://doi.org/10.1016/j.ssi.2004.08.013.
(113) Appetecchi, G. B.; Croce, F.; Persi, L.; Ronci, F.; Scrosati, B. Transport and Interfacial Properties of Composite Polymer Electrolytes. *Electrochimica Acta* **2000**, *45* (8–9), 1481–1490. https://doi.org/10.1016/S0013-4686(99)00363-1.
(114) Kumar, B. Polymer–Ceramic Composite Protonic Conductors. *J. Power Sources* **2003**, *123* (2), 132–136. https://doi.org/10.1016/S0378-7753(03)00530-5.
(115) Miyake, N.; Wainright, J. S.; Savinell, R. F. Evaluation of a Sol-Gel Derived Nafion/Silica Hybrid Membrane for Proton Electrolyte Membrane Fuel Cell Applications: I. Proton Conductivity and Water Content. *J. Electrochem. Soc.* **2001**, *148* (8), A898. https://doi.org/10.1149/1.1383071.
(116) Panero, S.; Scrosati, B.; Greenbaum, S. G. Ionic Conductivity and 7Li NMR Study of Poly(Ethylene Glycol) Complexed with Lithium Salts. *Electrochimica Acta* **1992**, *37* (9), 1533–1539. https://doi.org/10.1016/0013-4686(92)80106-V.
(117) Borghini, M. C.; Mastragostino, M.; Passerini, S.; Scrosati, B. Electrochemical Properties of Polyethylene Oxide - Li [(CF 3 SO 2) 2 N] - Gamma - LiAlO2 Composite Polymer Electrolytes. *J. Electrochem. Soc.* **1995**, *142* (7), 2118–2121. https://doi.org/10.1149/1.2044260.
(118) Golodnitsky, D.; Ardel, G.; Strauss, E.; Peled, E.; Lareah, Y.; Rosenberg, Y. Conduction Mechanisms in Concentrated LiI-Polyethylene Oxide- Al2 O 3-Based Solid Electrolytes. *J. Electrochem. Soc.* **1997**, *144* (10), 3484–3491. https://doi.org/10.1149/1.1838037.
(119) Krawiec, W.; Scanlon, L. G.; Fellner, J. P.; Vaia, R. A.; Vasudevan, S.; Giannelis, E. P. Polymer Nanocomposites: A New Strategy for Synthesizing Solid Electrolytes for Rechargeable Lithium Batteries. *J. Power Sources* **1995**, *54* (2), 310–315. https://doi.org/10.1016/0378-7753(94)02090-P.
(120) Wang, C.; Zhang, X.-W.; Appleby, A. J. Solvent-Free Composite PEO-Ceramic Fiber/Mat Electrolytes for Lithium Secondary Cells. *J. Electrochem. Soc.* **2005**, *152* (1), A205. https://doi.org/10.1149/1.1828952.
(121) Li, Q.; Takeda, Y.; Imanish, N.; Yang, J.; Sun, H. Y.; Yamamoto, O. Cycling Performances and Interfacial Properties of a Li/PEO-Li(CF3SO2)2N-Ceramic Filler/LiNi0.8Co0.2O2 Cell. *J. Power Sources* **2001**, *97–98*, 795–797. https://doi.org/10.1016/S0378-7753(01)00610-3.

(122) Bates, J. Thin-Film Lithium and Lithium-Ion Batteries. *Solid State Ion.* **2000**, *135* (1–4), 33–45. https://doi.org/10.1016/S0167-2738(00)00327-1.
(123) Bates, J. B.; Dudney, N. J.; Gruzalski, G. R.; Zuhr, R. A.; Choudhury, A.; Luck, C. F.; Robertson, J. D. Fabrication and Characterization of Amorphous Lithium Electrolyte Thin Films and Rechargeable Thin-Film Batteries. *J. Power Sources* **1993**, *43* (1–3), 103–110. https://doi.org/10.1016/0378-7753(93)80106-Y.
(124) Bates, J. B.; Dudney, N. J.; Neudecker, B. J.; Hart, F. X.; Jun, H. P.; Hackney, S. A. Preferred Orientation of Polycrystalline LiCoO[Sub 2] Films. *J. Electrochem. Soc.* **2000**, *147* (1), 59. https://doi.org/10.1149/1.1393157.
(125) Magistris, A.; Chiodelli, G.; Villa, M. Lithium Borophosphate Vitreous Electrolytes. *J. Power Sources* **1985**, *14* (1–3), 87–91. https://doi.org/10.1016/0378-7753(85)88016-2.
(126) Pribat, D. *Rechargeable Batteries—Materials, Technologies and New Trends; Zhang, Z., Zhang, SS, Eds*; Springer: Berlin/Heidelberg, Germany, 2015.
(127) Yoon, Y.; Park, C.; Kim, J.; Shin, D. Characterization of Lithium Borophosphate Glass Thin Film Electrolytes Deposited by RF-Magnetron Sputtering for Micro-Batteries. *Solid State Ion.* **2012**, *225*, 636–640. https://doi.org/10.1016/j.ssi.2012.05.008.
(128) Fleutot, B.; Pecquenard, B.; Martinez, H.; Levasseur, A. Lithium Borophosphate Thin Film Electrolyte as an Alternative to LiPON for Solder-Reflow Processed Lithium-Ion Microbatteries. *Solid State Ion.* **2013**, *249*, 49–55.
(129) Aaltonen, T.; Nilsen, O.; Magrasó, A.; Fjellvag, H. Atomic Layer Deposition of Li2O–Al2O3 Thin Films. *Chem. Mater.* **2011**, *23* (21), 4669–4675.
(130) Comstock, D. J.; Elam, J. W. Mechanistic Study of Lithium Aluminum Oxide Atomic Layer Deposition. *J. Phys. Chem. C* **2013**, *117* (4), 1677–1683.
(131) Hämäläinen, J.; Holopainen, J.; Munnik, F.; Hatanpää, T.; Heikkilä, M.; Ritala, M.; Leskelä, M. Lithium Phosphate Thin Films Grown by Atomic Layer Deposition. *J. Electrochem. Soc.* **2012**, *159* (3), A259.
(132) Wu, J.; Zeng, H.; Li, X.; Xiang, X.; Liao, Y.; Xue, Z.; Ye, Y.; Xie, X. Ultralight Layer-by-layer Self-assembled MoS2-polymer Modified Separator for Simultaneously Trapping Polysulfides and Suppressing Lithium Dendrites. *Adv. Energy Mater.* **2018**, *8* (35), 1802430.
(133) Bazant, M. Z. Theory of Chemical Kinetics and Charge Transfer Based on Nonequilibrium Thermodynamics. *Acc. Chem. Res.* **2013**, *46* (5), 1144–1160. https://doi.org/10.1021/ar300145c.
(134) Sekimoto, K. Lecture Notes in Physics. **2010**.
(135) Bard, A. J.; Faulkner, L. R. Fundamentals and Applications. *Electrochem. Methods* **2001**, *2* (482), 580–632.
(136) Monroe, C.; Newman, J. The Impact of Elastic Deformation on Deposition Kinetics at Lithium/Polymer Interfaces. *J. Electrochem. Soc.* **2005**, *152* (2), A396. https://doi.org/10.1149/1.1850854.
(137) Monroe, C.; Newman, J. Dendrite Growth in Lithium/Polymer Systems. *J. Electrochem. Soc.* **2003**, *150* (10), A1377. https://doi.org/10.1149/1.1606686.
(138) Barai, P.; Higa, K.; Srinivasan, V. Effect of Initial State of Lithium on the Propensity for Dendrite Formation: A Theoretical Study. *J. Electrochem. Soc.* **2017**, *164* (2), A180–A189. https://doi.org/10.1149/2.0661702jes.

(139) Barai, P.; Higa, K.; Srinivasan, V. Impact of External Pressure and Electrolyte Transport Properties on Lithium Dendrite Growth. *J. Electrochem. Soc.* **2018**, *165* (11), A2654–A2666. https://doi.org/10.1149/2.0651811jes.
(140) Barai, P.; Higa, K.; Srinivasan, V. Lithium Dendrite Growth Mechanisms in Polymer Electrolytes and Prevention Strategies. *Phys. Chem. Chem. Phys.* **2017**, *19* (31), 20493–20505. https://doi.org/10.1039/C7CP03304D.
(141) Barai, P.; Higa, K.; Ngo, A. T.; Curtiss, L. A.; Srinivasan, V. Mechanical Stress Induced Current Focusing and Fracture in Grain Boundaries. *J. Electrochem. Soc.* **2019**, *166* (10), A1752–A1762. https://doi.org/10.1149/2.0321910jes.
(142) Barai, P.; Ngo, A. T.; Narayanan, B.; Higa, K.; Curtiss, L. A.; Srinivasan, V. The Role of Local Inhomogeneities on Dendrite Growth in LLZO-Based Solid Electrolytes. *J. Electrochem. Soc.* **2020**, *167* (10), 100537. https://doi.org/10.1149/1945-7111/ab9b08.
(143) Ahmad, Z.; Viswanathan, V. Stability of Electrodeposition at Solid-Solid Interfaces and Implications for Metal Anodes. *Phys. Rev. Lett.* **2017**, *119* (5), 056003. https://doi.org/10.1103/PhysRevLett.119.056003.
(144) Yu, S.; Siegel, D. J. Grain Boundary Softening: A Potential Mechanism for Lithium Metal Penetration through Stiff Solid Electrolytes. *ACS Appl. Mater. Interfaces* **2018**, *10* (44), 38151–38158. https://doi.org/10.1021/acsami.8b17223.
(145) Tian, H.-K.; Xu, B.; Qi, Y. Computational Study of Lithium Nucleation Tendency in Li7La3Zr2O12 (LLZO) and Rational Design of Interlayer Materials to Prevent Lithium Dendrites. *J. Power Sources* **2018**, *392*, 79–86. https://doi.org/10.1016/j.jpowsour.2018.04.098.
(146) Guyer, J. E.; Boettinger, W. J.; Warren, J. A.; McFadden, G. B. Phase Field Modeling of Electrochemistry. I. Equilibrium. *Phys. Rev. E* **2004**, *69* (2), 021603. https://doi.org/10.1103/PhysRevE.69.021603.
(147) Guyer, J. E.; Boettinger, W. J.; Warren, J. A.; McFadden, G. B. Phase Field Modeling of Electrochemistry. II. Kinetics. *Phys. Rev. E* **2004**, *69* (2), 021604. https://doi.org/10.1103/PhysRevE.69.021604.
(148) Liang, L.; Qi, Y.; Xue, F.; Bhattacharya, S.; Harris, S. J.; Chen, L.-Q. Nonlinear Phase-Field Model for Electrode-Electrolyte Interface Evolution. *Phys. Rev. E* **2012**, *86* (5), 051609. https://doi.org/10.1103/PhysRevE.86.051609.
(149) Liang, L.; Chen, L.-Q. Nonlinear Phase Field Model for Electrodeposition in Electrochemical Systems. *Appl. Phys. Lett.* **2014**, *105* (26), 263903. https://doi.org/10.1063/1.4905341.
(150) Chen, L.; Zhang, H. W.; Liang, L. Y.; Liu, Z.; Qi, Y.; Lu, P.; Chen, J.; Chen, L.-Q. Modulation of Dendritic Patterns during Electrodeposition: A Nonlinear Phase-Field Model. *J. Power Sources* **2015**, *300*, 376–385. https://doi.org/10.1016/j.jpowsour.2015.09.055.
(151) Yan, H. H.; Bie, Y. H.; Cui, X. Y.; Xiong, G. P.; Chen, L. A Computational Investigation of Thermal Effect on Lithium Dendrite Growth. *Energy Convers. Manag.* **2018**, *161*, 193–204. https://doi.org/10.1016/j.enconman.2018.02.002.
(152) Yurkiv, V.; Foroozan, T.; Ramasubramanian, A.; Shahbazian-Yassar, R.; Mashayek, F. Phase-Field Modeling of Solid Electrolyte Interface (SEI) Influence on Li Dendritic Behavior. *Electrochimica Acta* **2018**, *265*, 609–619. https://doi.org/10.1016/j.electacta.2018.01.212.

(153) Yurkiv, V.; Foroozan, T.; Ramasubramanian, A.; Shahbazian-Yassar, R.; Mashayek, F. The Influence of Stress Field on Li Electrodeposition in Li-Metal Battery. *MRS Commun.* **2018**, *8* (03), 1285–1291. https://doi.org/10.1557/mrc.2018.146.
(154) Hong, Z.; Viswanathan, V. Phase-Field Simulations of Lithium Dendrite Growth with Open-Source Software. *ACS Energy Lett.* **2018**, *3* (7), 1737–1743. https://doi.org/10.1021/acsenergylett.8b01009.
(155) Hong, Z.; Viswanathan, V. Prospect of Thermal Shock Induced Healing of Lithium Dendrite. *ACS Energy Lett.* **2019**, *4* (5), 1012–1019. https://doi.org/10.1021/acsenergylett.9b00433.
(156) Tian, H.-K.; Liu, Z.; Ji, Y.; Chen, L.-Q.; Qi, Y. Interfacial Electronic Properties Dictate Li Dendrite Growth in Solid Electrolytes. *Chem. Mater.* **2019**, *31* (18), 7351–7359. https://doi.org/10.1021/acs.chemmater.9b01967.
(157) Liu, Z.; Li, Y.; Ji, Y.; Zhang, Q.; Xiao, X.; Yao, Y.; Chen, L.-Q.; Qi, Y. Dendrite-Free Lithium Based on Lessons Learned from Lithium and Magnesium Electrodeposition Morphology Simulations. *Cell Rep. Phys. Sci.* **2021**, *2* (1), 100294. https://doi.org/10.1016/j.xcrp.2020.100294.
(158) Li, G.; Liu, Z.; Huang, Q.; Gao, Y.; Regula, M.; Wang, D.; Chen, L.-Q.; Wang, D. Stable Metal Battery Anodes Enabled by Polyethylenimine Sponge Hosts by Way of Electrokinetic Effects. *Nat. Energy* **2018**, *3* (12), 1076–1083. https://doi.org/10.1038/s41560-018-0276-z.
(159) Li, G.; Liu, Z.; Wang, D.; He, X.; Liu, S.; Gao, Y.; AlZahrani, A.; Kim, S. H.; Chen, L.; Wang, D. Electrokinetic Phenomena Enhanced Lithium-Ion Transport in Leaky Film for Stable Lithium Metal Anodes. *Adv. Energy Mater.* **2019**, *9* (22), 1900704. https://doi.org/10.1002/aenm.201900704.
(160) Wan, J.; Xie, J.; Kong, X.; Liu, Z.; Liu, K.; Shi, F.; Pei, A.; Chen, H.; Chen, W.; Chen, J.; Zhang, X.; Zong, L.; Wang, J.; Chen, L.-Q.; Qin, J.; Cui, Y. Ultrathin, Flexible, Solid Polymer Composite Electrolyte Enabled with Aligned Nanoporous Host for Lithium Batteries. *Nat. Nanotechnol.* **2019**, *14* (7), 705–711. https://doi.org/10.1038/s41565-019-0465-3.
(161) Peled, E. The Electrochemical Behavior of Alkali and Alkaline Earth Metals in Nonaqueous Battery Systems—The Solid Electrolyte Interphase Model. *J. Electrochem. Soc.* **1979**, *126* (12), 2047–2051. https://doi.org/10.1149/1.2128859.
(162) Zhang, S. S.; Xu, K.; Jow, T. R. EIS Study on the Formation of Solid Electrolyte Interface in Li-Ion Battery. *Electrochimica Acta* **2006**, *51* (8–9), 1636–1640. https://doi.org/10.1016/j.electacta.2005.02.137.
(163) Ichikawa, K.; Nozaki, H.; Komazawa, N.; Tachibana, A. Theoretical Study of Lithium Clusters by Electronic Stress Tensor. *AIP Adv.* **2012**, *2* (4), 042195. https://doi.org/10.1063/1.4774037.
(164) Han, D. G.; Choi, G. M. Computer Simulation of the Electrical Conductivity of Composites: The Effect of Geometrical Arrangement. *Solid State Ion.* **1998**, *106* (1–2), 71–87. https://doi.org/10.1016/S0167-2738(97)00484-0.
(165) Kalnaus, S.; Sabau, A. S.; Newman, S.; Tenhaeff, W. E.; Daniel, C.; Dudney, N. J. Effective Conductivity of Particulate Polymer Composite Electrolytes Using Random Resistor Network Method. *Solid State Ion.* **2011**, *199–200*, 44–53. https://doi.org/10.1016/j.ssi.2011.07.016.

(166) Nan, C.-W.; Smith, D. M. On Comment on ?Enhancement of Ionic Conduction in CaF2 and BaF2 by Dispersion of Al2O3? *J. Mater. Sci. Lett.* **1991**, *10* (19), 1142–1143. https://doi.org/10.1007/BF00744107.
(167) Kalnaus, S.; Sabau, A. S.; Tenhaeff, W. E.; Dudney, N. J.; Daniel, C. Design of Composite Polymer Electrolytes for Li Ion Batteries Based on Mechanical Stability Criteria. *J. Power Sources* **2012**, *201*, 280–287. https://doi.org/10.1016/j.jpowsour.2011.11.020.
(168) Chen, L.; Zhang, H. W.; Liang, L. Y.; Liu, Z.; Qi, Y.; Lu, P.; Chen, J.; Chen, L.-Q. Modulation of Dendritic Patterns during Electrodeposition: A Nonlinear Phase-Field Model. *J. Power Sources* **2015**, *300*, 376–385. https://doi.org/10.1016/j.jpowsour.2015.09.055.
(169) Zhang, H.-W.; Liu, Z.; Liang, L.; Chen, L.; Qi, Y.; Harris, S. J.; Lu, P.; Chen, L.-Q. Understanding and Predicting the Lithium Dendrite Formation in Li-Ion Batteries: Phase Field Model. *ECS Trans.* **2014**, *61* (8), 1–9. https://doi.org/10.1149/06108.0001ecst.
(170) Mullin, S. A.; Stone, G. M.; Panday, A.; Balsara, N. P. Salt Diffusion Coefficients in Block Copolymer Electrolytes. *J. Electrochem. Soc.* **2011**, *158* (6), A619. https://doi.org/10.1149/1.3563802.
(171) Schultz, R. Fermilab-TM-2191; 2002; pp 1–6.
(172) Tariq, S.; Ammigan, K.; Hurh, P.; Schultz, R.; Liu, P.; Shang, J. LI Material Testing- Fermilab Antiproton Source Litihum Collection Lens. In *Proceedings of the 2003 Bipolar/BiCMOS Circuits and Technology Meeting (IEEE Cat. No.03CH37440)*; IEEE: Portland, OR, USA, 2003; Vol. 3, pp 1452–1454. https://doi.org/10.1109/PAC.2003.1288558.
(173) Geng, H.; Rosen, R.; Zheng, B.; Shimoda, H.; Fleming, L.; Liu, J.; Zhou, O. Fabrication and Properties of Composites of Poly(Ethylene Oxide) and Functionalized Carbon Nanotubes. *Adv Mater* **2002**, No. 19, 4.
(174) Moreno, M.; Quijada, R.; Santa Ana, M. A.; Benavente, E.; Gomez-Romero, P.; González, G. Electrical and Mechanical Properties of Poly(Ethylene Oxide)/Intercalated Clay Polymer Electrolyte. *Electrochimica Acta* **2011**, *58*, 112–118. https://doi.org/10.1016/j.electacta.2011.08.096.
(175) Li, L.; Basu, S.; Wang, Y.; Chen, Z.; Hundekar, P.; Wang, B.; Shi, J.; Shi, Y.; Narayanan, S.; Koratkar, N. Self-Heating–Induced Healing of Lithium Dendrites. *Science* **2018**, *359* (6383), 1513–1516. https://doi.org/10.1126/science.aap8787.
(176) Rumble, J. R. Formaldehyde. *CRC Handb. Chem. Phys.* **2018**, 3–28.
(177) He, Y.; Gao, N.; Jiang, Y.; Ren, B.; Chen, G. Isobaric Heat Capacity Measurements for Dimethyl Ether and 1,1-Difluoroethane in the Liquid Phase at Temperatures from 305 K to 365 K and Pressures up to 5 MPa. *J. Chem. Eng. Data* **2014**, *59* (9), 2885–2890. https://doi.org/10.1021/je500512f.
(178) Tanaka, K.; Higashi, Y. Measurements of the Isobaric Specific Heat Capacity and Density for Dimethyl Ether in the Liquid State. *J. Chem. Eng. Data* **2010**, *55* (8), 2658–2661. https://doi.org/10.1021/je900922x.
(179) Park, C.; Kanduč, M.; Chudoba, R.; Ronneburg, A.; Risse, S.; Ballauff, M.; Dzubiella, J. Molecular Simulations of Electrolyte Structure and Dynamics in Lithium–Sulfur Battery Solvents. *J. Power Sources* **2018**, *373*, 70–78. https://doi.org/10.1016/j.jpowsour.2017.10.081.

(180) Bower, A. F. *Applied Mechanics of Solids*, 0 ed.; CRC Press, 2009. https://doi.org/10.1201/9781439802489.
(181) Ouyang, R.; Curtarolo, S.; Ahmetcik, E.; Scheffler, M.; Ghiringhelli, L. M. SISSO: A Compressed-Sensing Method for Identifying the Best Low-Dimensional Descriptor in an Immensity of Offered Candidates. *Phys. Rev. Mater.* **2018**, *2* (8), 083802. https://doi.org/10.1103/PhysRevMaterials.2.083802.
(182) Glorot, X.; Bordes, A.; Bengio, Y. Deep Sparse Rectifier Neural Networks. In *Proceedings of the Fourteenth International Conference on Artificial Intelligence and Statistics*; Gordon, G., Dunson, D., Dudík, M., Eds.; Proceedings of Machine Learning Research; PMLR: Fort Lauderdale, FL, USA, 2011; Vol. 15, pp 315–323.
(183) Tieleman, T.; Hinton, G.; others. Lecture 6.5-Rmsprop: Divide the Gradient by a Running Average of Its Recent Magnitude. *COURSERA Neural Netw. Mach. Learn.* **2012**, *4* (2), 26–31.
(184) Srivastava, N.; Hinton, G.; Krizhevsky, A.; Sutskever, I.; Salakhutdinov, R. Dropout: A Simple Way to Prevent Neural Networks from Overfitting. *J. Mach. Learn. Res.* **2014**, *15* (1), 1929–1958.
(185) Tikhonov, A. N. On the Stability of Inverse Problems. In *Dokl. Akad. Nauk SSSR*; 1943; Vol. 39, pp 195–198.
(186) Tibshirani, R. Regression Shrinkage and Selection Via the Lasso. *J. R. Stat. Soc. Ser. B Methodol.* **1996**, *58* (1), 267–288. https://doi.org/10.1111/j.2517-6161.1996.tb02080.x.
(187) Kresse, G.; Hafner, J. Ab Initio Molecular Dynamics for Liquid Metals. *Phys. Rev. B* **1993**, *47* (1), 558–561. https://doi.org/10.1103/PhysRevB.47.558.
(188) Kresse, G.; Furthmüller, J.; Hafner, J. Theory of the Crystal Structures of Selenium and Tellurium: The Effect of Generalized-Gradient Corrections to the Local-Density Approximation. *Phys. Rev. B* **1994**, *50* (18), 13181–13185. https://doi.org/10.1103/PhysRevB.50.13181.
(189) Kresse, G.; Furthmüller, J. Efficient Iterative Schemes for *Ab Initio* Total-Energy Calculations Using a Plane-Wave Basis Set. *Phys. Rev. B* **1996**, *54* (16), 11169–11186. https://doi.org/10.1103/PhysRevB.54.11169.
(190) Kresse, G.; Furthmüller, J. Efficiency of Ab-Initio Total Energy Calculations for Metals and Semiconductors Using a Plane-Wave Basis Set. *Comput. Mater. Sci.* **1996**, *6* (1), 15–50. https://doi.org/10.1016/0927-0256(96)00008-0.
(191) Perdew, J. P.; Chevary, J. A.; Vosko, S. H.; Jackson, K. A.; Pederson, M. R.; Singh, D. J.; Fiolhais, C. Atoms, Molecules, Solids, and Surfaces: Applications of the Generalized Gradient Approximation for Exchange and Correlation. *Phys. Rev. B* **1992**, *46* (11), 6671–6687. https://doi.org/10.1103/PhysRevB.46.6671.
(192) Monkhorst, H. J.; Pack, J. D. Special Points for Brillouin-Zone Integrations. *Phys. Rev. B* **1976**, *13* (12), 5188–5192. https://doi.org/10.1103/PhysRevB.13.5188.
(193) Geng, Z.; Lu, J.; Li, Q.; Qiu, J.; Wang, Y.; Peng, J.; Huang, J.; Li, W.; Yu, X.; Li, H. Lithium Metal Batteries Capable of Stable Operation at Elevated Temperature. *Energy Storage Mater.* **2019**, *23*, 646–652. https://doi.org/10.1016/j.ensm.2019.03.005.
(194) Xiao, J. How Lithium Dendrites Form in Liquid Batteries. *Science* **2019**, *366* (6464), 426–427. https://doi.org/10.1126/science.aay8672.

(195) Cheng, Q.; Wei, L.; Liu, Z.; Ni, N.; Sang, Z.; Zhu, B.; Xu, W.; Chen, M.; Miao, Y.; Chen, L.-Q.; Min, W.; Yang, Y. Operando and Three-Dimensional Visualization of Anion Depletion and Lithium Growth by Stimulated Raman Scattering Microscopy. *Nat. Commun.* **2018**, *9* (1), 2942. https://doi.org/10.1038/s41467-018-05289-z.

(196) Ren, Y.; Zhou, Y.; Cao, Y. Inhibit of Lithium Dendrite Growth in Solid Composite Electrolyte by Phase-Field Modeling. *J. Phys. Chem. C* **2020**, *124* (23), 12195–12204. https://doi.org/10.1021/acs.jpcc.0c01116.

(197) Sakuda, A.; Hayashi, A.; Takigawa, Y.; Higashi, K.; Tatsumisago, M. Evaluation of Elastic Modulus of Li_2S–P_2S_5 Glassy Solid Electrolyte by Ultrasonic Sound Velocity Measurement and Compression Test. *J. Ceram. Soc. Jpn.* **2013**, *121* (1419), 946–949. https://doi.org/10.2109/jcersj2.121.946.

(198) Herbert, E. G.; Tenhaeff, W. E.; Dudney, N. J.; Pharr, G. M. Mechanical Characterization of LiPON Films Using Nanoindentation. *Thin Solid Films* **2011**, *520* (1), 413–418. https://doi.org/10.1016/j.tsf.2011.07.068.

(199) Kasemchainan, J.; Zekoll, S.; Spencer Jolly, D.; Ning, Z.; Hartley, G. O.; Marrow, J.; Bruce, P. G. Critical Stripping Current Leads to Dendrite Formation on Plating in Lithium Anode Solid Electrolyte Cells. *Nat. Mater.* **2019**, *18* (10), 1105–1111. https://doi.org/10.1038/s41563-019-0438-9.

(200) Krauskopf, T.; Hartmann, H.; Zeier, W. G.; Janek, J. Toward a Fundamental Understanding of the Lithium Metal Anode in Solid-State Batteries—An Electrochemo-Mechanical Study on the Garnet-Type Solid Electrolyte $Li_{6.25}Al_{0.25}La_3Zr_2O_{12}$. *ACS Appl. Mater. Interfaces* **2019**, *11* (15), 14463–14477. https://doi.org/10.1021/acsami.9b02537.

(201) Wang, M. J.; Choudhury, R.; Sakamoto, J. Characterizing the Li-Solid-Electrolyte Interface Dynamics as a Function of Stack Pressure and Current Density. *Joule* **2019**, *3* (9), 2165–2178. https://doi.org/10.1016/j.joule.2019.06.017.

(202) Zhang, X.; Wang, Q. J.; Harrison, K. L.; Jungjohann, K.; Boyce, B. L.; Roberts, S. A.; Attia, P. M.; Harris, S. J. Rethinking How External Pressure Can Suppress Dendrites in Lithium Metal Batteries. *J. Electrochem. Soc.* **2019**, *166* (15), A3639–A3652. https://doi.org/10.1149/2.0701914jes.

(203) Ding, S.; Fairgrieve-Park, L.; Sendetskyi, O.; Fleischauer, M. D. Compressive Creep Deformation of Lithium Foil at Varied Cell Conditions. *J. Power Sources* **2021**, *488*, 229404. https://doi.org/10.1016/j.jpowsour.2020.229404.

(204) Liu, W.; Lee, S. W.; Lin, D.; Shi, F.; Wang, S.; Sendek, A. D.; Cui, Y. Enhancing Ionic Conductivity in Composite Polymer Electrolytes with Well-Aligned Ceramic Nanowires. *Nat. Energy* **2017**, *2* (5), 17035. https://doi.org/10.1038/nenergy.2017.35.

(205) Sharafi, A.; Meyer, H. M.; Nanda, J.; Wolfenstine, J.; Sakamoto, J. Characterizing the Li–Li7La3Zr2O12 Interface Stability and Kinetics as a Function of Temperature and Current Density. *J. Power Sources* **2016**, *302*, 135–139. https://doi.org/10.1016/j.jpowsour.2015.10.053.

(206) Sharafi, A.; Kazyak, E.; Davis, A. L.; Yu, S.; Thompson, T.; Siegel, D. J.; Dasgupta, N. P.; Sakamoto, J. Surface Chemistry Mechanism of Ultra-Low Interfacial Resistance in the Solid-State Electrolyte $Li_7La_3Zr_2O_{12}$. *Chem. Mater.* **2017**, *29* (18), 7961–7968. https://doi.org/10.1021/acs.chemmater.7b03002.

(207) Bai, P.; Li, J.; Brushett, F. R.; Bazant, M. Z. Transition of Lithium Growth Mechanisms in Liquid Electrolytes. *Energy Environ. Sci.* **2016**, *9* (10), 3221–3229. https://doi.org/10.1039/C6EE01674J.
(208) Sharon, D.; Bennington, P.; Patel, S. N.; Nealey, P. F. Stabilizing Dendritic Electrodeposition by Limiting Spatial Dimensions in Nanostructured Electrolytes. *ACS Energy Lett.* **2020**, *5* (9), 2889–2896. https://doi.org/10.1021/acsenergylett.0c01543.
(209) Capuano, F.; Croce, F.; Scrosati, B. Composite Polymer Electrolytes. *J. Electrochem. Soc.* **1991**, *138* (7), 1918–1922. https://doi.org/10.1149/1.2085900.
(210) Li, Z.; Su, G.; Wang, X.; Gao, D. Micro-Porous P(VDF-HFP)-Based Polymer Electrolyte Filled with AlO Nanoparticles. *Solid State Ion.* **2005**, *176* (23–24), 1903–1908. https://doi.org/10.1016/j.ssi.2005.05.006.
(211) Gantenbein, S.; Schönleber, M.; Weiss, M.; Ivers-Tiffée, E. Capacity Fade in Lithium-Ion Batteries and Cyclic Aging over Various State-of-Charge Ranges. *Sustainability* **2019**, *11* (23), 6697. https://doi.org/10.3390/su11236697.
(212) Yang, H.; Qiao, Y.; Chang, Z.; Deng, H.; Zhu, X.; Zhu, R.; Xiong, Z.; He, P.; Zhou, H. Reducing Water Activity by Zeolite Molecular Sieve Membrane for Long-Life Rechargeable Zinc Battery. *Adv. Mater.* **2021**, *33* (38), 2102415. https://doi.org/10.1002/adma.202102415.
(213) Ma, L.; Chen, S.; Li, N.; Liu, Z.; Tang, Z.; Zapien, J. A.; Chen, S.; Fan, J.; Zhi, C. Hydrogen-Free and Dendrite-Free All-Solid-State Zn-Ion Batteries. *Adv. Mater.* **2020**, *32* (14), 1908121. https://doi.org/10.1002/adma.201908121.
(214) Wang, F.; Borodin, O.; Gao, T.; Fan, X.; Sun, W.; Han, F.; Faraone, A.; Dura, J. A.; Xu, K.; Wang, C. Highly Reversible Zinc Metal Anode for Aqueous Batteries. *Nat. Mater.* **2018**, *17* (6), 543–549. https://doi.org/10.1038/s41563-018-0063-z.
(215) Cao, L.; Li, D.; Pollard, T.; Deng, T.; Zhang, B.; Yang, C.; Chen, L.; Vatamanu, J.; Hu, E.; Hourwitz, M. J.; Ma, L.; Ding, M.; Li, Q.; Hou, S.; Gaskell, K.; Fourkas, J. T.; Yang, X.-Q.; Xu, K.; Borodin, O.; Wang, C. Fluorinated Interphase Enables Reversible Aqueous Zinc Battery Chemistries. *Nat. Nanotechnol.* **2021**, *16* (8), 902–910. https://doi.org/10.1038/s41565-021-00905-4.
(216) Sun, W.; Wang, F.; Zhang, B.; Zhang, M.; Küpers, V.; Ji, X.; Theile, C.; Bieker, P.; Xu, K.; Wang, C.; Winter, M. A Rechargeable Zinc-Air Battery Based on Zinc Peroxide Chemistry. *Science* **2021**, *371* (6524), 46–51. https://doi.org/10.1126/science.abb9554.
(217) Chen, Z.; Mo, F.; Wang, T.; Yang, Q.; Huang, Z.; Wang, D.; Liang, G.; Chen, A.; Li, Q.; Guo, Y.; Li, X.; Fan, J.; Zhi, C. Zinc/Selenium Conversion Battery: A System Highly Compatible with Both Organic and Aqueous Electrolytes. *Energy Environ. Sci.* **2021**, *14* (4), 2441–2450. https://doi.org/10.1039/D0EE02999H.
(218) Liu, C.; Luo, Z.; Deng, W.; Wei, W.; Chen, L.; Pan, A.; Ma, J.; Wang, C.; Zhu, L.; Xie, L.; Cao, X.-Y.; Hu, J.; Zou, G.; Hou, H.; Ji, X. Liquid Alloy Interlayer for Aqueous Zinc-Ion Battery. *ACS Energy Lett.* **2021**, *6* (2), 675–683. https://doi.org/10.1021/acsenergylett.0c02569.
(219) Cao, Z.; Zhu, X.; Xu, D.; Dong, P.; Chee, M. O. L.; Li, X.; Zhu, K.; Ye, M.; Shen, J. Eliminating Zn Dendrites by Commercial Cyanoacrylate Adhesive for Zinc Ion Battery. *Energy Storage Mater.* **2021**, *36*, 132–138. https://doi.org/10.1016/j.ensm.2020.12.022.

(220) Zhou, J.; Xie, M.; Wu, F.; Mei, Y.; Hao, Y.; Huang, R.; Wei, G.; Liu, A.; Li, L.; Chen, R. Ultrathin Surface Coating of Nitrogen-Doped Graphene Enables Stable Zinc Anodes for Aqueous Zinc-Ion Batteries. *Adv. Mater.* **2021**, *33* (33), 2101649. https://doi.org/10.1002/adma.202101649.
(221) Wang, M.; Zhang, F.; Lee, C.-S.; Tang, Y. Low-Cost Metallic Anode Materials for High Performance Rechargeable Batteries. *Adv. Energy Mater.* **2017**, *7* (23), 1700536. https://doi.org/10.1002/aenm.201700536.
(222) Mhin, B. J.; Lee, S.; Cho, S. J.; Lee, K.; Kim, K. S. Zn(H2O)2+6 Is Very Stable among Aqua-Zn(II) Ions. *Chem. Phys. Lett.* **1992**, *197* (1–2), 77–80. https://doi.org/10.1016/0009-2614(92)86025-D.
(223) Dong, Y.; Miao, L.; Ma, G.; Di, S.; Wang, Y.; Wang, L.; Xu, J.; Zhang, N. Non-Concentrated Aqueous Electrolytes with Organic Solvent Additives for Stable Zinc Batteries. *Chem. Sci.* **2021**, *12* (16), 5843–5852. https://doi.org/10.1039/D0SC06734B.
(224) De, S.; Ali, Sk. M.; Ali, A.; Gaikar, V. G. Micro-Solvation of the Zn2+ Ion—a Case Study. *Phys. Chem. Chem. Phys.* **2009**, *11* (37), 8285. https://doi.org/10.1039/b902422k.

Biographical Information

Yao Ren received his B.S. degree in Polymer Science and Engineering from Qingdao University of Science and Technology, Shandong, China in 2014. He also earned his M.S. degree from Nanjing University, Jiangsu, China in 2017. His research focused on the memory application by ferroelectric polymers in his master. Then he joined Department of Materials Science and Engineering of University of Texas at Arlington to pursue his Ph.D. in 2018. Under Dr. Ye Cao's supervision, he developed a phase-field model of Li metal battery to study the mechanical effects of solid electrolyte on the dendrite growth. He also studied the mechanism of dead Li formation. As the side projects, his research also includes the DFT calculation of Thiadiazole and Dimercapto-Thiadiazole adsorption on Copper and Silver surfaces, phase-field simulations of ferroelectric materials and semiconductor devices.

List of Publications during Ph.D.

(1) **Ren, Y.**; Zhou, Y.; Cao, Y. Inhibit of Lithium Dendrite Growth in Solid Composite Electrolyte by Phase-Field Modeling. *J. Phys. Chem. C* **2020**, *124* (23), 12195–12204. https://doi.org/10.1021/acs.jpcc.0c01116.

(2) **Ren, Y.**; Rahmani, H.; Meletis, E. I.; Zhang, Q.; Cao, Y. A First-Principles Study of Thiadiazole and Dimercapto-Thiadiazole Adsorption on Copper and Silver Surfaces. *Mater. Chem. Phys.* **2021**, *273*, 125057. https://doi.org/10.1016/j.matchemphys.2021.125057.

(3) Kelley, K. P.; **Ren, Y.**; Dasgupta, A.; Kavle, P.; Jesse, S.; Vasudevan, R. K.; Cao, Y.; Martin, L. W.; Kalinin, S. V. Probing Metastable Domain Dynamics *via* Automated Experimentation in Piezoresponse Force Microscopy. *ACS Nano* **2021**, *15* (9), 15096–15103. https://doi.org/10.1021/acsnano.1c05455.

(4) Kelley, K. P.; Li, L.; **Ren, Y.**; Ehara, Y.; Funakubo, H.; Somnath, S.; Jesse, S.; Cao, Y.; Kannan, R.; Vasudevan, R. K.; Kalinin, S. V. Tensor Factorization for Elucidating Mechanisms of Piezoresponse Relaxation via Dynamic Piezoresponse Force Spectroscopy. *Npj Comput. Mater.* **2020**, *6* (1), 113. https://doi.org/10.1038/s41524-020-00384-6.

(5) Kelley, K. P.; **Ren, Y.**; Morozovska, A. N.; Eliseev, E. A.; Ehara, Y.; Funakubo, H.; Giamarchi, T.; Balke, N.; Vasudevan, R. K.; Cao, Y.; Jesse, S.; Kalinin, S. V. Dynamic Manipulation in Piezoresponse Force Microscopy: Creating Nonequilibrium Phases with Large Electromechanical Response. *ACS Nano* **2020**, *14* (8), 10569–10577. https://doi.org/10.1021/acsnano.0c04601.

(6) Li, Y.; Cao, D.; Arnold, W.; **Ren, Y.**; Liu, C.; Jasinski, J. B.; Druffel, T.; Cao, Y.; Zhu, H.; Wang, H. Regulated Lithium Ionic Flux through Well-Aligned Channels for Lithium Dendrite Inhibition in Solid-State Batteries. *Energy Storage Mater.* **2020**, *31*, 344–351. https://doi.org/10.1016/j.ensm.2020.06.029.

(7) Agar, J. C.; Naul, B.; Pandya, S.; van der Walt, S.; Maher, J.; **Ren, Y.**; Chen, L.-Q.; Kalinin, S. V.; Vasudevan, R. K.; Cao, Y.; Bloom, J. S.; Martin, L. W. Revealing Ferroelectric Switching Character Using Deep Recurrent Neural Networks. *Nat. Commun.* **2019**, 10 (1), 4809. https://doi.org/10.1038/s41467-019-12750-0.

Under Review

(1) **Ren, Y.**; Zhang, K.; Zhou, Y.; Cao, Y. Phase-field simulation and machine learning study of the effects of elastic and plastic properties of electrode and solid polymer electrolyte on the suppression of Li dendrite growth. *ACS Appl. Mater. Interfaces.*